Development of Tunable Molecular Tension Sensors to Visualize Vinculin Loading and Detect Mechanosensitive Protein Recruitment to Focal Adhesions

by

Andrew Scott LaCroix

Department of Biomedical Engineering
Duke University

Date:_____
Approved:

_____
Brenton D Hoffman, Supervisor

_____
Lingchong You

_____
George A Truskey

_____
Jennifer L West

_____
Keith Burridge

Dissertation submitted in partial fulfillment of
the requirements for the degree of Doctor
of Philosophy in the Department of
Biomedical Engineering in the Graduate School
of Duke University

2018

ABSTRACT

Development of tunable molecular tension sensors to visualize vinculin loading and detect mechanosensitive protein recruitment to focal adhesions

by

Andrew Scott LaCroix

Department of Biomedical Engineering
Duke University

Date:_____
Approved:

_____
Brenton D Hoffman, Supervisor

_____
Lingchong You

_____
George A Truskey

_____
Jennifer L West

_____
Keith Burridge

An abstract of a dissertation submitted in partial fulfillment of the requirements for the degree of Doctor of Philosophy in the Department of Biomedical Engineering in the Graduate School of Duke University

2018

Copyright by
Andrew Scott LaCroix
2018

Abstract

Mechanical forces are potent drivers of many biological processes. The form and function of many tissues depends on cells properly receiving and responding to mechanical signals either from neighboring cells or from the underlying matrix. During development, dynamic tissue movements are driven by cell contractility and stem cell fate is affected by the mechanical forces in and the stiffness of the cellular microenvironment. Conversely, aberrant mechanosensitive signaling is associated with the pathological progression of several disease states, such as cancer and atherosclerosis, for which effective treatments are scarce. As such, understanding how cells physically interact with and detect mechanical aspects of their microenvironment is critical to both understanding developmental processes and developing new treatments for disease.

To initiate changes in cell behavior, mechanical information from the microenvironment must be converted into biochemical signals inside cells through molecular scale processes, collectively referred to as mechanotransduction. Many of the events associated with mechanosensitive signaling and mechanotransduction are mediated by force-dependent changes in protein structure and function. However, the lack of available tools to study these molecular scale processes in cells is currently preventing further progress. To address this need, the goals of this dissertation were to (1) improve upon and expand the capabilities of existing tools to visualize molecular

forces and (2) develop novel methodologies to detect key force-sensitive signaling events inside cells.

We began by focusing on the further development and improvement of one of the most critical tools to molecular-scale mechanobiological investigations: Förster Resonance Energy Transfer (FRET)-based molecular tension sensors. While these sensors have contributed greatly to our understanding of mechanobiology, the limited dynamic range and inability to specify the mechanical sensitivity of existing sensors has hindered their use in diverse cellular contexts. Through both experiments and modeling efforts, we developed a comprehensive biophysical understanding of molecular tension sensor function that enabled the creation of new sensors with predictable and tunable mechanical sensitivities. We used this knowledge to create a sensor optimized to study the ~1-6pN loads experienced by vinculin, a critical linker protein that plays an integral role in connecting cells, via focal adhesions (FAs), to the extracellular matrix (ECM). Using this optimized sensor enabled sensitive detection of changes in molecular loads across single cells and even within individual FA structures. We also expanded the capabilities of tension sensors to investigate the potentially distinct roles of protein force and protein extension in activating mechanosensitive signaling. Specifically, a trio of these new biosensors with distinct force- and extension-sensitivities revealed that an extension-based control paradigm underlies cellular control of vinculin loading.

As these sensors uniquely provide insight into which molecules are physically engaged and could be participating in mechanically-based signaling, we next investigated which cytoskeletal structures mediated vinculin loading at multiple length scales within the cell. Specifically, we focused on two active, but distinct force generating machineries inside cells: stress fibers (SFs) and lamellipodial-associated protrusions (LPs). By measuring vinculin tension in various mechanical and biochemical contexts, we found that vinculin is mechanically loaded in both LP and SF structures. However, the distribution of loads across vinculin within individual FAs was dramatically different between these two distinct actin structures. Specifically, asymmetric distribution of vinculin load along individual FAs was an exclusive feature of SF-associated FAs. Subsequent experiments showed that formation and maintenance of these gradient loading profiles are dependent on the activation of specific mediators of cytoskeletal assembly as well as vinculin's interactions with key binding partners. These data suggest that both the magnitude as well as the pattern of vinculin loading within FAs are independently regulated by cells, and thus might serve distinct purposes in cellular mechanosensing.

Towards understanding the biochemical consequences of protein load at the molecular level, we developed an imaging-based technique to detect one of the events most often implicated in mechanically-based signal transduction: the formation of force-sensitive protein-protein interactions (PPIs). While these force sensitive interactions have

been extensively documented in vitro, the extent to which they occur inside living cells is debated. This imaging-based technique, which we refer to as fluorescence-force co-localization (FFC), involves imaging of a FRET-based tension sensor and standard fluorescence-based detection of other proteins of interest to correlate molecular tension with protein recruitment to FAs. Using vinculin as a prototypical example and focusing on a screen-based approach, we used immunofluorescence to measure the relative enrichment of 20 other key FA proteins in areas of high vinculin tension. Factoring in what we previously learned about (1) the importance of actin architecture and (2) the well-established role of vinculin alone in controlling FA composition, we provide a multiparametric perspective on a potential mechanotransduction node associated with high vinculin loads. Focusing on the top five hits from this FFC screen, subsequent experiments revealed a genuine vinculin tension-dependent interaction with migfilin, a LIM domain containing protein that plays both structural roles in FAs and has also been implicated in the regulation of gene transcription. Overall, the work presented in this dissertation provides a means for the detection of force-sensitive PPIs in cells, and the functional role of these interactions can be addressed in future work.

In total, the techniques developed in this dissertation enable detection of multiple molecular events associated with mechanotransduction inside cells. The improvement of FRET-based tension sensors as well as the ability to define their mechanical properties a priori should expedite investigations of molecular forces in

diverse biological contexts. Additionally, the realization of force-dependent PPIs inside cells provided by the FFC screen constitutes a significant step towards uncovering mechanically-based signaling mechanisms inside cells. The more widespread application of these tools will undoubtedly fuel our understanding of mechanotransduction and could enable better control of cell behaviors in engineered tissues and aid in the development of treatments for mechanosensitive diseases.

Contents

Abstract iv

List of Tables xv

List of Figures xvi

Acknowledgements xix

1 Introduction 1

2 Background 6

2.1 Mechanics in biology 6

2.2 Biophysical description of mechanosensitive processes 7

2.2.1 Force as analogous to a post-translational modification 8

2.2.2 Protein responses to mechanical loading: catch and slip bonds 10

2.2.3 Mechanosensitivity as a four-step process 12

2.2.3.1 Mechanotransmission 13

2.2.3.2 Mechanotransduction and mechanosensing 14

2.2.3.3 Mechanoresponse 15

2.3 Focal adhesion structure and function 16

2.3.1 Compositional complexity 17

2.3.2 Hierarchical 3D structure 19

2.3.3 Cytoskeletal regulation of FA dynamics and maturation 21

2.3.3.1 Differential regulation of cytoskeletal structures by Rho and Rac 21

2.3.3.2 FA formation, maturation, and attachment to actin architectures 23

2.3.4 Force-dependent signaling 25

2.4 Force transmission through focal adhesions 27

2.4.1 Measuring force transmission at the cellular and molecular levels 27

2.4.1.1 Measuring forces at the cell-substrate interface: traction force microscopy 28

2.4.1.2 Measuring molecular-scale forces inside cells: FRET-based tension sensors 29

2.4.2 Biophysical control of FA loading and cell contractility 33

2.4.2.1 Force-dependent growth of FAs 34

2.4.2.2 Stress-control versus strain-control 35

2.5 Vinculin as a model mechanosensitive protein 37

2.5.1 Vinculin structure and regulation 38

2.5.2 Role of vinculin in FA force transmission 39

2.5.3 Role of vinculin in mechanosensitive cellular processes 40

3 Tunable Molecular Tension Sensors Reveal Extension-Based Control of Vinculin Loading 42

3.1 Introduction 42

3.2 Methods 44

3.2.1 Cell culture and transfection 44

3.2.2 Generation of TSMods and vinculin tension sensor constructs 45

3.2.3 FRET imaging 47

3.2.4 Quantitative FRET efficiency measurements from 3-cube FRET imaging ... 49

3.2.5 Segmentation and analysis of VinTS in FAs 51

3.2.6 FRET efficiency calculations from spectrofluorometry 52

3.2.7 Statistics, bootstrapping, and data digitization 53

3.3 Results 55

3.3.1 Creation of TSMods based on synthetic unstructured polypeptides 55

3.3.2 A quantitative model describing the mechanical sensitivity of TSMods 61

3.3.2.1 Model Overview 61

3.3.2.2 Extensible domain mechanics are well-described by the worm-like chain model 64

3.3.2.3 Effects of fluorescent proteins 70

3.3.2.4 Accounting for rotational entropy phenomenologically 71

3.3.2.5 Förster resonance energy transfer 74

3.3.2.6 Calculations 75

3.3.2.7 Model validation in unloaded conditions 75

3.3.2.8 Model validation in loaded conditions 79

3.3.2.9 Comparison to other descriptions of TSMod mechanical sensitivity ... 83

3.3.3 Summary of model validation in unloaded conditions 87

3.3.4 Summary of model validation in loaded conditions 88

3.3.5 A novel approach for predicting the in cellulo calibration of TSMods 89

3.3.6 Optimized tension sensor reveals gradients of vinculin tension across FAs 90

3.3.7 Vinculin loading is subject to an extension-based control mechanism 95

3.3.8 Examining extension-based control of vinculin loading with a structural model of a FA 98

3.3.9 Roadmap for future TSMod design 105

3.4 Discussion 108

3.4.1 Updating TSMod design principles 108

3.4.2 Probable causes for vinculin tension asymmetries in FAs 109

3.4.3 Implications of molecular extension-control for rigidity sensing 110

3.5 Summary 111

4 Investigating Asymmetric Distribution of Vinculin Loads Within Individual Focal Adhesions 112

4.1 Introduction 112

4.2 Methods 115

4.2.1 Cell culture and transfection 115

4.2.2 Construction of viral expression plasmids 115

4.2.3 Generating stable cell lines 116

4.2.4 Estimating endogenous expression of VinTS constructs 117

4.2.5 Cell seeding and spreading assays 118

4.2.6 Immunofluorescence 118

4.2.7 FRET imaging 119

4.2.8 FRET image analysis, focal adhesion and cell segmentation 119

4.2.9 Gradient quantification 119

4.2.10 Statistics 120

4.3 Results 121

4.3.1 Two distinct spatial profiles of vinculin loading in FAs 121

4.3.2 Automated quantification of the magnitude of tension gradients 124

4.3.3 Gradient loading of vinculin coincides with SF formation during cell spreading 125

4.3.4 Vinculin loading profiles can be altered by RhoGTPase activation 128

4.3.5 Talin and actin modulate vinculin loading and spatial loading profile 131

4.4 Discussion 134

4.4.1 Role of talin in establishment of vinculin tension gradients 134

4.4.2 Vinculin is mechanically engaged in both LP- and SF-associated FAs..... 135

4.4.3 New information for models of FA force-dependent growth..... 135

4.5 Summary 136

5 Detection of Force-Dependent Protein-Protein Interactions in Focal Adhesions 138

5.1 Introduction 138

5.2 Methods 140

5.2.1 Cell culture 140

5.2.2 Stable expression of VinTS constructs..... 141

5.2.3 Immunofluorescence and proximity ligation assay 141

5.2.4 Microscopy and FRET imaging..... 142

5.2.5 FRET efficiency calculations..... 143

5.2.6 Simulations of FFC data..... 143

5.2.7 Statistics 147

5.3 Results 148

5.3.1 Stochastic simulations guide interpretation of fluorescence-force co-localization data 148

5.3.2 Normalization strategy to visualize force-dependent interactions in simulated data..... 150

5.3.3 Recruitment Index describes molecular enrichment in loaded FAs..... 151

5.3.4 Simulations indicate Recruitment Index is robust to most alternative protein recruitment pathways 153

5.3.5 Candidate selection for FFC screen 155

5.3.6 Measuring vinculin force-dependent protein associations in FAs using FFC 156

5.3.7 FA composition is altered in vinculin -/- cells 159

5.3.8 Spatial gradients in tension also impact FA composition and signaling state 161

5.3.9 Multivariate representation of vinculin mechanotransduction in FAs 164

5.3.10 Verification of novel vinculin force-dependent PPIs in FAs 166

5.4 Discussion 170

5.4.1 Strengths and weaknesses of FFC 170

5.4.2 Implications of force-sensitive PPI between vinculin and migfilin 171

5.5 Summary 172

6 Conclusions and Future Directions 174

6.1 Exploring the limits of extension-based control of protein loading 174

6.2 Elucidating integrin-specific mechanotransduction 175

6.3 Monitoring time-varying mechanosensitive processes in FAs 177

6.4 Implementation of Molecular Tension Sensors In New Systems 178

6.4.1 Studying Protein Loading in Other Subcellular Structures 178

6.4.2 Moving Tension Sensors In Vivo 179

References 181

Biography 205

List of Tables

Table 3.1: Primers used in Chapter 3 47

Table 3.2: Spectral bleed-through coefficients and G factors. 51

Table 3.3: Statistical test details including exact p-values for ANOVAs and post-hoc tests. 54

Table 3.4 Model fit parameters compared to literature estimates. 86

Table 3.5 Persistence length (L_P) for a variety of published polypeptides. 87

Table 5.1: List of antibodies used in FFC screen 142

List of Figures

Figure 2.1 Force impacts protein structure and function 9

Figure 2.2: Types of molecular bonds. 12

Figure 2.3: Molecular events underlying cellular mechanosensitivity. 13

Figure 2.4: Hierarchical organization and molecular complexity in FAs. 18

Figure 2.5: FAs undergo dynamic molecular rearrangements during their assembly and disassembly 25

Figure 2.6: Traction forces and molecular tension are not equivalent. 29

Figure 2.7: FRET-based molecular tension sensor function. 31

Figure 2.8: Vinculin binding partners. 39

Figure 3.1: Design and characterization of tunable FRET-based molecular tension sensors. 56

Figure 3.2: FRET efficiency measurements are insensitive to fixation and sensor intensity. 57

Figure 3.3: Increase in unloaded FRET efficiency with Clover-mRuby2 sensors in vitro 58

Figure 3.4: "Minimal" FPs exhibit spectral properties indistinguishable from full-length parent FPs. 59

Figure 3.5: Schematic depiction of biophysical model describing the mechanical sensitivity of TSMods. 63

Figure 3.6: Verification of the proper implementation of a biophysical model describing the mechanical sensitivity of FRET-based TSMods. 73

Figure 3.7: Parameter constraint has minimal effects on measurement of polypeptide persistence length (L_P) in vitro. 78

Figure 3.8: Parameter constraint has minimal effects on measurement of polypeptide persistence length (L_P) in cellulo. 79

Figure 3.9: Predicting TSMod calibrations using a biophysical model. 81

Figure 3.10: Parameter constraint has minimal effects on measurement of polypeptide persistence length (L_P) for TSMod-like constructs in unloaded or loaded conditions. 83

Figure 3.11: Experimental and theoretical examinations of other models [194] of $(GPGGA)_n$ mechanical sensitivity. 85

Figure 3.12: Selection of optimal $(GGSGGS)_n$ extensible domain length in a Clover-mRuby2 based TSMod for measuring ~1-6 pN loads borne by vinculin. 91

Figure 3.13: Optimized tension sensor reveals sub-FA gradients in vinculin tension. 93

Figure 3.14: FA morphologies, cell morphologies, and sensor localization to FAs are indistinguishable between different versions of VinTS. 94

Figure 3.15: Schematic depiction of force-extension relationships and potential force- and extension-control paradigms. 96

Figure 3.16: Using tension sensors with distinct mechanical sensitivities to test force-based versus extension-based control of vinculin loading. 97

Figure 3.17 Various structural arrangements within FAs could lead to force-based or extension-based control. 104

Figure 3.18: Roadmap to enable the rational design of FRET-based molecular tension sensors. 107

Figure 3.19: Roadmaps to guide the rational design of FRET-based molecular tension sensors for some commonly used FRET-pairs. 108

Figure 4.1: Spatial gradients in vinculin loading are associated with specific actomyosin structures. 123

Figure 4.2: Schematic depicting automated spatial tension gradient measurements. 125

Figure 4.3: Emergence of gradient loading of vinculin during the cell spreading process 128

Figure 4.4: Constitutively-active forms of RhoA and Rac1 impact vinculin spatial loading profile. 131

Figure 4.5: Vinculin's interactions with talin are dispensable for vinculin loading but required for gradient loading profile. 134

Figure 5.1: Schematic depiction of molecular FFC simulations. 149

Figure 5.2: Comparison of multiple metrics to detect force-independent and force-dependent interactions in FFC simulations. 151

Figure 5.3: Calculating protein Recruitment Index. 153

Figure 5.4: Robustness of Recruitment Index to alternative recruitment pathways. 154

Figure 5.5: FFC reveals vinculin tension is associated with distinct molecular composition. 158

Figure 5.6: FA composition is dramatically altered in cells lacking vinculin. 160

Figure 5.7: Origins of vinculin tension, as measured by spatial gradient loading profile also impact FA composition and signaling state. 162

Figure 5.8: Verifying the impact of actin architecture on FA localization of FAK and VASP. 164

Figure 5.9: Multivariate plot of vinculin-dependent FA composition. 166

Figure 5.10: Intensity correlations between VinTS and proteins of interest are disrupted by I997A actin binding mutation. 167

Figure 5.11: Detection of vinculin tension-dependent PPIs in FAs. 169

Acknowledgements

I would like to acknowledge everyone who has assisted me throughout my graduate studies. The completion of this dissertation would not have been possible without the support from my family, friends, and colleagues.

First and foremost, I would like to thank my family, who have always been there for me. Thank you to my parents, Mike and Sue, and my sister Sarah. Your love and constant encouragement have gotten me through the years. Thank you for always having confidence in me and helping me become the person I am today.

I'd like to thank Kristin for being my partner and a source of unwavering support. You have always cheered me on through my successes and helped me to persevere through the more difficult days. I could not have done this without you.

Thank you to all my friends and colleagues in the Hoffman Lab who have helped contribute to this research. I would especially like to thank Katy and Aarti who completed this journey alongside (well slightly ahead of) me. We did it!

I would like to extend thanks to the Duke Biomedical Engineering department and its staff. The Duke community fosters academic and professional growth. This could not have been accomplished without the abundance of resources provided to me through the department.

Finally, thank you to the members of my thesis committee for your guidance and encouragement. And a special thank you to my advisor, Brent for his expertise,

mentorship, and patience throughout the years. You always kept a sense of humor, even when I sometimes lost mine.

1 Introduction

Recently, significant evidence has emerged demonstrating that mechanical stimuli, such as applied forces or the mechanical properties of the extracellular matrix (ECM), are critical determinants of the form and function of cells and tissues [1-6]. In addition to genetic and biochemical factors, mechanical inputs are primary regulators of many fundamental cellular processes, including cell division [7], differentiation [8, 9], and migration [10]. At longer length scales, cell mechanical properties impact cell sorting within the embryo [11] and mediate apical constriction, enabling tissue folding during gastrulation [6]. In contrast, aberrant mechanosensitive signaling has been implicated in many pathophysiological processes [3] including atherosclerotic plaque formation at points of disturbed shear stress [2] and the enhanced metastatic potential of cancer cells in the stiffer tumor microenvironment [12]. Finally, improper activation of mechanosensitive pathways likely causes unintended cellular behaviors within engineered tissues, including the loss of cell phenotype or improper cell contractility or migration [13, 14].

Despite the widespread evidence for the important role mechanical inputs play in numerous biological processes, a mechanistic, molecular understanding of how cells convert mechanical inputs into biochemically detectable signals, a process termed mechanotransduction, is lacking. The current theoretical framework surrounding mechanotransduction is a derivative of protein structure-function relationships. In much

the same way that classical signal transduction pathways are initiated by chemically induced changes in protein structure (e.g. phosphorylation), mechanotransduction pathways are thought to be initiated by mechanically induced deformations in load-bearing proteins [15-17]. The possibility of such mechanically induced events has been elegantly demonstrated in single molecule in vitro systems [18, 19]. However, the extent to which such events occur in living cells, the magnitude and origins of mechanical loads in cellulo, and the biochemical consequences of protein loading have yet to be fully elucidated.

The work described in this dissertation is motivated by a need for techniques capable of detecting the molecular events associated with mechanotransduction inside cells. Broadly, we aimed to (1) develop improved FRET-based molecular tension sensors capable of enhanced and quantitative measurement of protein loads in cellulo and (2) update and expand fluorescence colocalization microscopy techniques to detect the formation of force-sensitive protein-protein interactions. Overall, by employing these techniques to study vinculin mechanotransduction at FAs, we uncovered a surprising extension-based control regulating vinculin loading and found compelling evidence for the cumulative roles of vinculin, vinculin tension, and actin architectures in modulating FA composition and mechanosensitive signaling. These two distinct but complementary techniques represent a significant step towards a quantitative biophysical understanding of the fundamentally molecular events initiating vinculin-dependent and possibly other mechanotransduction pathways.

In Chapter 3, we focused on the improvement of molecular tension sensor function in hopes of making this valuable tool tunable and thus applicable to a multitude of studies in mechanobiology. We systematically examined the components of molecular tension sensors that could be altered to improve their functionality and developed biophysical descriptions of sensor behavior, enabling calibration and deployment of tension sensors in identical environments for the first time. After an extensive validation process, we demonstrated the predictive power of the calibration model through the construction of a tension sensor optimized to measure loads borne by the focal adhesion protein vinculin, which revealed asymmetrically distributed loads across vinculin in single focal adhesions. The cytoskeletal structures that give rise to such tension gradients are further examined in Chapter 4, and their impact on vinculin mechanotransduction is investigated in Chapter 5. Then we utilized a trio of these improved, in cellulo calibrated sensors with distinct force-extension relationships to interrogate the molecular origins of the long-standing observations of cellular stress- versus strain-control of cell contractility. In the context of vinculin mechanobiology, this trio of sensors revealed a novel control paradigm whereby protein extension (molecular analogue to strain) rather than force (molecular analogue to stress) is physically regulated by the cell. Simple physical models of FAs provided molecular insight into the potential ultrastructure and intermolecular interactions that could give rise to such extension-based control.

In Chapter 4, we investigated the cytoskeletal origins of the gradient loading profiles of vinculin detected in Chapter 3 and identified two types of FAs with distinct vinculin loading profiles. Specifically, FAs associated with actin stress fibers (SFs) exhibited gradient loading of vinculin while those loaded by forces associated with lamellipodial protrusion structures showed uniformly high loads across vinculin throughout the FA. We determined that the strength of these tension gradients can be modulating by cell spreading, the Rho-GTPases RhoA and Rac1, and through the disruption of vinculin's interactions with both talin and actin, indicating that the formation of gradient loading is a tightly regulated process. The high tensions present in both types of FAs, but distinct loading profile of vinculin in SF-associated FAs indicated that the loads and loading profiles are separable. These findings thus motivated further investigation (in Chapter 5) into the likely distinct roles of vinculin load and vinculin loading profile in vinculin mechanotransduction pathways.

In Chapter 5, we assessed the biological consequences of molecular tension in terms of alterations in FA composition. We tested the extent to which force-sensitive protein-protein interactions could be detected through the simple combination of molecular tension sensors and immunofluorescent labeling of 22 other core FA components. To attain a more complete picture of the vinculin mechanotransduction signaling axis, we augmented this fluorescence-force colocalization technique with measurements of (1) vinculin-dependent (irrespective of tension) protein recruitment to FAs in wild-type compared to vinculin -/- cell lines and (2) the actin architectural

preference of the candidate proteins in terms of their relative localization to LP- versus SF-associated FAs. Combined, these three measurements revealed a unique molecular signature for vinculin mechanotransduction at FAs. With this rich molecular picture of vinculin tension-dependent signaling, we focused our efforts on validating a mechanistic link between vinculin-loads, actin architectures, and protein recruitment to FAs. For those proteins exhibiting the strongest vinculin tension sensitivity, we measured changes in their recruitment to FAs following disruption of vinculin's ability to bind actin and thus bear load. To examine the specificity of SF-dependent protein localization to FAs, we monitored changes in protein localization to peripheral FAs after perturbing SF formation via the transient activation of Rac1. Finally, we used proximity ligation assays to confirm the formation of genuine vinculin tension-sensitive protein-protein interactions, identifying novel vinculin interacting proteins and updating the picture of vinculin-VASP interactions previously thought to be constitutive.

In Chapter 6, we summarize the main results and conclusions of this work and discuss how these findings might motivate future studies in cell biological and biomedical research.

2 Background

2.1 Mechanics in biology

While mechanobiology is current undergoing a reemergence, evidence for the important role of physical cues in biology dates back more than a century. In 1917, biomathematician D'Arcy Thompson's renowned work "On Growth and Form" advocated for the application of physical and mathematical principles to understand diverse biological systems [20]. Indeed, scientists have documented many instances of mechanical inputs affecting biology at multiple length scales; for instance, mechanical loading augments bone formation [21], laminar shear stress contributes to blood vessel health [22], and cancers are often accompanied by changes in tissue architecture [23].

Although these and other seminal works highlighted a need to understand how mechanical inputs lead to biological outputs, only in the last 30 years have tools become more widely available to study mechanobiology from a mechanistic perspective. Scientists can now use tools like atomic force microscopy to probe the mechanics of single cells and pull on specific subcellular structures. Controlling substrate rigidity and studying the magnitude of cell contractility have been made possible using engineered substrates such as hydrogels and microfabricated pillars used in traction force microscopy experiments. The mechanical responses of individual proteins, which frequently involves nano- and pico-Newton forces, have been measured using magnetic tweezers and optical traps. This assortment of technologies designed to probe the mechanical properties of and quantify physical forces in cells have driven our

understanding of mechanobiology and the role it plays in numerous physiological and pathophysiological processes.

This increasingly molecular-scale toolkit [24] has revealed mechanical regulation of numerous fundamental cellular processes. We now know that forces applied to cells, as well as those that originate from a cell's interrogation of its local microenvironment, are sufficient to activate transcription [25], direct cell migration [26], initiation differentiation pathways [13], or alter the metastatic potential of cancer cells [27]. The far-reaching implications for our understanding of human development [1, 5, 6], treatment of disease [2, 3, 28], and tissue engineering efforts [4, 29, 30] have driven mechanobiological research endeavors.

2.2 Biophysical description of mechanosensitive processes

In discussing the mechanisms by which cells respond to physical stimuli, scientists have adapted some of the terminology used to describe the steps in traditional, biochemically-based cell signaling. Broadly, any molecular or cellular process that can be affected by a mechanical variable, like the stiffness of the ECM or contractile forces generated within a neighboring cell, is referred to as mechanosensitive. However, while cell signaling can generally be explained in terms of the principles of solution chemistry such as reaction kinetics and diffusion coefficients, new terms were required to explain and understand mechanically-based signaling. How cells transmit and interpret mechanical information also required knowledge of the deformability of individual

proteins. In particular, examining how mechanical loads affect protein conformation and protein binding from a molecular perspective has shed light on the molecular mechanisms underlying mechanosensitive processes.

2.2.1 Force as analogous to a post-translational modification

The three-dimensional structure of a protein is central to its function. This is apparent with considering the impact that post-translational modifications, such as phosphorylation, have on protein function. Often phosphorylation events will lead to slight changes in protein conformation, creating docking sites for other proteins, activating some intrinsic catalytic activity in the phospho-protein, or releasing it from a protein complex to achieve some downstream signaling function (Figure 2.1, left).

In analogous terms, molecular scale forces can impact protein structure and thus function. Since protein conformation is chiefly governed by labile non-covalent interactions, even small forces can have just as large of an impact on protein structure as a phosphorylation event. These force-induced conformational shifts in proteins can alter a protein's affinity for key binding partners, activate (or inhibit) catalytic functions, or reveal cryptic binding sites giving rise to novel protein-protein interactions.

Downstream signaling or reinforcement events are thus triggered by a mechanical input (force) rather than a biochemical change (phosphorylation) (Figure 2.1, right).

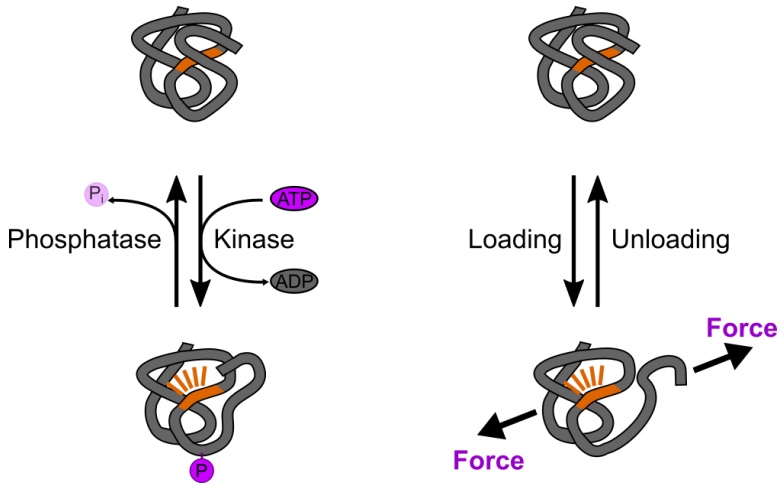

Figure 2.1 Force impacts protein structure and function. Post-translational modifications like phosphorylation alter protein structure and thus function. In analogous terms, forces can lead to similar changes in protein structure and cause similar downstream signaling functions.

The amount of force required to shift the conformational equilibrium of a protein is surprisingly small (in the ~pN range on the order of Brownian motion), as has been calculated theoretically [17] and measured experimentally using single molecule techniques such as atomic force microscopy (AFM), optical traps, or magnetic tweezers [31-34]. For example, a series of experiments that made use of both AFM and magnetic tweezers on substrate-immobilized proteins showed that conformation changes within individual domains of a single talin molecule, resulting in exposure of a cryptic binding site for vinculin, can be induced with as little as 2 pN of force [18, 35]. Additionally, low force transitions have been discovered in certain domains of filamin, where the association between domains 20 and 21 is disrupted at 2-5 pN of exerted force [36]. Single molecule measurements using optical traps have estimated that individual myosin motors can generate forces in the 2-5 pN range, indicating that these low-force

transitions are likely to occur in vivo. Indeed, the amount of energy (work = force * distance) required to stretch an unstructured protein two nanometers against a 2 pN force is approximately 1/20th the energy released by ATP hydrolysis [17], indicating that forces are potentially potent drivers of protein conformational changes.

Although force can be a potent regulator of protein function, many load-bearing proteins whose mechanical stability is critical to cell and tissue integrity have relatively compact domains able to withstand high mechanical loads. For example the Ig or Ig-like domains found in titin [37] are mechanically stable and only unfold upon force application upwards of 150 to 300 pN [37]. Similar results have been found for other load-bearing proteins such as filamin [38, 39] and actinin [40]. When compared to the force generation ability of myosin, it is unlikely that these rare high-force changes associated with complete domain unfolding play a major role in mechanotransduction.

Considering the close relationship between protein structure and function, it does not take a large conceptual leap to perceive how ~pN forces might impact protein conformation, and thus function. However, based on the available data on protein mechanics, forces in cells are likely sufficient to mechanically activate some, but not all load bearing proteins. This specificity is likely important for selective mechanosensitive signaling.

2.2.2 Protein responses to mechanical loading: catch and slip bonds

In considering the molecular mechanisms of cellular mechanosensitivity, it is important to bear in mind the physical principles that mediate force-induced

conformational changes in proteins. When proteins or protein complexes are subject to mechanical loads, the resulting structural changes can serve to either reinforce or dissociate interacting domains. To describe these divergent responses, two general classes of molecular bonds have been defined (Figure 2.2). In most molecular bonds, referred to as slip bonds, the application of load decreases the lifetime of the bond. In this class of bond, applied load typically results in the separation of key contact interfaces, reducing their ability to interact, and resulting in decreased bond lifetime. Thus, weak slip bonds are expected to be perturbed during force-induced conformation changes in protein structure. The resulting changes in protein conformation are likely associated with the tilt or slight deformation of a particular protein domain. In other cases, applied load can increase the lifetime of a bond. This class of bond is called a catch bond. In this type of bond, loads applied to a protein cause conformation changes or other events that result in the decreased distance of key interaction groups or results in the formation of new interactions. This increases the overall energetic favorability of the interaction and lengthens the bond lifetime. However, at very large forces key interactions are eventually perturbed, causing domain separation and the dissociation of the bond. Therefore, these bonds are also referred to as catch-slip bonds. As we examine in the following sections, these two distinct types of molecular bonds serve distinct purposes in mechanosensitive signaling mechanisms.

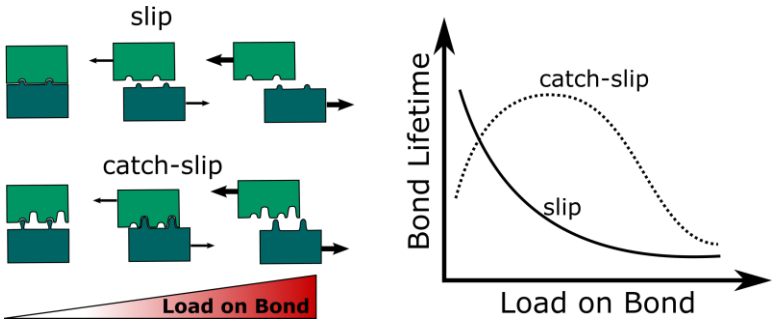

Figure 2.2: Types of molecular bonds. Slip and catch-slip bonds mediate protein conformation and protein-protein interaction lifetimes (strength). Slip bond lifetimes decrease as a function of applied load, while catch-slip bond lifetimes initially increase at low force, but eventually dissociate at higher loads.

2.2.3 Mechanosensitivity as a four-step process

Conceptual descriptions of mechanosensitive processes, typically describe four fundamental steps (Figure 2.3). These steps are based on the central premise that specific structures within the cell are particularly sensitive to mechanical stimuli. Thus, forces must first be transmitted to these specialized structures. Often, increased loading of these structures causes a force-induced change in the conformation of a mechanosensitive protein, enabling conversion of the mechanical stimuli into a biochemically-detectable signal. Sensing of this signal then elicits a detectable response in a signaling pathway, gene transcription, or cell behavior. These four stages are often referred to as mechanotransmission, mechanotransduction, mechanosensing, and mechanoresponse [16]. While other nomenclatures exist [17] they each describe the same set of conserved processes.

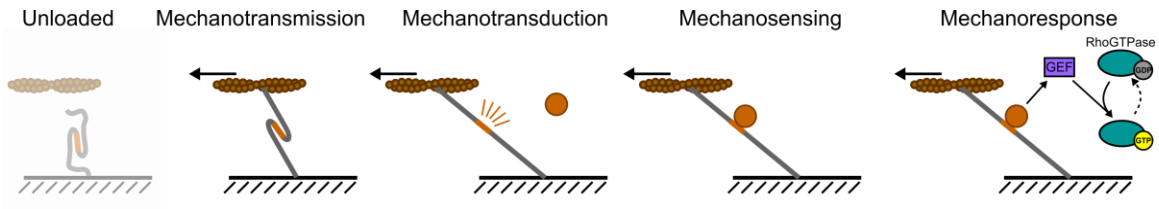

Figure 2.3: Molecular events underlying cellular mechanosensitivity. In an unloaded state, a cryptic binding site (orange) is hidden within a protein's 3D structure. Physical connection to a cytoskeletal structure (actin) facilitates mechanotransmission through that protein. At higher forces, the protein undergoes a conformational change, transducing force into a biochemically detectable event (revealing of the cryptic binding site). Subsequent sensing of the signal by a protein with an affinity for the once-cryptic binding site produces a downstream mechanoresponse that activates a Rho-GTPase signaling cascade.

2.2.3.1 Mechanotransmission

Mechanotransmission refers to the transfer of mechanical loads along elastic elements [41]. On a molecular level, the ability of proteins and protein-protein interactions to resist mechanical loading impacts the degree of mechanotransmission to specialized mechanosensitive structures. In the absence of mechanical connections, mechanosensitive signaling does not progress. In cells, due to physical linkages between the ECM and a mechanically active cytoskeleton, forces can be transmitted between the intracellular and extracellular environments [42]. These linkages enable the cell to physically manipulate its environment, mechanically integrate with its surroundings, and migrate [43]. Additionally, due to the stiff and filamentous nature of several cytoskeletal elements, particularly F-actin and microtubules, forces can be transmitted over long distances, relatively quickly in comparison to effects mediated by protein diffusion [44]. For instance, forces applied at the plasma membrane can lead to Src activation at the opposite side of the cell within 300 ms [45, 46].

Often, protein-protein interactions expected to be important in mechanotransmission act as catch bonds. This class of bond will increase the length of time that loading can be maintained, providing increased opportunities for the detection and amplification of mechanosensitive signaling. Single molecule experiments involving an AFM or magnetic tweezer-based apparatus have been used to directly demonstrate that applied loads prolong bond lifetimes between actin monomers and actin filaments [47], actin and myosin [48], and $\alpha_5\beta_1$ integrin and fibronectin [49], all of which are thought to enhance mechanotransmission. In the case of $\alpha_5\beta_1$ integrins and the ECM protein fibronectin, binding is enhanced by exposure of an additional binding site, called the synergy site, on fibronectin [50]. Such force-stabilized interactions are likely to have large, but indirect, effects on mechanosensitive signals.

2.2.3.2 Mechanotransduction and mechanosensing

While the term mechanotransduction is frequently used as a catch-all term to describe mechanosensitive processes in cells, it also refers to a specific step in the series of events from force transmission to cellular response. Transmitted forces ultimately impinge upon a mechanosensitive protein or protein complex, causing biochemically detectable changes [51]. Thus, transduction and sensing are conceptually distinct, but inherently linked. Mechanotransduction refers to the direct conversion of mechanical forces into a biochemically detectable signal, while mechanosensing describes the subsequent detection of this signal [51]. These are often considered to be implicitly linked, as many of the principles underlying mechanotransduction were first

determined by studying mechanically-activated ion channels [52]. In this context, transduction and sensing occur virtually instantaneously due to conformational changes in the channel and subsequent flow of ions. In other subcellular structures, mechanosensing is most often accomplished through the creation of novel, force-dependent protein-protein interactions. Although specific examples will be discussed later, a common scenario involves the force-induced exposure of a cryptic binding site or signaling domain that is typically buried within the protein's structure [18, 53]. Structural or signaling proteins then sense this conformational change, resulting in mechanical reinforcement or phosphorylation events [19].

2.2.3.3 Mechanoresponse

Mechanoresponse refers to the downstream effects of the sensing of applied load. Since mechanosensing often involves the formation of novel protein-protein interactions, a natural downstream effect of this is the structural reinforcement of load-bearing structures by these newly recruited proteins. This type of force-induced structural reinforcement is often referred to as adhesion strengthening and has been observed in multiple subcellular structures including focal adhesions [54] and adherens junctions [55]. Another consequence of the creation of novel protein-protein interactions is the activation of signaling cascades, which often feedback to directly modulate cellular contractility through the Rho-family of GTPases [56, 57]. On longer time scales (minutes to hours to years in the case of some mechanosensitive diseases), mechanoresponse refers to the sustained activation of mechanosensitive signaling pathways and

subsequent changes in gene expression. Mechanoresponse is especially evident in larger-scale phenomena such as the thickening of artery walls [2] and ventricular hypertrophy [58] in response to prolonged elevated blood pressure. Other mechanoresponses include the role of low shear stress in the induction of atherosclerotic lesions, stiffness-dependent cell cycle control in cancer, and bone resorption in response to stress shielding [28]. Overall, cellular mechanosensitivity is a highly integrated process that spans a wide range of length and time scales but is mediated by force-sensitive interactions between individual molecules.

2.3 Focal adhesion structure and function

Focal adhesions (FAs) mechanically integrate cells with their microenvironment and are one of the primary subcellular structures implicated in cellular mechanosensitivity [43]. FAs serve as a responsive physical connection at the interface between the force-generating actomyosin machinery inside the cell and the source of mechanical stimulation and physical support, the extracellular matrix (ECM). The molecular composition and architecture of individual FAs is tightly regulated, time-varying, and closely linked to FA load transmission and signaling functions. Recent advances in identifying multiple molecular species at high spatial and/or temporal resolution have clarified the role of specific FA proteins in the dynamic process of linking integrins to the actin cytoskeleton.

2.3.1 Compositional complexity

FAs are comprised of a multitude of molecular components that serve both structural and signaling roles. This compositional complexity supports a variety of functions, as the removal of any single FA component has been shown to disrupt FA assembly [59], cell migration [60], matrix rigidity sensing [61], among others [62]. Generally, FA components can be grouped into three categories, namely adhesion, structural, and signaling proteins. Adhesion proteins, which mediate cellular connections to the ECM, primarily refers to integrins, although other cell surface receptors have been identified [63]. Integrins are heterodimeric, transmembrane proteins whose binding affinity for the ECM ligands is conformationally regulated by extracellular signals, intracellular signals, and mechanical forces [64-66]. Following integrin activation, a network of structural and signaling proteins form on the cytoplasmic domain of integrins, eventually linking to the actin cytoskeleton (Figure 2.4) [67]. Structural proteins include adaptors, which link FA components together as well as actin binding proteins, which connect directly to the actin cytoskeleton. Signaling proteins such as kinases and phosphatases, as well as GTPases or GTPase regulatory proteins modulate protein-protein interactions and participate in downstream signaling cascades. However, these two categories are not mutually exclusive, and many FA proteins are required for both structural and signaling functions.

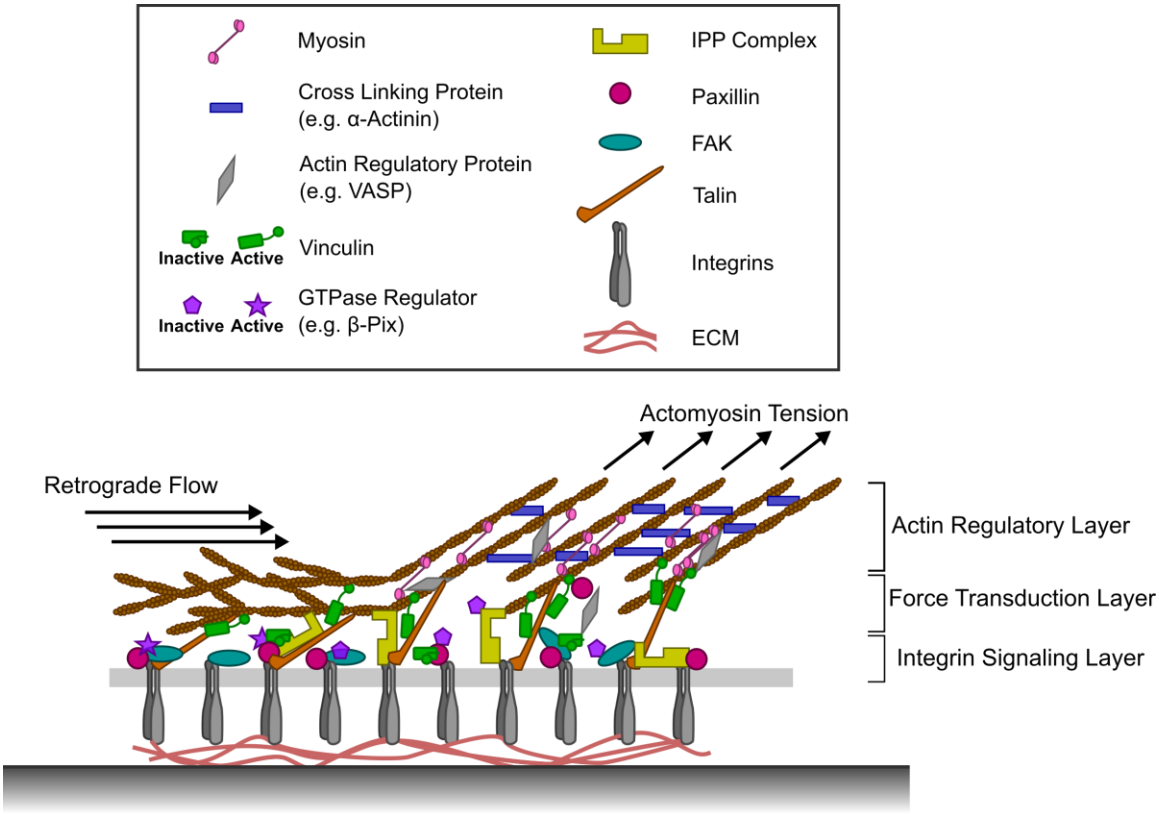

Figure 2.4: Hierarchical organization and molecular complexity in FAs. FAs are multimolecular protein assemblies that serve as connections between the actin cytoskeleton and the ECM. Integrins, heterodimeric receptors for various ECM components, connect via multiple structural and signaling proteins to the actin cytoskeleton. The stratified organization of FAs has led to the definition of three distinct layers, which mediate integrin signaling, force transduction, and actin regulatory functions [68, 69]. Forces borne by various FA components originate from two distinct actin motions: the "flow" associated with actin polymerization in the cell periphery (left) and actomyosin tension which is transmitted to FAs via stress fibers (right).

Proteomics and other systems-level investigations [70] have provided valuable perspective on the molecular diversity contained within FAs. One of the first studies to provide a global examination of the "integrin adhesome" network identified 156 unique components based on curated protein-protein interaction data from both online databases and published literature [67]. This spurred investigations that identified, based on systems-level siRNA screens and proteomic analyses of FAs, multiple

functional [59-61] and force responsive [71-74] elements in this network, expanding this number to 232 [62]. Most recently, attempts at simplifying this signaling network to its core components have led to the definition of a core "consensus integrin adhesome" [75]. The core adhesome consists of 60 proteins that were found to be enriched on fibronectin-coated substrates over some negative control ligand in at least 5 of 7 independent datasets [75]. Further bioinformatic analysis of the core adhesome showed that 34 of these proteins have >1 binding interaction with other core components or with actin, suggesting they play integral roles in the adhesion machinery [75]. This interaction data also guided the grouping of these proteins into four signaling axes centered around talin-vinculin, FAK-paxillin, ILK-PINCH-kindlin, and α-actinin-zyxin-VASP nodes [75]. Given the daunting molecular complexity of FAs, this work was critical to refining and focusing the problem, providing targets for future study.

2.3.2 Hierarchical 3D structure

FAs form three-dimensional structures on the intracellular surfaces of integrins, detectable by both atomic force microscopy [76] and cryo-electron tomography (cryo-ET) [77]. The molecular details of sub-adhesion structures have been revealed using interferometric photoactivated localization microscopy (iPALM). This technique combines multi-phase interferometry with PALM, providing information on 3D protein localization with sub-20nm accuracy [78]. Visualization of 3D FA structure with iPALM revealed a stratified layering of specific types of FA proteins [68]. Based on this work, FAs appear to be comprised of at least three layers: an integrin signaling layer, a force

transduction later, and an actin regulatory layer (Figure 2.4). Consistent with previous work with cryo-ET [77], the actin regulatory layer was found to be the furthest removed from the ECM and contained actin binding proteins such as VASP and α-actinin. Furthermore, proteins thought to be important for mechanotransduction and adhesion strengthening, including talin and vinculin, localize to the force transduction layer. Finally, proteins classically involved in the first events of integrin signal transduction, including FAK and paxillin, were found in the membrane-proximal integrin signaling layer. Interestingly, these three sets of proteins were also identified in bioinformatic analyses of the integrin adhesome [75], further suggesting that they constitute functional units

The stratified molecular architecture within FAs observed using these 3D microscopy techniques has important implications for mechanotransduction. While such stratification likely arises due the self-assembly of proteins with defined binding partners, the resulting compartmentalization could also serve to separate proteins into distinct layers or, conversely, bring proteins together that would normally not interact. Furthermore, these observations strongly suggest the existence of multi-molecular force transmission through focal adhesions, as few proteins (only talin) have been observed to physically span the gap between integrins and the actin cytoskeleton. However, other techniques are needed to directly measure when and where loads are borne by FAs and individual FA proteins.

2.3.3 Cytoskeletal regulation of FA dynamics and maturation

FAs undergo dynamic alterations at the molecular level that manifest as changes in overall shape and movement of the FA, including growth, sliding, and disassembly. Based on their size, composition, and location within the cell, FAs are frequently classified into three categories: nascent adhesions, focal complexes, and mature FAs (Figure 2.5) [79]. However, these distinct types of FAs are defined by more than just their physical appearance. These classes are distinct in their connectivity to various actin architectures, myosin II-dependent force sensitivity, and molecular composition. As such, it is important to understand the upstream regulators of these various FA types, and the tools available to researchers that enable modulation of cytoskeletal structures and cellular contractility.

2.3.3.1 Differential regulation of cytoskeletal structures by Rho and Rac

The Rho-family of small GTPases are potent regulators of cytoskeletal structures and cell contractility [80-82]. These proteins are active when bound to GTP, but have intrinsic enzymatic GTPase activity that serves to inactivate them over time [83]. In an active, GTP-bound state, these proteins interact with a host of downstream effectors, which then mediate numerous cellular responses including adhesion, cytoskeletal assembly, migration, and division [83, 84]. Due to their roles as master-regulators of the actin cytoskeleton, a number of FRET-based biosensors have been developed to monitor the activity of these key GTPases through time [85, 86], shedding light on their differential activation through complex mechanical processes like protrusion [87-89], cell

migration [90], and division [91]. While numerous Rho GTPases exist and play prominent roles in mechanical processes in cells, RhoA and Rac1 play particularly important roles and are frequently examined in mechanobiological contexts [82, 83].

RhoA and Rac1 are mutual antagonists and are generally thought to regulate the formation of actin stress fibers and lamellipodial protrusions, respectively. RhoA acts through two main signaling axes, driving (1) myosin II activity and cell contraction through Rho-associated protein kinase (ROCK) and (2) actin polymerization through mDia [82, 92]. Both of these signaling axes augment the formation of prominent actin stress fibers and large, mature FAs [93]. Direct modulation of RhoA activity can be accomplished experimentally through the transient expression of its constitutively-active form (V14-Rho), which impedes its GTPase function, leaving it perpetually loaded with GTP. Additionally, several small molecule inhibitors of downstream effectors of RhoA have allowed for the more precise tuning of RhoA activities. Most notably, Y-27632 inhibits ROCK activity, perturbing the activation of myosin II motor function, but leaving its crosslinking function intact. Other small molecules, such as blebbistatin, inhibit both the motor and crosslinking functions of myosin, making experimental results with these difficult to interpret. Rac1 on the other hand, through a number of effector proteins [82], facilitates the formation of lamellipodial protrusions [94]. Like RhoA, point mutation of Rac1 (V12) can lead to a constitutively active form that facilitates the formation of broad lamellipodia and membrane ruffles. Although RhoA and Rac1 are not known to be outright mechanosensors, a number of proteins that

directly control their activity, particularly GEFs and GAPs, localize to FAs and are regulated by force [83]. However, many of the details underlying this balance between forces, RhoGTPase signaling and cytoskeletal organization are still a subject of debate [83, 95].

2.3.3.2 FA formation, maturation, and attachment to actin architectures

Nascent adhesions form at the cell periphery as a cluster of activated integrins bound to ECM ligand. These small adhesions (<0.2 μm^2) are associated with cell protrusions, namely lamellipodia, which are rich in Arp2/3-dependent branched actin structures (Figure 2.5). Together with their small size, their transient stability (on the order of seconds) makes nascent adhesions relatively difficult to study or characterize molecularly. While different mechanisms may underpin the initial binding of αv [96] and α5 [97] class integrin clusters to fibronectin, the resulting complex is driven rearward towards the cell body at a rate correlated with the speed of cell protrusion, suggesting a critical role for actin-based retrograde flow [97].

At the lamellipodia-lamellum interface, nascent adhesions either disassemble or engage an actin bundle, which initiates a rapid growth phase and continued translocation of these slightly larger (0.2 – 1.0 μm^2) adhesion structures, termed focal complexes, into the cell body (Figure 2.5). The continued maturation and stability of focal complexes depends on myosin II. However, whether myosin's motor activity or cross-linking function that facilitates focal complex stability and maturation is still a matter of debate [98]. As with nascent adhesions, dynamic frictional forces associated

with actin retrograde flows serves to load focal complexes and are frequently implicated in their force-dependent maturation [99]. The concept of adhesion structures serving as molecular clutches was first evident observing focal complex force generation and actin retrograde flows (Waterman-Storer). Engagement of these adhesions with the actin cytoskeleton slows the retrograde flow of actin, while at the same time increasing the rate of lamellipodial protrusion.

Maturation of focal complexes into full-fledged FAs results in visible linkage to an actin stress fiber (SF) as well as further compositional changes, with more adaptor proteins and cytoskeletal regulators, especially LIM-domain containing proteins, being recruited to the structure (Figure 2.5) [73]. The force sensitivity of this stage is traditionally associated with the application of relatively static stresses to the FA, as maturation can be induced by both increases in actomyosin contractility or application of static stress external to the cell [97, 100]. Finally, measurements at high spatial and temporal resolution have revealed that stresses are not evenly distributed across an individual FA and are not necessarily constant in time [101]. Together, these findings suggest that both static stresses transmitted through stress fibers, and dynamic frictional forces likely associated with changes in actin retrograde flow, induce FA maturation in a myosin-dependent manner.

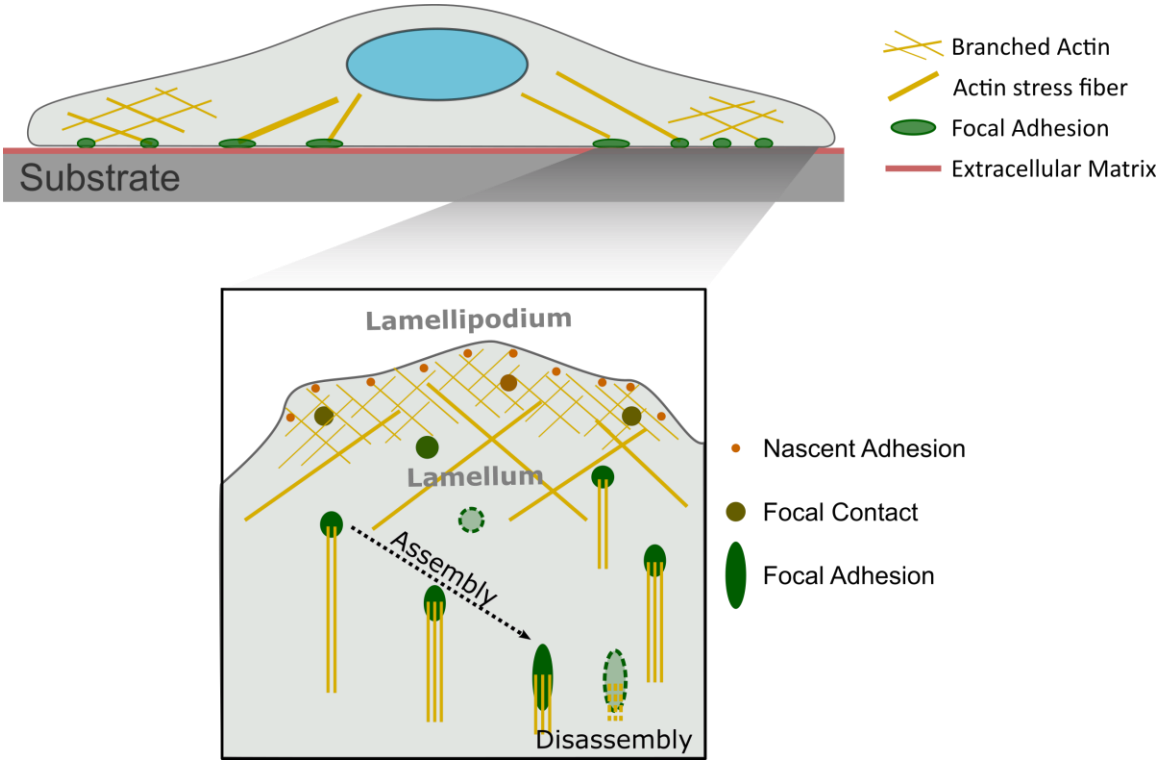

Figure 2.5: FAs undergo dynamic molecular rearrangements during their assembly and disassembly. FAs are dynamic subcellular structures that physically connect the ECM to cytoskeletal structures like stress fibers (top). The formation, maturation, and translocation of FAs towards the cell body is driven by forces from the actomyosin cytoskeleton and is accompanied by alterations in FA composition (shades of orange and green) as well as size, shape, and subcellular location changes.

2.3.4 Force-dependent signaling

FAs act as force-dependent signaling hubs, transducing mechanical information into biochemical signals that control diverse cellular functions. Analogous to other classical post-translational modifications, force-dependent signals are thought to be induced by the force-induced exposure of a cryptic binding or signaling domain that is buried within the protein's structure [18, 53]. Subsequently, signaling proteins sense this conformational change, often resulting in changes in binding partners, catalytic activity or dynamics [19].

Many studies into the mechanisms FA force-dependent signaling have documented the important role of protein kinases, their activation, and force- or adhesion-dependent phosphorylation events [102]. For example, force-induced unfolding of p130Cas exposes a substrate domain which contains multiple Src phosphorylation sites [19]. Furthermore, internally generated forces and changes in external mechanical cues have profound effects on phosphorylation in FAs [49], suggesting a link between applied forces and protein tyrosine kinase (PTK) activity [61]. Indeed, several protein PTKs are well-known to associate with FAs and mediate phosphorylation events that appear to be sensitive to forces [102, 103]. Force-dependent changes in phosphorylation could occur due to variations in kinase residence times in FAs [104] or the exposure of cryptic phosphorylation sites in kinase substrates [19]. Mechanically, PTK activity has been linked to alterations in FA dynamics initiating FA disassembly processes [105] and cytoskeletal remodeling. Additionally, force-dependent PTK activities in FAs could explain the potent regulation of growth and metabolic responses to physical cues [7, 106].

Mechanical cues also influence differentiation, implicating FAs as having a regulatory role in transcription [4]. Recent work has highlighted the mechanosensitive activation and translocation of several transcriptional co-activators. Notably, extensive experimental evidence suggests that mechanical cues are potent regulators of the transcriptional co-regulators YAP and TAZ. YAP/TAZ activity is classically understood in the context of the Hippo signaling pathway [107], but is also exquisitely sensitive to a

variety of physical cues [108]. Specifically, ECM stiffness and cell spread area appear to link YAP nuclear translocation to differentiation in human mesenchymal stem cells [25]. Additionally, and cell confluence and shear flow have been implicated in YAP-mediated atherogenesis[109, 110]. Even more recent work discovered evidence for a potential unifying mechanism for YAP mechanosensitivity in which nuclear deformation alone enables YAP/TAZ translocation into the nucleus [111]. Besides YAP/TAZ, the transcriptional co-activators MRTF/MAL-A play an important mechanosensitive role in the differentiation of epidermal stem cells [112]. Finally, activation of the transcription factors in ternary complex factor (TCF) sub-family have also been implicated in cell shape-dependent regulation of gene expression [113].

2.4 Force transmission through focal adhesions

2.4.1 Measuring force transmission at the cellular and molecular levels

In light of early observations of cellular mechanosensitivity and evidence for force as a potent regulator of multiple cellular functions, several techniques have been established to probe cell-generated forces at both the cellular and molecular levels. The two most prominent are traction force microscopy and, more recently, FRET-based molecular tension sensors. While both tools provide force measurements in dynamic cellular systems, they function at vastly different length scales. Thus, each technique provides distinct but complimentary biophysical insight into cell force generation and mechanosensitive processes (see Figure 2.6 for illustrative comparison).

2.4.1.1 Measuring forces at the cell-substrate interface: traction force microscopy

Traction force microscopy (TFM) refers to a suite of techniques were developed to probe the magnitude of cell-generated forces on engineered substrates. Even before the development of quantitative TFM methods [114], cellular traction forces were evident from observations of cell wrinkling of silicone rubber substrata [115]. Quantitative TFM techniques rely on measurements of fiducial marker displacements in engineered substrates (Figure 2.6A). Combined with information about the mechanical properties of these elastic materials, lateral displacement measurements can be used to back-calculate the cellular traction forces. The most popular platforms for TFM include deformable hydrogels [114], micropatterned substrates [116, 117], and microfabricated devices [118-120]. Notably, all of these TFM techniques allow for modification of substrate stiffness, enabling investigations of cellular rigidity sensing [121-123], durotaxis [26, 101], and other stiffness-dependent processes [124, 125].

Although TFM techniques have most commonly been used to probe the entire force output of a single cell or study the spatiotemporal variations in cell contractility, recent advances have led to the extension of this technique to more complex systems. For example, extrapolation of TFM techniques to three dimensions has revealed out-of-plane normal and rotational forces about FAs [126] and suggests that cells can exert forces of similar magnitude in all directions [126, 127]. Furthermore, precise TFM measurements with spatial resolutions on the order of microns and sub-second temporal resolution have revealed highly variable "tugging" forces on individual FAs [101]. These

tugging events were shown to be dispensable for cell migration up a chemotactic gradient, but required for durotaxis, suggesting a critical mechanosensory function. Finally, TFM techniques developed for multicellular systems have indicated long-range mechanical connectivity between cells in migrating layers [128, 129].

Overall, traction force techniques have led to important insights into the regulators and spatiotemporal dynamics of cell contractility and rigidity sensing but are limited in that they only measure forces at the cell-ECM interface.

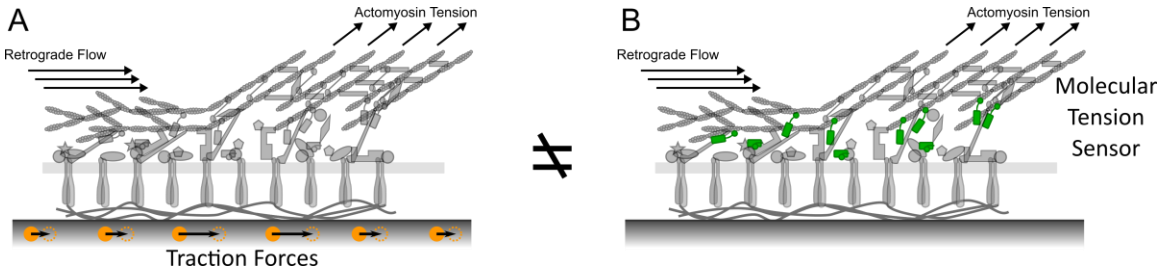

Figure 2.6: Traction forces and molecular tension are not equivalent. Due to multiple molecular linkages connecting the intra- and extra-cellular environments, TFM and molecular tension sensor measurements of cell-generated forces cannot be assumed to be equivalent. (A) TFM measures the total force output from a given cell or FA structure based on lateral displacements in the underlying substrate. (B) Molecular tension sensors report loads borne by individual proteins on the intracellular face of FAs (in this illustration, vinculin is highlighted as the molecular linkage of interest).

2.4.1.2 Measuring molecular-scale forces inside cells: FRET-based tension sensors

More recently, interest has emerged in determining the molecular-scale mechanisms cells use to detect and respond to mechanical cues. Based on work with purified proteins in vitro, these mechanisms were thought to involve force-induced changes in protein conformation and thus function (see Chapter 2.2.1). One well-studied mechanosensitive interaction involves the FA proteins talin and vinculin. In vitro,

stretching talin reveals cryptic binding sites for vinculin, indicating a mechanism by which vinculin could reinforce talin-actin linkages in a force-dependent manner [18]. However, important questions remained. When and where is talin loaded inside cells? Do cells exert large enough forces on talin to elicit these force-sensitive interactions? These types of questions, and many other interesting in vitro results, led to an overwhelming interest in visualizing and quantifying the forces experienced by specific proteins in living cells.

Measurements of the molecular-scale deformations in living cells were made possible by the development of biosensors based on Forster resonance energy transfer (FRET) [130, 131]. FRET is a process by which energy is non-radiatively transferred between an excited donor fluorophore and an adjacent acceptor fluorophore [132]. The amount of FRET that occurs is sensitive to the photophysical properties, relative orientation, mobility, and, importantly, the separation distance of the fluorophores. Changes in FRET can be measured through a number of microscopy techniques, including an increased acceptor to donor emission ratio (two-color FRET) or a decreased donor lifetime (FLIM). By assuming that the fluorophores diffuse randomly and have no preferred orientation, the FRET efficiency (E) can be described by the simple equation $E = (1 + (r/R_0)^6)^{-1}$, where R_0 is the Forster radius, or the fluorophore separation distance at which 50% FRET efficiency is achieved, and r is the separation distance of the two fluorophores [132]. Several groups have created biosensors which take advantage of the strong distance dependence of FRET to measure displacements within, and thus

tension across, specific proteins of interest. Most tension sensors are based on a module (Figure 2.7A), comprised of two fluorophores separated by an elastic linker, which can be inserted into a target protein (ex. vinculin, Figure 2.7B). As a load is applied across the protein, the donor and acceptor fluorophores separate and FRET decreases (Figure 2.7C), visualization of ~pN forces across single proteins in living cells [133-135].

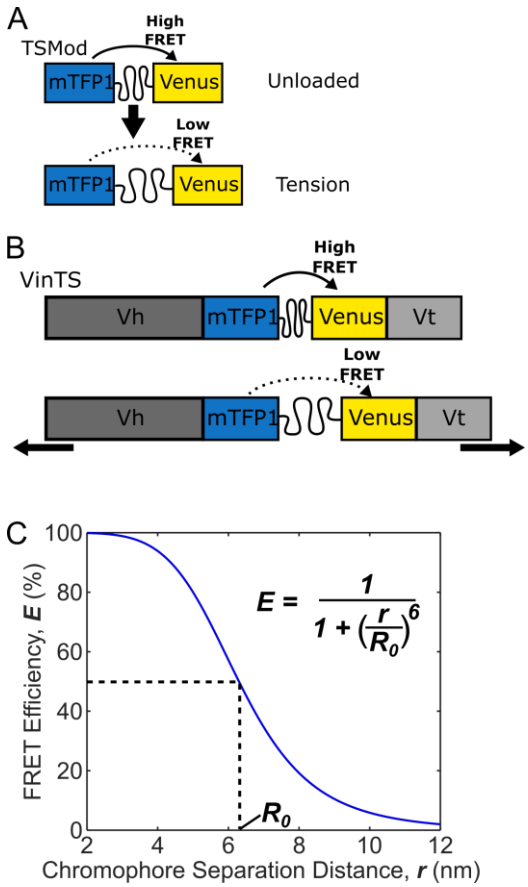

Figure 2.7: FRET-based molecular tension sensor function. A tension sensor module (TSMod, panel A) consists of a donor and acceptor fluorophore, separated by a spring-like polypeptide linker. When subject to mechanical loads, as would occur upon genetic incorporation into a protein of interest (Vinculin, panel B), FRET decreases sharply as a function of fluorophore separation distance (C).

By measuring the spatiotemporal distribution of loads through individual proteins in FAs and other cytoskeletal structures, one can start to unravel the

mechanisms underlying mechanically-sensitive phenomena such as ECM remodeling, and adhesion assembly and disassembly. For example, a fibronectin strain sensor showed reversible domain unfolding in response to cellular-generated forces [136] that reveals cryptic motifs thought to regulate fibrillogenesis [137]. This result links intracellularly-generated tension through a molecular unfolding event to a remodeling outcome. A vinculin tension sensor was used to establish that vinculin load bearing is a switch that dictates whether FAs assemble or disassemble in response to applied load [131]. Additionally, an actinin tension sensor, using a slightly different design based on an α-helix was used to show that forces are highest across actinin in migrating cells [130]. Also, a FRET-based sensor was designed that was capable of reporting unfolding between the 20-21 Ig domains in the actin cross-linker, filamin, in response to internally generated forces [138]. Interestingly, 20-21 Ig domain unfolding, like tension across vinculin and actinin, was concentrated at the leading edge of migrating cells, supporting a mechanism through which tension across filamin releases FilGAP [56], inhibiting Rac activation in leading edge protrusions. Finally, the recent development of multiple talin tension sensors has revealed interesting features of cell rigidity sensing [139, 140]. Both groups found that talin bears significant loads (sometimes > 10pN) in FAs and that these loads are dependent upon the stiffness of the underlying substrate. Additionally, these talin tension sensors enabled investigations of talin tension-dependent vinculin reinforcement events previously restricted to in vitro single molecule settings. Together, talin's stiffness-dependent loading and subsequent tension-dependent recruitment of

vinculin point to talin as a critical mechanotransducing element in FAs (see Chapter 2.2.3).

The continued development and use of molecular tension sensors will provide more unique, molecularly-specific views into load transfer through cytoskeletal structures and FAs. While initial studies using molecular tension sensors have provided valuable insight into the magnitudes and spatiotemporal variations in protein loading, the full potential of FRET-based molecular tension sensors is only just beginning to be realized.

2.4.2 Biophysical control of FA loading and cell contractility

Numerous mechanosensitive mechanisms allow cells to perceive the physical properties of their microenvironment (e.g. stiffness, ECM density) as well as respond to mechanical perturbations (e.g. cyclic stretch, shear flow). Changes in substrate stiffness alone can modulate cell survival [7], drive the epithelial-to-mesenchymal transition [14, 141], or initiate changes in transcription leading to differentiation [13, 142]. Importantly, these relatively slow processes are preceded, and likely driven by numerous mechanical changes within the cell, including changes in cell contractility as well as the assembly of cytoskeletal and adhesion structures. What links ECM stiffness to changes in cell mechanical state however, is still unclear. The importance of Rho and Rac has been established [27], but the signals causing their differential activation downstream of various mechanical inputs are still being elucidated. The biophysical regulation of protein loading and the important role of molecular scale forces in these processes must

therefore be further studied and is just becoming apparent using FRET-based molecular tension sensors. In the following sections, we examine evidence for biophysical regulation in two frequently-investigated phenomena from both a macroscopic and the more recent molecular perspective: (1) the force-dependent growth of FAs and (2) the stress-control and strain-control paradigms of cell contractility.

2.4.2.1 Force-dependent growth of FAs

Despite an extensive body of work detailing FA growth and disassembly cycles and feedback through Rho and Rac to modulate actomyosin structures, little is known about how FA structure and morphology dictate force transmission into and out of the cell. Observations of force-dependent FA growth imply a relationship between force and FA morphology. Early work employing multiple TFM techniques found a correlation between FA size and force, indicating constant stress across single FAs [117, 118, 124, 143]. While these findings may hold true for single FAs formed on microposts or micropatterned ECM, subsequent work on flat substrata showed a more complex relationship between FA size and stress. Beningo et al. found an anti-correlation between FA size and stress, but only at the leading edge of migratory cells in presumably assembling FAs [144]. Others found large super-mature adhesions exhibited highest traction stresses [145]. Still others have examined the critical role of actin retrograde flow in loading adhesions and found a biophasic response between actin speed and traction stress, highlighting the clutch-like function of FAs in cell protrusion

[146]. As of yet, descriptions of FA structure and dynamics in relation to their load-bearing capacity only hold true for specific FAs in a context-dependent manner [147].

The divergent role of force at FAs is also apparent when examining cell migration processes. Directional cell migration requires cell polarization followed by strong adhesion at the leading edge of a cell, contraction of the actin cytoskeleton to pull the cell body forward, and deadhesion at the rear [148, 149]. However, forces transmitted to the underlying substrate are equally high at both the leading and trailing edge of cells [114]. Somehow equivalent forces lead to assembly and adhesion at the front, and disassembly and deadhesion in the rear. While there are important biochemical regulators in this process, for example the calpain mediated cleavage of talin [150] or phosphorylation of FAK [105], considering which molecules are bearing these bulk traction forces also provides insight into the biophysical regulation of cell migration. Specifically, using a tension sensor that reports loads across vinculin in FAs, it was shown that if bulk forces through FAs are borne by vinculin, FAs assemble, whereas if they pass through some other force transmission pathway, FAs tended to disassemble [131]. Thus, tension across vinculin is a critical determinate of the dynamic or signaling state of FAs.

2.4.2.2 Stress-control versus strain-control

Stiffness sensing describes the process by which a cell interrogates the mechanical properties of its surroundings. In principle, this process involves the cell first pulling (or sometimes pushing) on a material and subsequently detecting some quantity

related to material stiffness. Considering that stiffness, or more precisely elastic modulus, is defined as the ratio of stress to strain, this means that a cell could measure stiffness by applying a constant stress and detecting the resultant strain in the material. However, the reverse operation is also possible: application of a constant strain and detecting the resultant stress required to reach that strain also provides an equivalent measurement of mechanical properties. These two distinct paths to measuring substrate stiffness have been designated by the variable which a cell controls, namely, stress-control and strain-control [151-153].

Evidence for strain-controlled rigidity sensing comes mainly from qualitative observations of increased cell contractility on stiffer substrates. In order to generate the required forces, cells assemble larger, more static FAs, increase myosin activity, and create more robust actin stress fibers. Because stiffer substrates cause more contractile, stiffer cells, strain control has also been referred to as "tensional homeostasis" [27]. The studies that have directly investigated strain-controlled rigidity sensing showed that this control paradigm occurs most often in softer substrates in physiological stiffness regimes [119, 121, 123, 154]. Importantly, these observations implicate the cell itself as a mechanosensor rather than the subcellular structures or proteins frequently implicated in and required for rigidity sensing [15].

The main evidence for stress-controlled rigidity sensing comes from the correlations between force and FA area observed using TFM, indicating a constant stress within these structures [54, 117, 118, 143]. However, as discussed above, these results

mainly hold for certain cell types in a context-dependent manner. Additionally, since TFM infers cell contractility based on principles derived from continuum mechanics, it is unknown the extent to which these bulk forces translate to the molecular level. Ultimately, bulk forces transmitted through FAs are borne by discrete molecular linkages within these structures. Thus, considering the likely scenario that rigidity sensing is mediated locally by protein deformations in load-bearing structures like FAs, further investigations into the mechanisms of rigidity sensing will need to employ molecular tension sensors (and is the topic of Chapter 4 of this dissertation).

2.5 Vinculin as a model mechanosensitive protein

Many of the molecular processes that underlie molecular mechanotransduction have only been observed in vitro, in tightly controlled experimental conditions involving purified proteins or protein fragments. While these studies have provided unique insight into the loads required to regulate protein conformation, the extent to which these findings translate to intracellular environments has yet to be confirmed. Elucidation of the cellular and molecular determinants of protein loading, and the subsequent effect of force-mediated biochemical interactions is therefore of great interest. Driving this research are molecular tension sensors, which have been developed to probe the loads borne by a variety of proteins (reviewed in [155]). Among the known mechanosensitive proteins, vinculin plays a prominent role in force transmission at FAs and is essential to many cell and tissue level mechanosensitive processes. In addition to

providing rationale for choosing this protein, the following sections describe the current understanding and remaining questions regarding vinculin's critical roles in FA structure, force transmission, and cellular mechanosensitivity.

2.5.1 Vinculin structure and regulation

Structurally, vinculin is comprised of a globular head domain, which connects via a flexible proline-rich linker and strap region, to an F-actin binding tail domain [156]. In the cytosol, vinculin resides in an auto-inhibited state characterized by strong head-tail interactions that prevent vinculin's interactions with other molecules [157]. Only upon recruitment to FAs, via either PIP2-mediated [158] or FAK-paxillin pathways [159], does vinculin become activated. After recruitment and activation, vinculin interacts with many other key FA proteins including talin [160], α-actinin [161], paxillin [162-164], HIC5 [165], VASP [166], ponsin [167], vinexin [168], Arp2/3 [169], and F-actin [170], among other partners [75] (Figure 2.8). A number of these binding partners have been implicated in the activation of vinculin itself, including talin and α-actinin in the head domain, as well as F-actin and the phospholipid PIP2 in the tail domain [69, 156, 171, 172]. It is likely that the coincident binding of two or more of these molecules drives full vinculin activation [156]. Interestingly, while vinculin recruitment to FAs likely occurs via membrane-proximal components like PIP2 or phospho-paxillin, vinculin resides higher (further away from the plasma membrane) in more mature FAs. This vertical shift in vinculin position was shown to occur in a talin-dependent manner [69],

indicating the regulation of this shift could impact vinculin reinforcement of talin-actin connections.

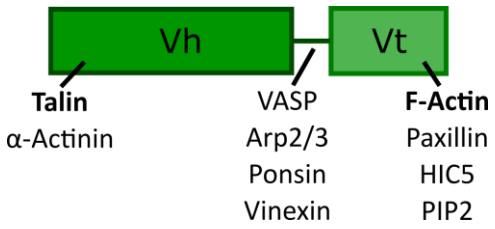

Figure 2.8: Vinculin binding partners. Upon activation, the head (Vh) and tail (Vt) domains of vinculin separate, enabling interactions with numerous binding partners to mediate downstream mechanical reinforcement and signaling events.

2.5.2 Role of vinculin in FA force transmission

One of vinculin's primary functions in FAs is to mediate force transmission from the actin cytoskeleton, through talin to integrins and the underlying ECM. While reports vary widely, vinculin -/- MEFs show somewhere between a 40% and a 5-fold decrease in traction force generation [99, 173-177]. Also, without vinculin, actin retrograde flow is dramatically increased and disorganized in the cell periphery and can only be rescued to slower rates by expressing full length vinculin with functional actin binding domain [99]. Expression of constitutively active forms of vinculin increase traction force generation [177], suggesting a role for force in stabilizing vinculin-actin connections. Indeed, recent single molecule studies have identified a directionally-specific catch bond between the vinculin tail domain and F-actin [178]. This force-induced stabilization of vinculin-actin connections could facilitate force transmission and augment conformational changes in either vinculin or talin that wouldn't occur until a higher force threshold is reached.

While vinculin's importance to cell adhesion was well-appreciated, it was only often considered a passive player. Recent work with a sensor capable of reporting forces across vinculin itself revealed a vinculin-tension dependent switch during FA assembly and disassembly processes [131]. Specifically, when vinculin bears tension in loaded FAs, the FAs assemble. However, if in response to increased mechanical loads, vinculin does not bear tension, indicating the loading of other proteins, the FAs disassemble. This could mean that distinct force transmission pathways are engaged in different FAs depending on their signaling state, location, or maturity. As vinculin is not required for FA growth [99], alternative assembly mechanisms do exist. However, without vinculin, FAs are not stabilized against applied loads, a fundamentally important process to cell migration and adhesion termed adhesion strengthening. Later work confirming this finding updated the picture of vinculin tension-dependent FA assembly to describe smaller subsets of stable FAs and FAs undergoing catastrophic disassembly [179]. The complexity of the molecular architecture on the intracellular face of integrins clearly shows why it is so difficult to relate measurements of traction force to molecular tensions within FAs (Figure 2.6).

2.5.3 Role of vinculin in mechanosensitive cellular processes

Vinculin's load-bearing capacity as well as it's multitude of binding partners ideally position it to mediate higher-order mechanosensitive processes in cells and tissues. Notably, vinculin knockout is embryonically lethal, as mice fail to survive past E10, and exhibit significant cardiac and neural defects [180]. At the cellular level,

vinculin plays a regulatory role in a variety of physical stimuli including stiffness changes, stretch and shear. Specifically, vinculin is an important regulator in the mechanosensitive differentiation of hMSCs [53], implicating vinculin as having a regulatory role upstream of transcription. Specifically, hMSCs lacking vinculin do not differentiate as efficiently towards myogenic lineages, an effect that can only be rescued by full length (capable of bearing forces) vinculin. Later work found that vinculin tension likely serves to activate transcription through the MAPK signaling axis as a force-dependent conformational shift in vinculin itself reveals a cryptic binding site for MAPK1 [181]. This may tangentially relate to a finding that differential recruitment of vinculin to FAs tunes cell sensitivity to substrate stiffness [101]. Besides differentiation, vinculin is critical to reorientation of FAs in response to cyclic stretch [182] as is essential to proper vasculature formation. Additionally, vinculin has a well-established role in linking cell shape changes to traction force [177]. The role of vinculin in coordinating cell shape changes is also central to cell migratory processes. Several studies have shown that vinculin enhances both 2D and 3D migration [176, 183, 184], and has been implicated in cancer progression [185]. Overall, this extensive collection of work indicates that vinculin is a critical and functionally important FA reinforcement element responsible for sensing and transmitting forces from the actin cytoskeleton to the ECM.

3 Tunable Molecular Tension Sensors Reveal Extension-Based Control of Vinculin Loading

3.1 Introduction

The ability of cells to generate and respond to mechanical loads is increasingly recognized as a critical driver in many fundamentally important biological processes, including migration [10, 26, 186], proliferation [7, 187], differentiation [8, 13, 188], and morphogenesis [5, 189]. While the mechanosensitive signaling pathways enabling these responses are poorly understood, most are thought to have a common basis: the mechanical deformation of load-bearing proteins [16, 190, 191]. As such, several technologies for measuring the loads borne by specific proteins in living cells have emerged [24, 134, 135]. These biosensors, collectively referred to as molecular tension sensors, leverage the distance-dependence of Förster Resonance Energy Transfer (FRET) to measure the extension of and, if properly calibrated, the forces across a specific protein of interest [133, 135, 192, 193]. For example, using this approach, the tension across vinculin was shown to regulate a mechanosensitive switch governing the assembly/disassembly dynamics of focal adhesions (FAs) [131]. While this and several other FRET-based molecular tension sensors provide a critical view into mechanosensitive processes [155, 190], fundamental questions regarding the nature and the degree of the mechanical loading of proteins remain. A key limitation has been the inability to create tension sensors with diverse mechanical sensitivities suitable for a wide variety of biological applications [193].

To date, genetically-encoded molecular tension sensor modules (TSMods), which are incorporated into various proteins to form distinct tension sensors (Figure 3.1A), have been created without a priori knowledge of their mechanical sensitivity. TSMod development has largely relied on a biologically-inspired "guess-and-check" design approach using naturally-occurring extensible polypeptides or protein domains as deformable elements in the FRET-based tension sensors. Furthermore, despite the use of these sensors to study intracellular processes, calibration measurements of their mechanical sensitivity are typically performed in vitro using highly precise single molecule techniques. Reported force sensitivities of several in vitro calibrated TSMods are 1-6 pN [131], 2-11 pN [194], 3-5 pN [195], 6-8 pN [139], or 9-11 pN [139]. However, it is unclear if these ranges are sufficient for diverse mechanobiological studies, and the applicability of these in vitro calibrations to sensors that are utilized in cellulo has not been verified.

We sought to overcome these limitations by creating new TSMods that do not rely on naturally occurring extensible domains or in vitro calibration schemes. These new TSMods consist of an improved Clover-mRuby2 FRET pair connected by unstructured polypeptide extensible domains of various lengths. As the entropy-driven mechanical resistance of unstructured polypeptides can be accurately predicted by established models of polymer extension [196], the force- and extension-sensitivities can be determined independently of in vitro calibration experiments. Using these advancements, we generate a variety of new tension sensors for the FA protein vinculin.

These include a version optimized for sensitivity, which shows a 200% increase in performance, as well as a suite of sensors with distinct mechanical sensitivities capable of determining if vinculin loading is subject to force-based or extension-based control, the molecular equivalents of stress and strain control. Lastly, we computationally predict the mechanical behavior expected for a variety of unstructured polypeptide-based tension sensors for several common FRET pairs. This resource should allow for the expedited creation and rational design of molecular tension sensors suited for diverse contexts, alleviating a significant limitation in the study of mechanobiology.

3.2 Methods

3.2.1 Cell culture and transfection

Vinculin -/- MEFs (kindly provided by Dr. Ben Fabry and Dr. Wolfgang H. Goldmann [183], Friedrich-Alexander-Universitat Erlangen-Nurnberg) were maintained in high-glucose DMEM with sodium pyruvate (D6429, Sigma Aldrich, St. Louis, MO) supplemented with 10% FBS (HyClone, Logan, UT), 1% v/v non-essential amino acids (Invitrogen, Carlsbad, CA), and 1% v/v antibiotic-antimycotic solution (Sigma Aldrich). HEK293 cells were maintained in high-glucose DMEM (D5796, Sigma Aldrich) supplemented with 10% FBS (HyClone) and 1% v/v antibiotic-antimycotic solution (Sigma Aldrich). Cells were grown at 37 °C in a humidified 5% CO_2 atmosphere. Cells were transfected at 50-75% confluence in 6-well tissue culture plates using Lipofectamine 2000 (Invitrogen) following the manufacturer's instructions.

3.2.2 Generation of TSMods and vinculin tension sensor constructs

Constructs were created from the previously generated pcDNA3.1 mTFP1 [131, 197] and pcDNA3.1 Venus (A206K) [131, 198] as well as pcDNA3.1 Clover (Addgene 40259) and pcDNA3.1 mRuby2 (Addgene 40260) [199]. Minimal versions of single FPs were generated via Polymerase Chain Reaction (PCR) and inserted into pcDNA3.1 via EcoRI/NotI digestion and subsequent ligation (T4 DNA Ligase, NEB, Ipswich, MA). Specifically, creation of minimal FPs involved deletion of the 11 C-terminal residues in mTFP1 and Clover, and the first and second N-terminal residues in Venus and mRuby2 after the start codon. Oligonucleotide primers used to generate full-length and minimal versions of mTFP1, Venus A206K, Clover, and mRuby2 are detailed in Table 3.1.

The FP component fragments of the mTFP1-Venus and Clover-mRuby2 TSMods were derived from pcDNA3.1 TS module [131] and pcDNA3.1-Clover-mRuby2 (Addgene 49089) or the minimal FP variants described above. The extensible $(GPGGA)_n$ and $(GGSGGS)_n$ extensible domains were derived from pcDNA3.1 TS module [131] and pET29CLY9 (Addgene 21769) [200], respectively. Gibson assembly was used to construct TSMods containing a given FRET pair and extensible domain from three fragments: (1) vector backbone and donor FP (complementary regions: 5′-ampicillin gene, 3′-donor FP), (2) extensible domain region (complementary regions: 5'-donor FP, 3′-acceptor FP), and (3) vector backbone and acceptor FP (complementary regions: 5′-acceptor FP, 3′-ampicillin gene). Primers used to generate the extensible domain region in this reaction scheme were designed to nonspecifically target the repetitive extensible domain

sequence, thereby generating extensible domains of various lengths. Following assembly and transformation into DH5α competent cells, single colonies were assayed for extensible domain length by DNA sequencing. Oligonucleotide primers used to generate TSMods are detailed in Table 3.1.

All variants of the vinculin tension sensor were derived from pcDNA3.1 Vinculin TS [131]. In a cloning strategy analogous to that described above for the TSMods, Gibson assembly techniques were used to assemble vinculin tension sensors containing various minimal Clover-mRuby2 TSMods based on three fragments: (1) vector backbone and vinculin head domain residues 1 - 883 (complementary regions: 5′-ampicillin gene, 3′-Clover), (2) TSMod with desired $(GGSGGS)_n$ extensible domain (complementary regions: 5′-Clover, 3′-mRuby2), and (3) vector backbone and vinculin tail domain residues 884 - 1066 (complementary regions: 5′-mRuby2, 3′-ampicillin gene). Again, the assembled DNA fragments were transformed into DH5α competent cells and extensible domain length was verified for single colonies by DNA sequencing. Oligonucleotide primers used to generate vinculin tension sensors are detailed in Table 3.1.

Table 3.1: Primers used in Chapter 3

Fluorescent Protein Truncation	Sequence (5' to 3')
trunc-mClover-EcoRI-F*	TAGTGAATTCGCCATGGTGAGCAAGGGCG
trunc-mClover-NotI-R	TGCGGCCGCTTAGGCGGCGGTCACGAAC
trunc-mRuby2-EcoRI-F	TAGCGAATTCGCCATGAAGGGCGAAGAGCTGATCAA
trunc-mRuby2-NotI-R	TGCGGCCGCTTACTTGTACAGCTCGTCCATC
trunc-Teal-NotI-R	TGCGGCCGCTTAGCGGGCCACGGCG
trunc-Venus-EcoRI-F	TAGCGAATTCGCCATGAAGGGCGAGGAGCTGTTC
trunc-Venus-NotI-R	TGCGGCCGCTTACTTGTACAGCTCGTCCATGC

Gibson Assembly of Tension Sensor Modules	Sequence (5' to 3')
pcDNA3.1-CRMod-GPGGAn	
Gibson-Clover-mRuby-Long-F	GTGCAGGTCCAGGTGGTGCTATGGTGTCTAAGGGCGAAGAGCTGATCAAGGAAAATATGC
Gibson-Clover-mRuby-Long-R	GGCCCTGCACCACCTGGCCCCTTGTACAGCTCGTCCATGCCATGTGTAATCCCG
Gibson-TSmod-Forward	GCATGGACGAGCTGTACAAGGGGCCAGGTGGT
Gibson-TSmod-Reverse	TCTTCGCCCTTAGACACCATAGCACCACCTGGACC
pcDNA3.1-tCRMod-GPGGAn	
mR-Cl-TS-Ins-F	AGTTCGTGACCGCCGCCGGGGGGCCAGGTGGTGCAGGG
mR-Cl-TS-Ins-R	TTGATCAGCTCTTCGCCCTTAGCACCACCTGGAC
mR-Cl-TS-Vec-F	GTGCAGGTCCAGGTGGTGCTAAGGGCGAAGAGCTGATCAAG
mR-Cl-TS-Vec-R	GGCCCTGCACCACCTGGCCCCCCGGCGGCGGT
pcDNA3.1-dBamHI-tCRMod-GGSGGSn	
mR-Cl-GGS-Ins-F	AGTTCGTGACCGCCGCCGGGGGTGGATCCGGTGGATCAG
mR-Cl-GGS-Ins-R	TTGATCAGCTCTTCGCCCTTGCTACCTCCGGATCCACCACT
mR-Cl-GGS-Vec-F	GTGGTGGATCCGGAGGTAGCAAGGGCGAAGAGCTGATCAAGG
mR-Cl-GGS-Vec-R	CCTGATCCACCGGATCCACCCCCGGCGGCGGTC
pcDNA3.1-dBamHI-tTVMod-GGSGGSn	
T-V-GGS-Ins-F	ACGAGAGCGCCGTGGCCCGCGGTGGATCCGGTGGAT
T-V-GGS-Ins-R	GTGAACAGCTCCTCGCCCTTGCTACCTCCGGATCCACCA
T-V-GGS-Vec-F	GTGGTGGATCCGGAGGTAGCAAGGGCGAGGAGCT
T-V-GGS-Vec-R	CCTGATCCACCGGATCCACCGCGGGCCACGGC

Gibson Assembly of Clover-mRuby2 Vinculin Tension Sensors	Sequence (5' to 3')
VinCR-Ins-F	GGATGGACGAGCTGTACAAGGCG
VinCR-Ins-R	TCCTCGCCCTTGCTCACCATCATCTCGACCTC
VinCR-Vect-F	AAAAAGATGAGGTCGAGATGATGGTGAGCAAGGGCGAG
VinCR-Vect-R	TCTGGGAACTCCGCGGCCGCCTTGTACAGCTCGTCCATCCC

Sequencing Primers	Sequence (5' to 3')
TSMod-seqF	GACCATCTACAGGGCCAAGA
Clover-seqF	AGGACGACGGTACCTACA

* Also used as Teal F primer

3.2.3 FRET imaging

For cell imaging, glass coverslips (#1.5, Bioptechs, Butler, PA) placed in reusable dishes (Bioptechs) were coated overnight at 4 °C with 10 μg/mL fibronectin (Fisher Scientific, Pittsburgh, PA). Transfected vinculin -/- MEFs expressing a given tension sensor construct were then trypsinized, transferred to the prepared glass-bottom dishes at a density 50,000 cells per dish, and allowed to spread to 4 h. For fixed experiments, samples were then rinsed quickly with PBS, and fixed for 10 min with 3.7% methanol-free paraformaldehyde (Electron Microscopy Sciences, Hatfield, PA). For live

experiments, growth media was exchanged, at least 1 h before imaging, for imaging media - Medium 199 (Life Technologies, 11043) supplemented with 10% FBS (HyClone), 1% v/v non-essential amino acids (Invitrogen), and 1% v/v antibiotic-antimytotic solution (Sigma Aldrich). Live cell imaging was performed for up to 30 min at 37 °C (Stable Z system, Bioptechs).

All imaging was performed on an Olympus IX83 inverted epifluorescent microscope (Olympus, Center Valley, PA) equipped with a LambdaLS 300W ozone-free xenon bulb (Sutter Instruments, Novato, CA), a sCMOS ORCA-Flash4.0 V2 camera (Hamamatsu, Japan), motorized filter wheels (Sutter Instruments 10-3), and automated stage (H117EIX3, Prior Scientific, Rockland, MA). Image acquisition was controlled by MetaMorph Advanced software (Olympus). Samples were imaged at 60X magnification (Olympus, UPlanSApo 60X/NA1.35 objective, 108nm/pix), using a three-image sensitized emission acquisition sequence [201]. The filter set for FRET imaging of mTFP1-Venus sensors includes mTFP1 excitation (ET450/30x, Chroma, Bellows Falls, VT), mTFP1 emission (Chroma, ET485/20m), Venus excitation (Chroma, ET514/10x), and Venus emission (FF01-571/72, Semrock, Rochester, NY) filters, and a dichroic mirror (Chroma T450/514rpc). Images of mTFP1-Venus sensors were acquired in, sequentially, the acceptor channel (Venus excitation, Venus emission, 1000 ms exposure), FRET channel (mTFP1 excitation, Venus emission, 1500 ms exposure), and donor channel (mTFP1 excitation, mTFP1 emission, 1500 ms exposure). For Clover-mRuby2 sensors, we utilized the FITC and TRITC filters from the DA/FI/TR/Cy5-4X4 M-C Brightline Sedat

filter set (Semrock), which provided efficient Clover excitation (FF02-485/20), Clover emission (FF01-525/30), mRuby2 excitation (FF01-560/25), and mRuby2 emission (FF01-607/36) filters, and appropriate dichroic mirror (FF410/504/582/669-Di01) for FRET imaging. Images of Clover-mRuby2 sensors were acquired in, sequentially, the acceptor channel (mRuby2 excitation, mRuby2 emission, 1500 ms exposure), FRET channel (Clover excitation, mRuby2 emission, 1500 ms exposure), and donor channel (Clover excitation, Clover emission, 1500 ms exposure).

3.2.4 Quantitative FRET efficiency measurements from 3-cube FRET imaging

FRET was detected through measurement of sensitized emission [201] and subsequent calculations were performed on a pixel-by-pixel basis using custom written code in MATLAB (Mathworks, Natick, MA) [202]. Prior to FRET calculations, all images were first corrected for uneven illumination, registered, and background-subtracted. Spectral bleed-through coefficients were determined through FRET-imaging of donor-only and acceptor-only samples (i.e. cells expressing a single donor or acceptor FP). Donor bleed-through coefficients (dbt) were calculated for mTFP1 and Clover as:

$$dbt = \langle \frac{I_f}{I_d} \rangle$$

where I_f is the intensity in the FRET-channel, I_d is the intensity in the donor-channel, and data were binned by donor-channel intensity. Similarly, acceptor bleed-through coefficients (abt) were calculated for Venus and mRuby2 as:

$$abt = \langle \frac{I_f}{I_a} \rangle$$

where I_a is the intensity in the acceptor-channel, and data were binned by acceptor-channel intensity. To correct for spectral bleed-through in experimental data, corrected FRET images (F_C) were generated following the equation:

$$F_c = I_f - dbt * I_d - abt * I_a$$

After bleed-through correction, FRET efficiency was calculated following the equation:

$$E = \frac{I_d + \frac{F_c}{G}}{I_a}$$

where G is a proportionality constant that describes the increase in acceptor intensity (due to sensitized emission) relative to the decrease in donor intensity (due to quenching) [201]. This constant depends on the specific FRET pair used, imaging system, and image acquisition settings, and was calculated for both mTFP1-Venus and Clover-mRuby2 biosensors through imaging donor-acceptor fusion constructs of differing but constant FRET efficiencies. See Table 3.2 for bleed-through and G coefficients.

Wherever possible, image analysis was standardized using custom-written Matlab software. Analysis parameters (Table 3.2) and thresholds for image segmentation were maintained across multiple days of experiments of the same type. For all TSMod

and VinTS constructs, only cells with an average acceptor intensity within a pre-specified range were analyzed. This range was set to [1000, 40000] for mTFP1-Venus-based sensors or [600, 24000] for Clover-mRuby2-based sensors, resulting in exclusion of <10% of cells. Finally, for VinTS constructs, cells that were not fully spread were also excluded from analysis.

Table 3.2: Spectral bleed-through coefficients and G factors. Parameters used in the FRET image analysis of mTFP1-Venus and Clover-mRuby2 based tension sensor FRET efficiency calculations.

FRET-pair	Imaging Environment	abt	dbt	G
mTFP1-Venus	Live	0.27	1.02	2.96
mTFP1-Venus	Fixed	0.26	0.97	2.65
Clover-mRuby2	Live	0.09	0.27	0.24
Clover-mRuby2	Fixed	0.08	0.26	0.24

3.2.5 Segmentation and analysis of VinTS in FAs

Post-processing of FRET images to segment and quantify the characteristics of individual FAs was performed using custom-written code in MATLAB (Mathworks). Briefly, FAs were identified and segmented on the acceptor channel using the water algorithm [203]. The resultant mask was applied across all images for ease of data visualization and quantification. For each identified FA, parameters describing its brightness in the acceptor channel, morphology, and molecular loading (FRET) were determined. To identify single cells, closed boundaries were drawn by the user based on the unmasked acceptor-channel image. From these cell outlines, parameters describing cell morphology and FA subcellular location were also determined.

Line scans of single FAs were performed using ImageJ software (US National Institutes of Health, Bethesda, MD; http://imagej.nih.gov/ij/). Specifically, the line tool

was used to visualize the acceptor channel intensity profile across single, large FAs in the cell periphery. The coordinates of these lines, drawn axially starting from the tip of FAs distal to the cell body, were then transferred to masked FRET efficiency images. Acceptor intensity and FRET efficiency profiles from single FAs were saved as text files for subsequent analysis.

3.2.6 FRET efficiency calculations from spectrofluorometry

Hypotonic lysates were prepared from HEK293 cells as previously described [204]. In addition to experimental samples, lysates from an equal number of untransfected cells were harvested and used as a reference background. Spectrofluorometric measurements were made with a Fluorolog-3 (FL3-22, HORIBA Scientific Jobin Yvon, Edison, NJ) spectrofluorometer with 1 nm step size, 0.2 s integration time, and 3 nm excitation and emission slit widths for all samples. For FRET measurements of mTFP1-Venus sensors, spectra were traced from 472 to 650 nm following donor excitation (λ_{Dex}) at 458 nm, and from 520 to 650 nm following acceptor excitation (λ_{Aex}) at 505 nm. For Clover-mRuby2 sensors, spectra were traced from 520 to 700 nm following donor excitation at 505 nm, and from 590 to 700 nm following acceptor excitation at 575 nm. The same settings were used to measure the emission spectra of full length and minimal FPs to confirm their spectral properties individually. Custom-written code in MATLAB (Mathworks) was used to calculate FRET efficiency via the $(ratio)_A$ method [205] as:

$$E = \frac{\varepsilon_A \lambda_{Aex}}{\varepsilon_D \lambda_{Dex}} \left(\frac{I_f \lambda_{Aem}}{I_a \lambda_{Aem}} - \frac{\varepsilon_A \lambda_{Dex}}{\varepsilon_A \lambda_{Aex}} \right)$$

where I_f and I_a are the intensities, at peak acceptor emission wavelength (λ_{Aem}, 530 nm for Venus, 610 nm for mRuby2), of the sample excited at donor and acceptor wavelengths, respectively. Donor and acceptor molar extinction coefficients (ε_D and ε_A, respectively) were calculated from absorbance spectra measured on the same Fluorolog-3 spectrofluorometer in absorbance mode (1 nm step size, 0.1 s integration time, 2 nm excitation and emission slit widths) using previously-measured maximal extinction coefficients: 64,000 $M^{-1}cm^{-1}$ for mTFP1 [197], 93,000 $M^{-1}cm^{-1}$ for Venus [198], 111,000 $M^{-1}cm^{-1}$ for Clover [199], and 113,000 $M^{-1}cm^{-1}$ for mRuby2 [199]. This approach was also used to confirm the absorbance spectra of the minimal FPs were unaltered as compared to the parent version.

3.2.7 Statistics, bootstrapping, and data digitization

All statistical analyses, except numerical bootstrapping, were performed using JMP Pro 12 software (SAS, Cary, NC). ANOVAs were used to determine if statistically significant differences ($p < 0.05$) were present between groups. If statistical differences were detected, Tukey's HSD post-hoc testing was used to perform multiple comparisons and assess statistical differences between individual groups (see Table 3.3 for exact p-values and multiple comparisons test details). Box-and-whisker diagrams (**Figure 3.1F**, **Figure 3.3C**) display the following elements: center line, median; box limits, upper and

lower quartiles; whiskers, 1.5x interquartile range; red filled circle, mean; open circles, outliers.

Table 3.3: Statistical test details including exact p-values for ANOVAs and post-hoc tests.

Figure panel	Metric	Statistical Test	Comparison Group 1	Comparison Group 2	p-value
Figure 3.16D	Brightness	ANOVA	Multiple Comparisons		0.821
Figure 3.16H	FRET Efficiency	ANOVA	Multiple Comparisons		2.48E-10
Figure 3.16H	FRET Efficiency	Tukey's HSD	$(GGSGGS)_5$	$(GGSGGS)_7$	0.0003
Figure 3.16H	FRET Efficiency	Tukey's HSD	$(GGSGGS)_5$	$(GGSGGS)_9$	9.57E-10
Figure 3.16H	FRET Efficiency	Tukey's HSD	$(GGSGGS)_7$	$(GGSGGS)_9$	0.003
Figure 3.16L	Force	ANOVA	Multiple Comparisons		0.0003
Figure 3.16L	Force	Tukey's HSD	$(GGSGGS)_5$	$(GGSGGS)_7$	0.007
Figure 3.16L	Force	Tukey's HSD	$(GGSGGS)_5$	$(GGSGGS)_9$	0.0004
Figure 3.16L	Force	Tukey's HSD	$(GGSGGS)_7$	$(GGSGGS)_9$	0.623
Figure 3.16P	Extension	ANOVA	Multiple Comparisons		0.749
Figure 3.14A	FA Area	ANOVA	Multiple Comparisons		0.965
Figure 3.14B	FA Axis Ratio	ANOVA	Multiple Comparisons		0.073
Figure 3.14C	Norm Dist. From Cell Edge	ANOVA	Multiple Comparisons		0.968
Figure 3.14D	Cell Perimeter	ANOVA	Multiple Comparisons		0.862
Figure 3.14E	Cell Axis Ratio	ANOVA	Multiple Comparisons		0.282
Figure 3.14F	n FAs per Cell Area	ANOVA	Multiple Comparisons		0.484
Figure 3.14G	Brightness	ANOVA	Multiple Comparisons		0.821

Numerical bootstrapping using the built-in Matlab (Mathworks) function bootstrp.m was used to calculate 95% confidence intervals for measurements of persistence length (**L**$_P$). Specifically, for each of 200 bootstrapped samples, drawn with replacement from the pertinent dataset, the **L**$_P$ that best reflected that sample was calculated by chi-squared error minimization. The mean and 95% confidence intervals of the resultant 200 values of **L**$_P$ are reported in Table 3.4. Fluorescence-force spectroscopy data [194] was digitized using the digitize2.m function in Matlab (Mathworks). To recapitulate the uncertainty in these published unloaded FRET and FRET-force datasets, random sets of 100 data points obeying a gaussian distribution with the reported mean and standard deviation were used.

For FRET efficiency measurements, numerical bootstrapping of pilot data was used to determine the sample size required to estimate FRET efficiency to within 1% of

the true population mean. This was determined to be 10-20 cells from 3 independent experiments for in cellulo measurements, or 5 independent samples for in vitro spectral FRET characterization. For fluorescent protein absorbance/emission spectra characterization, sample size was not pre-determined. Rather, the reproduction of data from independent experiments was deemed sufficient to draw conclusions about changes in the fluorescent protein spectral properties.

3.3 Results

3.3.1 Creation of TSMods based on synthetic unstructured polypeptides

TSMods for intracellular use consist of two fluorescent proteins (FPs) connected by an extensible domain (Figure 3.1A). To enable the creation of tension sensors with diverse mechanical sensitivities, we constructed a variety of TSMods using FPs with distinct photophysical properties connected by unstructured polypeptides of various lengths and mechanical properties, as each of these characteristics critically determine the behavior of these sensors (Figure 3.1B-D). We based our designs on the first calibrated TSMod [131], which is comprised of the mTFP1-Venus FRET pair connected by a flagelliform silk-based polypeptide with the repeated sequence $(GPGGA)_8$ and has been used in a variety of tension sensors [155, 190].

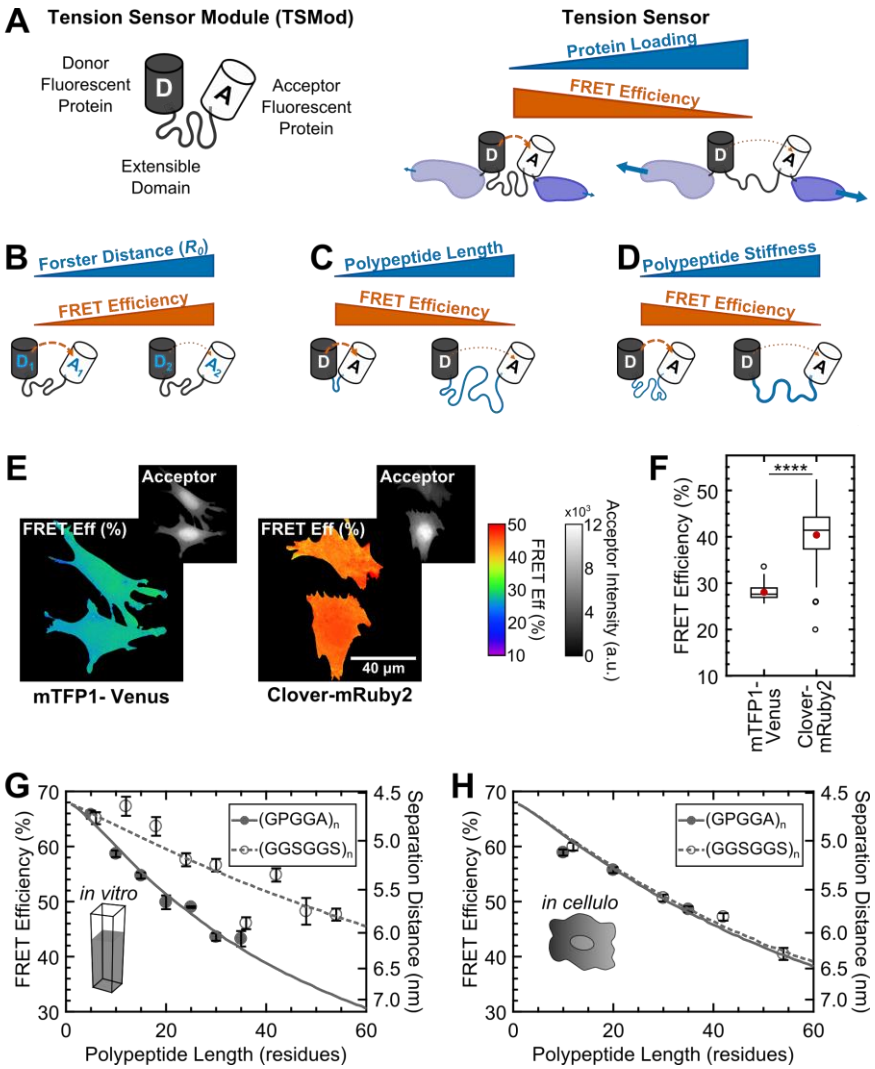

Figure 3.1: Design and characterization of tunable FRET-based molecular tension sensors. (A) Schematic depiction of a generic TSMod and inverse relationship between FRET and force for molecular tension sensors under tensile loading. (B-D) TSMod function depends on the Förster radius of the chosen FRET pair (B) as well as the length (C) and stiffness (D) of the extensible polypeptide domain. (E) Representative images of soluble mTFP1-Venus and Clover-mRuby2 TSMods expressed in Vin-/- MEFs. (F) Quantification of unloaded FRET efficiency for mTFP1-Venus and Clover-mRuby2 TSMods; (n = 53 and 92 cells, respectively); red filled circle denotes sample mean; **** $p < 0.0001$, Student's t-test, two-tailed, assuming unequal variances. (G) Quantification of FRET-polypeptide length relationship for minimal Clover-mRuby2 TSMods in vitro; each point represents data from at least 5 independent experiments; lines represent model fits where LP is the only unconstrained parameter. (H) Quantification of FRET-polypeptide length relationship for minimal Clover-mRuby2 based TSMods in cellulo; each point represents at least n = 48 cells from three independent experiments; lines represent model fits where persistence length (L_P) is the only unconstrained parameter. All error bars, s.e.m.

First, we evaluated the role of the FPs in TSMod function. Reasoning that increases in the unloaded FRET efficiency could potentially increase the dynamic range of the sensor as well as alleviate technical issues with measuring small FRET signals, we sought to increase the FRET efficiency in this state (Figure 3.1B). To do so, we replaced mTFP1-Venus with the green-red FRET pair Clover-mRuby2 [199], which exhibits stronger FRET at a given separation distance (Förster radius (R_0) of 5.7 and 6.3 nm, respectively). This simple substitution yielded a 12% higher baseline (unloaded) FRET efficiency that was observed in fixed (Figure 3.1E, F) and live cells (Figure 3.2), as well as cell lysates (Figure 3.3).

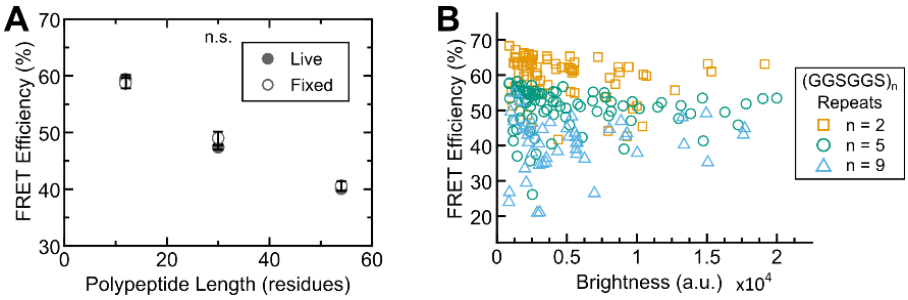

Figure 3.2: FRET efficiency measurements are insensitive to fixation and sensor intensity. (A) Quantification of FRET-polypeptide length relationship for "minimal" Clover-mRuby2 based TSMods in cellulo either live or fixed; each point represents at least n = 9 cells per experiment from three independent experiments; analysis of covariance (ANCOVA) was used to provide a model-independent assessment of statistical differences; ANCOVA interaction term $p > 0.05$ indicates that the relationship between FRET efficiency and polypeptide length is not significantly different (n.s.) between live and fixed conditions; error bars, s.e.m. (B) FRET efficiency measurements as a function of mean acceptor intensity (brightness) for fixed cells expressing TSMods consisting of the "minimal" Clover-mRuby2 FRET pair and (GGSGGS)2,5,9 extensible domains (R2 = 0.06, 0.01, 0.03 and n = 74, 86, 48 cells, respectively; data pooled from three independent experiments).

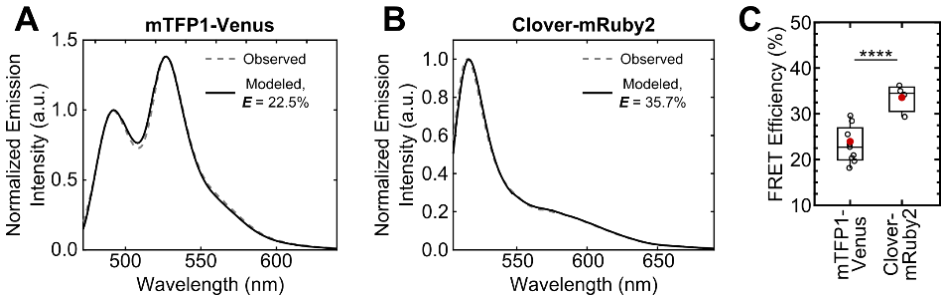

Figure 3.3: Increase in unloaded FRET efficiency with Clover-mRuby2 sensors in vitro. (A, B) Representative images of quantitative spectral analysis of mTFP1-Venus (A) and Clover-mRuby2 (B) TSMod fluorescence in cell lysates using the (ratio)A method [205]. C) Quantification of unloaded FRET efficiency for mTFP1-Venus and Clover-mRuby2 TSMods with (GPGGA)8 extensible domain; (n = 9 and 4 independent experiments, respectively); red filled circle denotes sample mean; **** $p < 0.0001$, Student's t-test, two-tailed, assuming unequal variances.

In addition to their photophysical properties, we considered the effect of the physical structure of the FPs on their performance in TSMods. Although commonly identified by a characteristic beta-barrel structure, FPs also contain short unstructured regions at their termini that likely contribute to the effective mechanical properties of the extensible domains used in TSMods [206]. Previous work, and our data (Figure 3.4), have shown that "minimal" Clover (residues 1 – 227) and mRuby2 (residues 3 – 236) exhibit absorbance and emission spectra indistinguishable from their full-length counterparts [139, 206-209]. Therefore, to mitigate concerns about FPs affecting the mechanical properties of the extensible domains and further increase the unloaded FRET efficiency, minimal versions of Clover and mRuby2 were used in the construction of all TSMods.

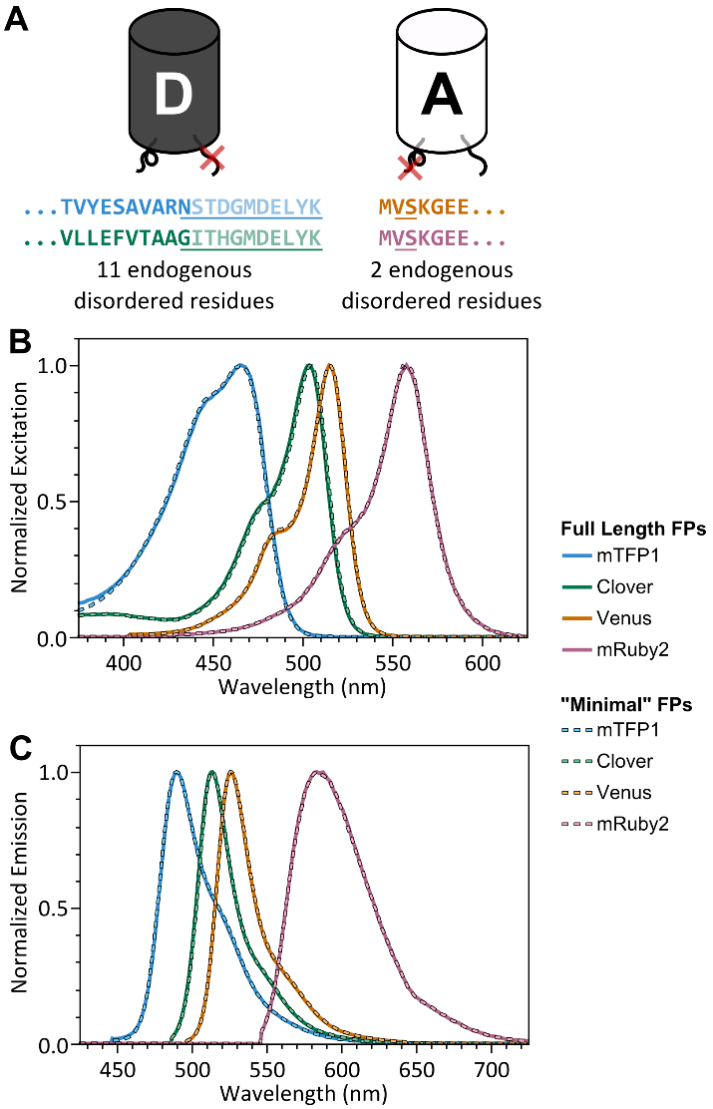

Figure 3.4: "Minimal" FPs exhibit spectral properties indistinguishable from full-length parent FPs. (A) Schematic of donor and acceptor FPs highlighting 11 C-terminal residues (donor FP) and 2 N-terminal residues (acceptor FP), which do not contribute to beta barrel structure, but are highly conserved between various FPs; residues not appearing in crystal structures are faded (PDB 2HQK and 1MYW for donor and acceptor FPs, respectively); residues that were removed are underlined. (B, C) Normalized excitation (B) and emission (C) spectra for full length and "minimal" versions of mTFP1, Venus, Clover, and mRuby2.

Recent evidence suggests that both the mechanical properties [192, 195] and the length [194] of the extensible domain provide viable means by which to tune the mechanical sensitivity of TSMods (Figure 3.1C, D). Towards this end, we created a variety of TSMods containing extensible domains comprised of either the flagelliform-based $(GPGGA)_n$, which is thought to be relatively stiff [210], or the synthetic $(GGSGGS)_n$ which has been characterized as an unstructured polypeptide and has previously been employed as a tunable linker in biochemical sensors [200]. Analysis of TSMods in cell lysates showed that those with $(GGSGGS)_n$ extensible domains exhibit higher FRET efficiencies than those with $(GPGGA)_n$ extensible domains of the same length (Figure 3.1G), suggesting that $(GPGGA)_n$-based polypeptides are indeed stiffer, and thus force the FPs apart more readily, than $(GGSGGS)_n$-based polypeptides. However, when $(GPGGA)_n$ and $(GGSGGS)_n$ TSMods were evaluated in cellulo, the FRET efficiency versus length relationships were indistinguishable, suggesting the polypeptides are exhibiting identical mechanical properties (Figure 3.1H). Together, these data demonstrate that factors dictating sensor functionality in the absence of applied load can be environmentally sensitive, and that the behavior of TSMods observed in vitro may not be reflective of their behavior in cellulo. As such, these results raise concerns about the applicability of calibrations of FRET-based tension sensors performed in vitro to sensors that are used in intracellular environments.

3.3.2 A quantitative model describing the mechanical sensitivity of TSMods

As an alternative to TSMod calibration through in vitro approaches, we pursued a modeling-based approach for describing the mechanical sensitivities of TSMods. Given that FPs linked by $(GGSGGS)_n$ polypeptides are well-described by established models of polymer physics in unloaded conditions [200], we developed an analogous model to predict TSMod behavior under load. Briefly, the proposed calibration model incorporates three main aspects of TSMods: (1) the photophysical properties of the FRET pair (Förster radius, $\mathbf{R_0}$), (2) the radii of the FPs ($\mathbf{R_{FP}}$), and (3) the mechanical response of the extensible domain, which is well-described as a semi-flexible polymer by a persistence length ($\mathbf{L_P}$) and a contour length ($\mathbf{L_C}$) in the framework of the worm-like chain model [196]. This modeling-based approach enables the prediction of the in cellulo mechanical response of FRET-based tension sensors by leveraging separate measurements of the in cellulo $\mathbf{L_P}$ of the unstructured polypeptide used as the extensible domain. In the following sections we describe, in detail, the development, validation, and implementation of this computational model describing the mechanical sensitivity of TSMods.

3.3.2.1 Model Overview

Estimates of TSMod mechanical sensitivity relate measured FRET efficiencies to applied forces. However, force and FRET are neither linearly nor simply related, as the relationship will depend on the mechanical properties of the extensible domain as well

as the manner in which the extensible domain is connected to the fluorescent moiety. When considering TSMods with unstructured polypeptide extensible domains, there are two key distance metrics that must be considered. First, the end-to-end distance of the polypeptide (r_e) can be directly related to force via various mechanical models of polymer mechanics (see Chapter 3.3.2.2, Figure 3.5A). Second, the chromophore separation distance (r_c) is directly related to FRET via established distance-FRET relationships including the Förster equation (see Chapter 3.3.2.4, Figure 3.5C). The relationship between r_e and r_c therefore is of critical importance and requires knowledge of the radii of the FPs (see Chapter 3.3.2.3, Figure 3.5B). Details of how the calculations were performed are provided in Chapter 3.3.2.5.

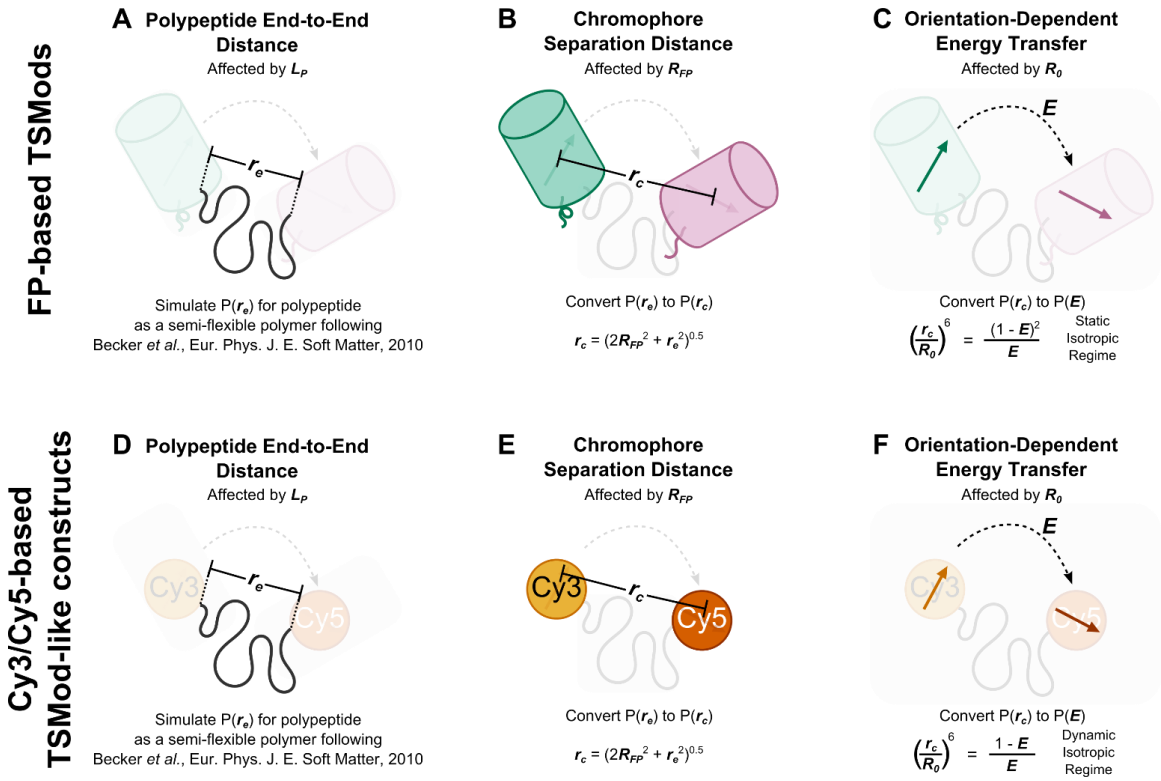

Figure 3.5: Schematic depiction of biophysical model describing the mechanical sensitivity of TSMods. (A-C) Mechanical sensitivity of FRET-based TSMods depends on the mechanical properties and length of the extensible domain (A), the physical separation of the chromophores within the FPs (B), and the relative orientation and timescale of rotation of the FPs (C). (D-F) Similarly, the mechanical sensitivity of FRET-based TSMod-like constructs which utilize Cy3 and Cy5 as the fluorescent moiety depends on the mechanical properties and the length of the extensible domain (D), the physical separation of the organic dyes (E), and the relative orientation and timescale of rotation of the dyes (F). Note when modeling large FP-based TSMods, the static isotropic regime of energy transfer is valid, while FRET between organic dyes is more appropriately described by the dynamic isotropic assumption of the classical Förster equation [211].

3.3.2.2 Extensible domain mechanics are well-described by the worm-like chain model

To describe the mechanics of the unstructured polypeptides that serve as the extensible elements of the TSMods, we employ the worm-like chain (WLC) model. This model, widely used in the study of the mechanics of biopolymers, captures the mechanical characteristics of a polymer in two key length scales, the persistence length (L_P) and the contour length (L_C). The persistence length describes the stiffness of the polymer, and is defined as the length over which the tangent direction of the polymer remains correlated [212]. The contour length describes the fully extended length of the polymer, and is defined by the product of the monomer size (b0 = 0.38 nm for amino acid chains [200]) and the number of monomers in the chain (N). Most often, the WLC model is presented as an approximation of the predicted force-extension curve, relating the average extension of the polymer to an applied force [212]:

$$F_z = \frac{k_b T}{L_P}\left(\frac{1}{4}\left(1 - \frac{\langle r_z \rangle}{L_C}\right)^{-2} - \frac{1}{4} + \frac{\langle r_z \rangle}{L_C}\right) \tag{1}$$

where F_z is the force on the polymer chain, $\langle r_z \rangle$ is the average chain extension, k_b is the Boltzmann constant, and T is temperature. A more accurate force-extension relation was developed by [213] by a simple 7th order polynomial correction scheme:

$$F_z = \frac{k_b T}{L_P}\left(\frac{1}{4}\left(1 - \frac{\langle r_z \rangle}{L_C}\right)^{-2} - \frac{1}{4} + \frac{\langle r_z \rangle}{L_C} + \sum_{i=2}^{i \leq 7} \alpha_i \left(\frac{\langle r_z \rangle}{L_C}\right)^{i}\right) \tag{2}$$

where $\alpha_2 = -0.5164228$, $\alpha_3 = -2.737418$, $\alpha_4 = 16.07497$, $\alpha_5 = -38.87607$, $\alpha_6 = 39.49944$, and $\alpha_7 = -14.17718$.

However, despite the widespread and successful use of these approximations of the force-extension curve of a WLC in the quantification of biopolymer mechanics (see Table 3.5), these relationships are not directly compatible with most FRET-based measurements for several reasons. The issue most pertinent to this work is that Eq. 1 and 2 relate force to the average extension ($\langle r_z \rangle$) of the polypeptide chain, which is zero in the absence of force. However, the non-zero polypeptide end-to-end distance (r_e), which describes the finite rest length of the extensible domain, is more directly related to the chromophore separation distance (r_c), which is the key distance determining FRET efficiency (E). Additionally, the nonlinear relationships between these quantities (r_e, r_c, and E) prevent the use of simple heuristic correction schemes to relate various distance metrics [200].

Previous work has developed formalisms that enable these concerns to be accounted for [196, 200, 211, 214], but they have yet to be applied to the development of FRET-based TSMods. A key realization is that TSMods are molecular-scale tools and therefore will be subject to thermal fluctuations [214]. Therefore, to begin it is necessary to describe the end-to-end distance of the extensible polypeptide (r_e) as a probability

density function $P(r_e)$, which is obtained by integrating the end-to-end vector probability density function $Q(\vec{R})$ over all the angles through which the chain may rotate:

$$P(r_e) = \int_0^{\pi}\int_0^{2\pi} Q(\vec{R}) r_e^2 \sin\phi \, d\theta d\phi \tag{3}$$

yielding

$$P(r_e) = 4\pi r_e^2 Q(r_e) \tag{4}$$

Forces will alter this distribution following the widely-applied Boltzmann relation:

$$P(r_e, F_z) = P(r_e) exp\left(\frac{F_z r_e}{k_b T}\right) \tag{5}$$

where $P(r_e,F_z)$ is the probability of observing a given end-to-end distance for the polymer chain at a given force F_z. The average extension of the polypeptide chain ($\langle r_z \rangle$), which is similarly affected by forces following the Boltzmann relation, was calculated as:

$$\langle r_z \rangle = \int_{-\infty}^{\infty} r_z Q(r_z) exp\left(\frac{F_z r_e}{k_b T}\right) dr_z \tag{6}$$

However, as stated above, this parameter has limited relevance for further FRET calculations and was only calculated for comparison to classical WLC force-extension relationships (Eq. 1 & 2).

A variety of closed-form equations that describe the behavior of biopolymers exist, but are accurate only in specific force regimes and ranges of polymer mechanics

[196]. For example, the second Daniels approximation [215, 216] describes $P(r_e)$ for small extensions of soft polymers ($L_C/L_P > 5$) following:

$$P(r_e) = 4\pi r_e^2 \left(\frac{3}{4\pi L_P L_C}\right)^{3/2} exp\left(\frac{-3r_e^2}{4L_P L_C}\right)\left(1 - \frac{5L_P}{4L_C} + \frac{2r_e^2}{L_C^2} - \frac{33r_e^4}{80L_P L_C^3} - \frac{79L_P^2}{160L_C^2} - \frac{329r_e^2 L_P}{120L_C^3} + \frac{6799r_e^4}{1600L_C^4} - \frac{3441r_e^6}{2800L_P L_C^5} + \frac{1089r_e^8}{12800L_P^2 L_C^6}\right) \quad (7)$$

In other work Wilhelm & Frey develop an approximation that describes the behavior of short chain or stiff ($L_C/L_P < 2$) polymers [217]. Specifically, Wilhelm & Frey provide two series expansions:

$$P(r_e) \propto \begin{cases} \dfrac{4\pi r_e^2 k_b T L_P}{2\pi L_C} \displaystyle\sum_{k=1}^{\infty} \pi^2 k^2 (-1)^{k+1} exp\left(-\frac{L_P}{L_C} k_b T \pi^2 k^2 \left(1 - \frac{r_e}{L_C}\right)\right) \\ \qquad where\ \dfrac{L_P}{L_C}\left(1 - \dfrac{r_e}{L_C}\right) \geq 0.2 \\ \dfrac{4\pi r_e^2 L_P}{8\pi^{3/2} L_C} \displaystyle\sum_{k=1}^{\infty} \left(\frac{L_P}{L_C}\left(1 - \frac{r_e}{L_C}\right)\right)^{-3/2} exp\left(-\frac{L_C (k-0.5)^2}{L_P\left(1 - \frac{r_e}{L_C}\right)}\right) H_2\left[\frac{k - 0.5}{\sqrt{\frac{L_P}{L_C}\left(1 - \frac{r_e}{L_C}\right)}}\right] \\ \qquad where\ \dfrac{L_P}{L_C}\left(1 - \dfrac{r_e}{L_C}\right) < 0.2 \end{cases} \quad (8)$$

where H_2 is the second Hermite polynomial $H_2 = 4x^2 - 2$. However, these approximations were later found to be valid primarily at high extension [196].

Excitingly, Becker et al. developed an explicit expression which interpolates between a number of these approximations, including but not limited to those described above, and created an ansatz that accurately describes $P(r_e)$ over a wide range of polymer mechanics $0.05 < L_C/L_P < 50$ [196], and likely to much higher values in the

absence of excluded volume effects. Normalizing the stiffness to the contour length such that $\kappa = L_C/L_P$, the final form of the interpolated probability density function $P(r_e)$ is given by:

$$P(r_e) = 4\pi r_e^2 J_{SYD}\left(\frac{1-c(r_e/L_C)^2}{1-(r_e/L_C)^2}\right)^{5/2} exp\left(\frac{\sum_{i=-1}^{0}\sum_{j=1}^{3} c_{i,j}\kappa^i\,(r_e/L_C)^{2j}}{1-(r_e/L_C)^2}\right) \times exp\left(-\frac{k\kappa ab(1+b)(r_e/L_C)^2}{1-b^2(r_e/L_C)^2}\right) I_0\left(-\frac{k\kappa a(1+b)(r_e/L_C)}{1-b^2(r_e/L_C)^2}\right) \tag{9}$$

where J_{SYD} is the Shimada-Yamakawa J-factor:

$$J_{SYD} = \begin{cases} 112.04\kappa^2 e^{0.246/\kappa - a\kappa}, & \kappa > 1/8 \\ \left(\frac{3}{4\pi\kappa}\right)^{3/2}\left(1-\frac{5\kappa}{4}\right), & \kappa \le 1/8 \end{cases} \tag{10}$$

with constants $a = 14.054$, $b = 0.473$, and coefficients $c_{i,j}$ given as:

$$\left(c_{i,j}\right)_{i,j} = \begin{bmatrix} -3/4 & 23/64 & -7/64 \\ -1/2 & 17/16 & -9/16 \end{bmatrix} \tag{11}$$

Additionally, I_0 is a modified Bessel function of the first kind and parameters c and d are defined as:

$$1 - c \cong (1 + (0.38\kappa^{-0.95})^{-5})^{-1/5} \tag{12}$$

$$1 - d \cong \begin{cases} 0, & \kappa < 1/8 \\ \dfrac{1}{0.177/(\kappa - 0.111) + 6.40(\kappa - 0.111)^{0.783}}, & \kappa \ge 1/8 \end{cases} \tag{13}$$

To describe the behavior of the unstructured polypeptides used in the assembly of TSMod constructs, values of L_C, L_P and F_z were specified, and the inverse-transform-sampling method [218] was used to generate sets of random numbers distributed

according to $P(r_e,F_z)$ as specified by combining the Becker et al. ansatz (Eq. 9) with the Boltzmann relation (Eq. 5). Note that while this describes the mechanical behavior of the unstructured polypeptide, the overall force sensitivity and FRET output from a given TSMod construct will also depend on the radii and photophysical properties of the FPs attached to this extensible domain as well (discussed further in Chapters 3.2.2.3 and 3.2.2.4).

To confirm that this formalism was both correctly implemented and suitable for the intended purposes, several calculations demonstrating the ability of our simulations to accurately reproduce previous results were completed. First, we verified the ability of the model to described the unloaded states of an unstructured polypeptide by comparing the zero-force state of the calculated $P(r_e)$ (Eq. 9) to published simulations of a discretized version of the WLC model developed by Wilhelm & Frey that is often used for stiffer polymers [217], and the second Daniels approximation for softer polymers [215, 216], observing excellent agreement in all cases (Figure 3.6A). Next, we determined the predictions of the scaling between the average end-to-end distance ($\langle r_e \rangle$) and polypeptide length (N) for the proposed model, observing the classical $\langle r_e \rangle \sim N^{0.5}$ behavior characteristic of random chains (Figure 3.6B). Finally, the model was used to generate force-extension curves (Eq. 6) for various ratios of contour length to persistence length and compared to the most accurate numerical approximation of the force-extension curve of a WLC [213] (Eq. 2). The model agrees well with the numerical approximation across all L_C/L_P ratios (Figure 3.6C). Together these data show that this approach

accurately simulates $P(r_e,F_z)$ for the expected mechanics (Table 3.5) and lengths achievable for the extensible domain of polypeptide-based TSMods.

3.3.2.3 Effects of fluorescent proteins

Next, we sought a method to account for the finite size of the FPs attached to the ends of the extensible domain. Like any FRET-based biosensor, the pertinent energy transfer distance for a TSMod is the inter-chromophore distance (r_c), not simply r_e. Since the FPs have finite size, the difference between these two quantities is not negligible and has been approximated by several methods [194, 200]. In light of the experimental complexities associated with single molecule fluorescence force spectroscopy, Brenner et al. utilized a simple approach and approximated $r_c = r_e + C$ [194]. However, it is generally recognized that FPs are free to rotate around the ends of the polypeptide in a random fashion requiring more complex relationships to relate r_c to r_e. Attempts by Evers et al. to recapitulate this behavior by simulating 66 possible orientations for each FP at a given r_e (4356 total conformations possible) and considering the average as an appropriate estimate of r_c are a reasonable means of estimating these effects [200]. However, Evers' approach does not yield a realistic limit at short polypeptide lengths. Specifically, as the polypeptide length approaches zero, this approach allows for the centers of the FPs to be closer than the sum of their individual radii (Figure 3.6D). To address this issue and approximate the effects of steric hindrance between the two FPs, we used a heuristic approach involving a quadrature sum of the key distances in this problem:

$$r_c = \sqrt{(R_{FP1} + R_{FP2})^2 + r_e^2} \tag{14}$$

where R_{FP1} and R_{FP2} are the radii of the donor and acceptor FPs, respectively. Based on crystal structures of FPs [197, 219, 220] and estimates of FP hydrodynamic radii from fluorescence correlation spectroscopy [221], we set $R_{FP1} = R_{FP2} = 2.3$ nm. For cyanine dyes, these quantities were set to $R_{FP1} = R_{FP2} = 0.95$ nm, which is mathematically equivalent to the reported hydrodynamic radii of Cy3 and Cy5, which are 0.90 nm [222] and 1.00 nm [223], respectively. This steric hindrance approximation recapitulates the behavior of Evers' spherical integration approach for longer polypeptides while also providing a realistic limit for very short polypeptides (Figure 3.6D). As the operation is always the same for a given separation distance and size of FPs, a transfer function (Eq. 14) was written to a file and treated as a lookup table for the conversion of r_e to r_c.

3.3.2.4 Accounting for rotational entropy phenomenologically

When applying load to a molecule, a portion of energy works against rotational entropy before the molecule is extended. This phenomenon is known to limit resolution in force spectroscopy measurements [32], and was therefore considered in our modeling of force sensitive biosensors. Previous descriptions of this phenomenon [194] have defined a critical force:

$$F_{critial} = \frac{k_b T}{r_{c,0}} \tag{15}$$

which is required to orient the molecule in the direction of pulling, and is set by the thermal energy of the system and the unloaded distance between the FP chromophores ($r_{c,0}$). Thus, forces below $F_{critical}$ do not entirely act to increase the separation distance between the FPs. We heuristically account for these effects using:

$$|F| = \sqrt{F_z^2 + F_{critical}^2} - F_{critical} \tag{16}$$

This results in only a fraction of the total amount of force applied to the TSMod, $|F|$, leading to extension of the TSMod through the force impinging on the extensible domain itself F_z (Figure 3.6E). This causes the emergence of a regime of relative insensitivity of the sensors at very small forces (Figure 3.6F). Notably, this simple equation recapitulates observations in single molecule force spectroscopy experiments [131, 194].

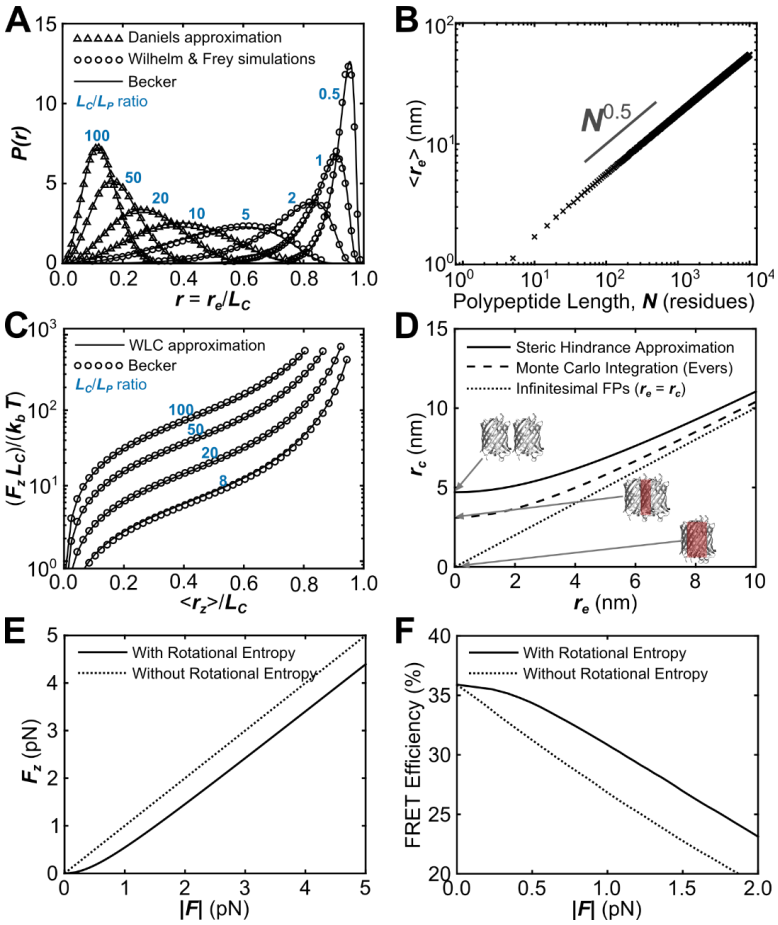

Figure 3.6: Verification of the proper implementation of a biophysical model describing the mechanical sensitivity of FRET-based TSMods. (A) Probability distributions of polypeptide end-to-end distance (r_e), normalized to contour length (L_C) such that $r = r_e/L_C$ calculated using the second Daniels approximation [215, 216], simulations from [217], and an ansatz approximation used in the proposed model based on [196] that smoothly bridges between various mechanical regimes. (B) Demonstration that the numerical ansatz predicts the standard length $\langle r_e \rangle$~N^(1/2) scaling behavior characteristic of unstructured polypeptides. (C) Under load, the average extension ($\langle r_z \rangle$) of the polypeptide extensible domain predicted by the [196] ansatz closely follows the previous prediction of the force-extension curve for a worm-like chain [213]. (D) Possible approaches to estimate the chromophore separation distance (r_c), from polypeptide end-to-end distance (r_e). Note that some approaches predict unphysical overlap of the FPs at short linker lengths, which is highlighted in red for the extreme condition of infinitesimal linker length. (E, F) The proposed model includes a dimensionless group (determined by the applied load, the rest length of the construct, and thermal energy) that heuristically accounts for the effects of rotational entropy. This results in a reduced amount of force transferred through FPs to the polypeptide at low applied force (E); this difference between the force causing extension of the polypeptide (F_z) and applied force (|F|) manifests in a plateau in the FRET-force relationship at very small loads (F).

3.3.2.5 Förster resonance energy transfer

FRET efficiency (E) was calculated for each r_c in the set using either the Förster equation:

$$r_c = R_0 * \sqrt[6]{\frac{(1-E)}{E}} \tag{17}$$

which assumes a dynamic isotropic regime for fluorescent moiety rotation ($\kappa^2 = 2/3$) and is applicable to only quickly rotating, small fluorescent moieties (e.g. cyanine dyes), or an alternative distance-FRET relationship:

$$r_c = R_0 * \sqrt[6]{\frac{(1-E)^2}{E}} \tag{18}$$

which is valid in the static isotropic regime and more accurately describes energy transfer between fluorescent moieties (e.g. FPs) which rotate on timescales longer than those associated with FRET [211, 214]. The Förster radius (R_0) appears in both relationships and is defined as the distance at which a pair of fluorescent moieties exhibit 50% FRET efficiency. The value for R_0 was set, based on previous measurements, to 5.7 nm for the mTFP1-Venus FRET pair [197], 6.3 nm for the Clover-mRuby2 FRET pair [199], and 5.4 nm for the Cy3-Cy5 FRET pair [224, 225]. As before, either transfer function was written to a file and treated as a lookup table for the conversion of any r_c to E. The mean of the resultant FRET distribution was then reported as the FRET efficiency at a given force.

3.3.2.6 Calculations

Monte Carlo simulations were used to determine the average polypeptide extension ($\langle r_z \rangle$) as well as probability distributions for the polypeptide end-to-end distance (r_e), FP chromophore separation distance (r_c), and FRET efficiency (E) at a given force on the polypeptide (F_z), persistence length (L_P), and number of residues in the polypeptide (N, used to calculate contour length, ($L_C = N * b_0$). First, a set of at least 10,000 random numbers obeying the probability distribution function $P(r_e)$ described by the Becker et al. ansatz (Eq. 9) was generated from a uniform distribution using the inverse-transform sampling method [218]. Then, the impact of force on $P(r_e)$ was accounted for following the Boltzmann relation (Eq. 5). Next, $P(r_e)$ was first converted to $P(r_c)$ using the r_e-to-r_c lookup table described by Eq. 14, and then P(E) using the r_c-to-E lookup table described by Eq. 17 for TSMod-like constructs with cyanine dyes as the fluorescent moiety or Eq. 18 for FP-based TSMods. Additionally, the force affecting the extension of the sensor ($|F|$) was determined from F_z following Eq. 16. Finally, the average of each population distribution as well as $|F|$, N, and L_P were written to a line of a TSMod calibration text file. These operations were repeated from 0 to 50 pN of force at increments of 0.1 pN to map out the FRET efficiency (E) as a function of force ($|F|$) and extension (r_z) with a given set of parameters.

3.3.2.7 Model validation in unloaded conditions

To evaluate whether the model can be used to describe the behavior of TSMods in unloaded conditions a variety of experimental results were evaluated. First, we

investigated whether the model accurately describes the relationship between FRET efficiency and polypeptide length for Clover-mRuby2 TSMods and provide reasonable estimates of L_P for $(GGSGGS)_n$ or $(GPGGA)_n$ extensible domains in both in vitro and in cellulo environments. To limit the parameter space, estimates for the other two input parameters (R_0 and R_{FP}) were obtained from previous reports of the Förster radius of Clover and mRuby2 (R_0 = 6.3 nm [199]) and the hydrodynamic radii of GFP family FPs (R_{FP} = 2.3 nm [221]). This leaves L_P as the sole adjustable parameter. Simulations were then used to predict the relationship between FRET efficiency and polypeptide length for a variety of polypeptide chains ($10 < N < 100$ residues) and persistence lengths ($0.1 < L_P < 2.0$ nm, 0.01 nm increments) and compared to in vitro FRET efficiency measurements of TSMods in cell lysates (Figure 3.1G). Model fits and bootstrapped 95% confidence intervals indicate a quantitative difference in the mechanics of $(GPGGA)_n$ (L_P = 0.74 ± 0.05 nm) and $(GGSGGS)_n$ (L_P = 0.33 ± 0.05 nm) extensible domains in vitro. Due to the presence of proline residues in the repeated structure of the $(GPGGA)_n$ extensible domain, this stiffer mechanical response is not unexpected [210]. In contrast, fits to sensitized emission-based FRET efficiency measurements of sensors expressed in cellulo revealed quantitatively indistinguishable FRET-polypeptide length relationships for TSMods containing $(GPGGA)_n$ (L_P = 0.50 ± 0.02 nm) and $(GGSGGS)_n$ (L_P = 0.48 ± 0.05 nm) extensible domains (Figure 3.1H). These values agree well with previous reports of both $(GPGGA)_n$ and $(GGSGGS)_n$ mechanics [200, 210]. In total, these results confirm that there is a quantitative difference in extensible domain mechanics between in vitro and in

cellulo environments, although less-so for $(GGSGGS)_n$-based TSMods and provide quantitative measurements of L_P that can be used to generate in cellulo TSMod calibrations.

To rule out the possibility that constraining R_{FP} and/or R_0 to their published values was skewing estimates of L_P, we examined whether improved fits to experimental data could be obtained if either R_{FP} or R_0 (in addition to L_P) were left unconstrained. Specifically, we compared simulated FRET-polypeptide length relationships for various combinations of either L_P and R_0 (at R_{FP} = 2.3 nm) or L_P and R_{FP} (at R_0 = 6.3 nm) to experimental FRET-length measurements made in vitro (Figure 3.7) or in cellulo (Figure 3.8). Simulations included L_P ranging from 0.10 to 1.00 nm, R_{FP} from 1.7 to 3.4 nm, and R_0 from 5.1 to 6.8 nm. We then evaluated the chi-squared error between model predictions and experimental data for each such combination of L_P and R_{FP} (Figure 3.7A, 3.7B, 3.8A, 3.8B) or L_P and R_0 (Figure 3.7C, 3.7D, 3.8C, 3.8D). In all cases, regardless of measurements made in vitro or in cellulo, minimal chi-squared error between model and experiment occurs at or close to the literature estimates of both R_{FP} and R_0 (highlighted with vertical green rectangles). Finally, compared to the single unconstrained parameter L_P, leaving two parameters unconstrained leads to no significant improvement in fits to the relationship between FRET efficiency and polypeptide length in unloaded conditions (Figure 3.7E, 3.8E). Thus, we conclude the use of literature-based estimates for key parameters did not bias our analysis.

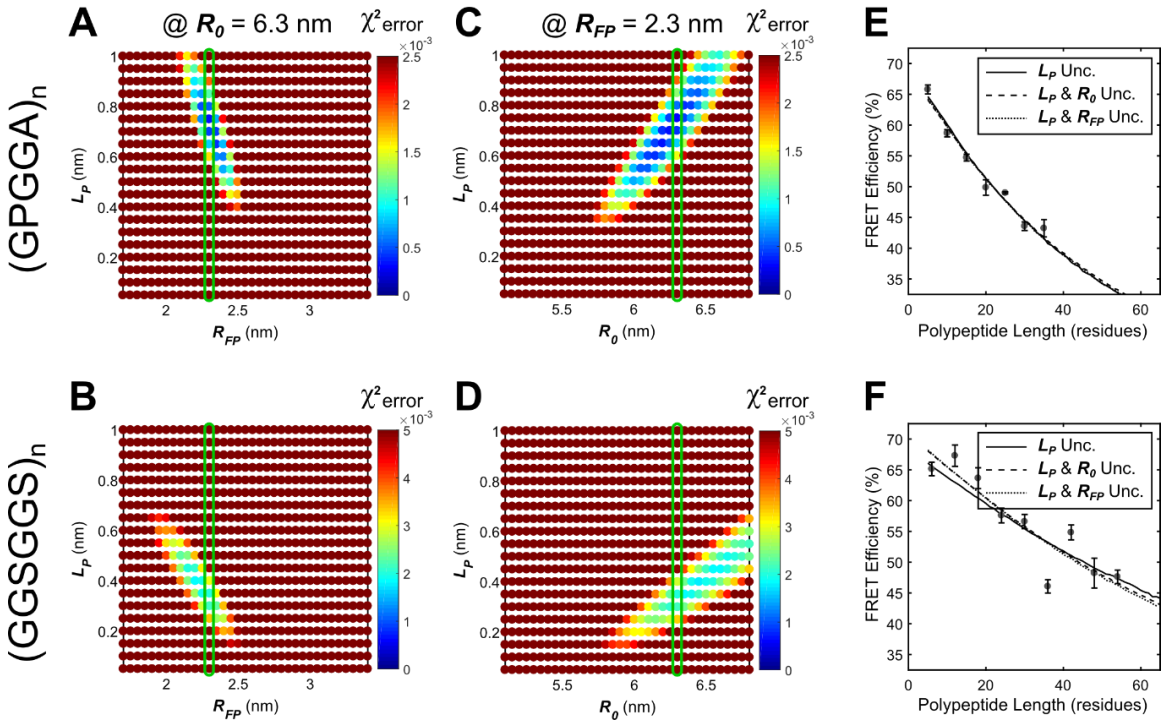

Figure 3.7: Parameter constraint has minimal effects on measurement of polypeptide persistence length (L_P) in vitro. (A, B) Heatmaps of chi-squared error of model fits to in vitro "minimal" Clover-mRuby2 based TSMod FRET-length measurements for various R_{FP} and L_P for $(GPGGA)_n$ (A) and $(GGSGGS)_n$ (B) extensible domains; literature estimate of R_{FP} used for parameter constraint highlighted with green bar; R_0 is constrained to 6.3 nm. (C, D) As in panels A and B, except various R_0 and L_P parameters were examined; green bar highlights R_0 parameter estimate; R_{FP} is constrained to 2.3 nm. (E, F) Model fits to in vitro FRET-length relationships for "minimal" Clover-mRuby2 based TSMods containing the $(GPGGA)_n$ (E) or $(GGSGGS)_n$ (F) extensible domain are equally accurate with either a single unconstrained (unc.) parameter (L_P) or two unconstrained parameters. See Table 3.4 for full list of fit parameters compared to values from the literature.

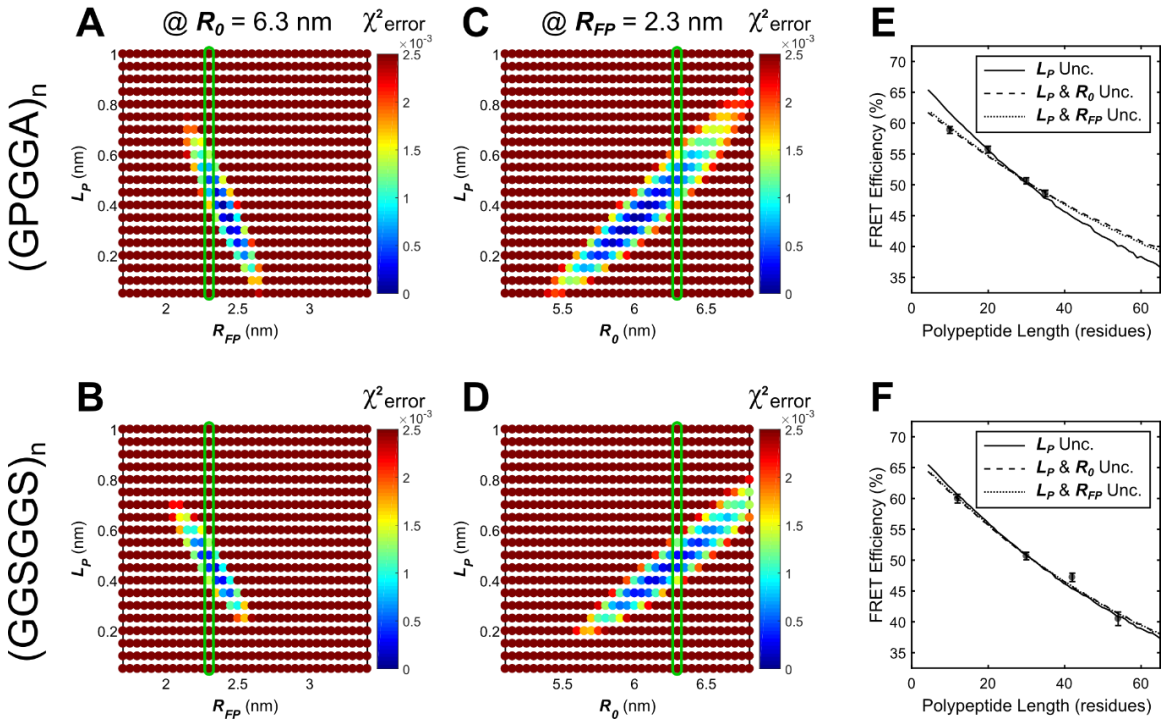

Figure 3.8: Parameter constraint has minimal effects on measurement of polypeptide persistence length (L_P) in cellulo. (A, B) Heatmaps of chi-squared error of model fits to in cellulo "minimal" Clover-mRuby2 based TSMod FRET-length measurements for various R_{FP} and L_P for $(GPGGA)_n$ (A) and $(GGSGGS)_n$ (B) extensible domains; literature estimate of R_{FP} used for parameter constraint highlighted with green bar; R_0 is constrained to 6.3 nm. (C, D) As in panels A and B, except various R_0 and L_P parameters were examined; green bar highlights R_0 parameter estimate; R_{FP} is constrained to 2.3 nm. (E, F) Model fits to in cellulo FRET-length relationships for "minimal" Clover-mRuby2 based TSMods containing the $(GPGGA)_n$ (E) or $(GGSGGS)_n$ (F) extensible domain are equally accurate with either a single unconstrained (unc.) parameter (L_P) or two unconstrained parameters. See Table 3.4 for full list of fit parameters compared to values from the literature.

3.3.2.8 Model validation in loaded conditions

To evaluate the ability of the calibration model to describe the mechanical sensitivity of TSMods subject to mechanical loads, we examined model fits to previously published fluorescence-force spectroscopy data of $(GPGGA)_n$ polypeptides labelled with Cy3 and Cy5 dyes [194]. These TSMod-like constructs differ from the FP-based TSMods

in terms of the physical size and the Förster radius of the fluorescent moiety. Therefore, we set R_{FP1} = 0.9 nm and R_{FP2} = 1.0 nm based on measurements of the hydrodynamic radii of Cy3 [222] and Cy5 [223] dyes, respectively. We also set R_0 = 5.4 nm based on the reported photophysical properties of the Cy3-Cy5 FRET pair [224, 225]. As above, the one unconstrained parameter remaining, persistence length (L_P), describes the mechanical response of the extensible domain. Simulations of Cy3-Cy5 constructs with various polypeptide lengths ($10 < N < 100$ residues) and persistence lengths ($0.1 < L_P < 2.0$ nm) were then compared to experimentally measured FRET-polypeptide length and FRET-force relationships (Figure 3.9). The simulations where $L_P \sim 1.05$ nm agree well with both the FRET-polypeptide length relationship over the range of polypeptide lengths assessed (Figure 3.9A), as well as the measured relationship between FRET efficiency and force (Figure 3.9B). For comparison, additional FRET-polypeptide length and FRET-force relationships for a range of L_P values between 1.0 nm and 1.15 nm are shown (lines in Figure 3.9A, shaded region in Figure 3.9B). Together, these data indicate that the proposed model can describe published fluorescence force measurements of TSMod-like constructs in both unloaded and loaded conditions with identical parameters.

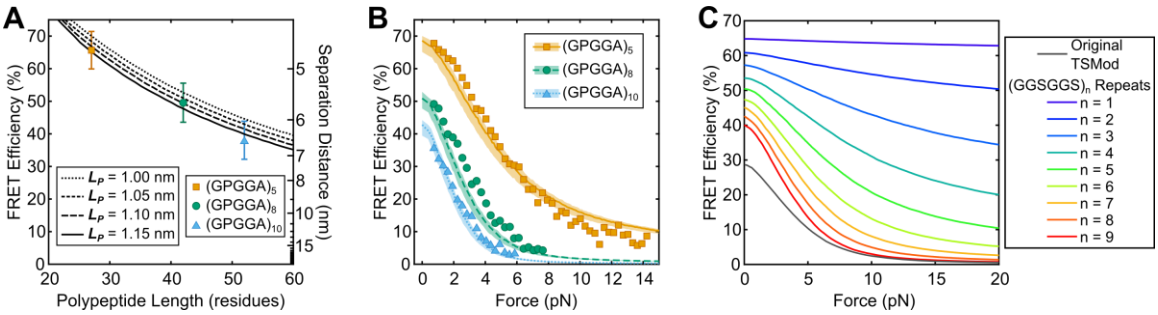

Figure 3.9: Predicting TSMod calibrations using a biophysical model. (A, B) Model descriptions, at various persistence lengths, of FRET-polypeptide length relationship (A) and FRET-force responses (B) of Cy3 and Cy5 dyes linked by SMCC linker + cysteine modified $(GPGGA)_n$ polypeptides; data was digitized based on histograms from [194]; model parameters R_0=5.4 nm, R_{FP}=0.95 nm, L_P=1.05 nm (range 1.00 to 1.15 nm); error bars, s.d. (C) Model predictions of force sensitivity of TSMods based on Clover-mRuby2 FRET pair and $(GGSGGS)_n$ extensible domains in comparison to the original TSMod [131]; model parameters R_0=6.3 nm, R_{FP}=2.3 nm, L_P=0.48 nm.

The relatively stiff mechanical response of the $(GPGGA)_n$ extensible domain (L_P ~ 1.0 nm) is somewhat unexpected given reports of other unstructured polypeptide mechanics (Table 3.5) and our own measurements of extensible domain mechanics in vitro (Figure 3.1G, Table 3.4). To rule out the possibility that constraining R_{FP} and/or R_0 to their published values was skewing estimates of L_P, we examined whether improved fits to experimental data could be obtained if either R_{FP} or R_0 (in addition to L_P) were left unconstrained. Specifically, we compared simulated FRET-polypeptide length and FRET-force relationships for various combinations of either L_P and R_0 (at $\langle R_{FP} \rangle$ = 0.95 nm) or L_P and R_{FP} (at R_0 = 5.4 nm) to experimental FRET-length and FRET-force measurements (Figure 3.10). Simulations included L_P ranging from 0.20 to 1.25 nm, R_{FP} from 0.3 to 2.0 nm, and R_0 from 4.8 to 6.5 nm. We then evaluated the chi-squared error between model predictions and experimental data for each such combination of L_P and R_{FP} (Figure 3.10A, B) or L_P and R_0 (Figure 3.10C, D). Minimal chi-squared error between

model and experiment occurs at or close to the literature estimates of both R_{FP} and R_0 (highlighted with vertical green rectangles). Finally, compared to the single unconstrained parameter L_P, leaving two parameters unconstrained leads to no significant improvement in fits to either the unloaded (Figure 3.10E) or loaded (Figure 3.10F) single molecule data. Thus, we find it unlikely that these stiff mechanics are an artifact of model parameter selection, and instead attribute the high L_P to the experimental conditions and stiff covalent attachments [194] required to connect different components in single molecule fluorescence force experiments. Specifically, the incorporation of an SMCC linker connecting the fluorescent molecules to the polypeptide chains likely contributes to the overall mechanics of the chain. The effects of this contribution may be greater for shorter polypeptide sequences, potentially explaining the increased discrepancy between the model and the data in this case. The fit parameters for the different constructs are summarized in Table 3.4.

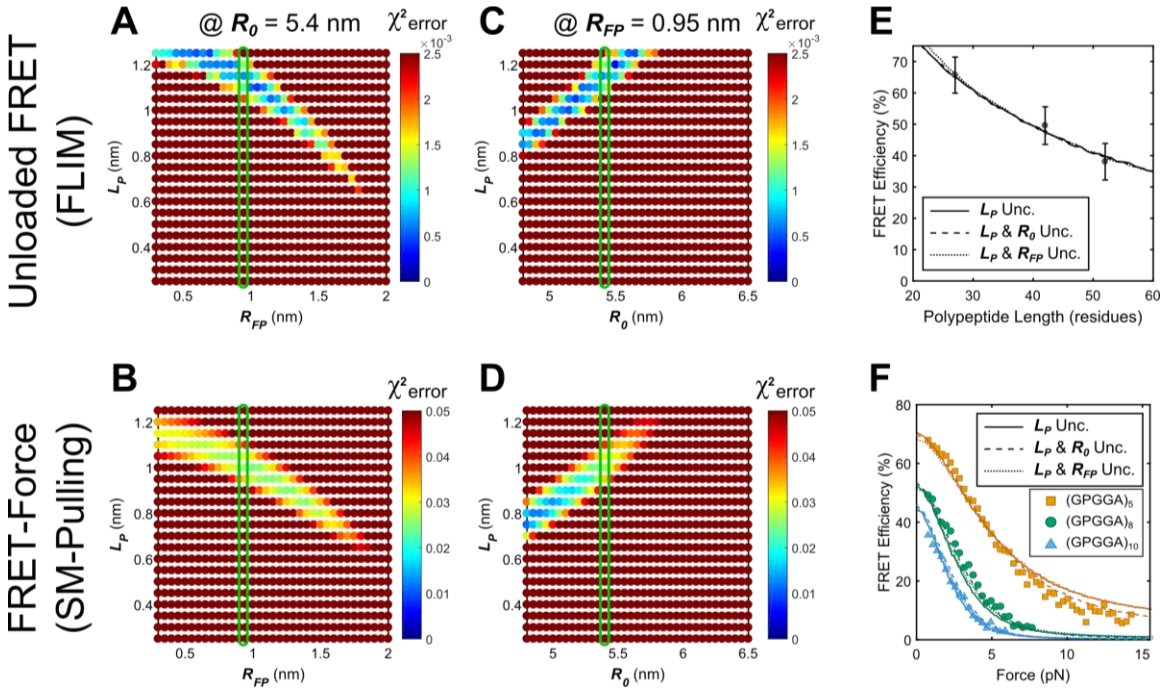

Figure 3.10: Parameter constraint has minimal effects on measurement of polypeptide persistence length (L_P) for TSMod-like constructs in unloaded or loaded conditions. (A, B) Heatmaps of chi-squared error of model fits to published fluorescence-force spectroscopy measurements of $(GPGGA)_{5,8,10}$ extensible domains flanked by Cy3 and Cy5 fluorescent dyes in unloaded (A) and loaded (B) conditions; literature estimate of R_{FP} used for parameter constraint highlighted with green bar; R_0 is constrained to 5.4 nm. (C, D) As in panels A and B, except various R_0 and L_P parameters were examined; green bar highlights R_0 parameter estimate; R_{FP} is constrained to 0.95 nm. (E, F) Model fits to published fluorescence-force spectroscopy data of TSMod-like constructs in unloaded (E) and loaded (F) conditions are equally accurate with either a single unconstrained (unc.) parameter (L_P) or two unconstrained parameters. See Table 3.4 for a full list of fit parameters compared to values from the literature.

3.3.2.9 Comparison to other descriptions of TSMod mechanical sensitivity

In validating the proposed model, we evaluated its ability to recapitulate published fluorescence force spectroscopy measurements from [194] of the mechanical response of $(GPGGA)_n$ extensible domains flanked by Cy3 and Cy5 fluorescent dyes (Chapter 3.2.2.8). Based on their modelling efforts, one of the main conclusions of Brenner et al. was that $(GPGGA)_n$ behaves as a linear nanospring, not an unstructured

polypeptide. This was primarily based on the observation of a linear relationship between average polypeptide end-to-end distance $\langle r_e \rangle$ and polypeptide length N, $\langle r_e \rangle \sim N^1$. On the contrary, for unstructured polypeptides, the predicted scaling is $\langle r_e \rangle \sim N^{0.5}$ [226] or $\langle r_e \rangle \sim N^{3/5}$ if excluded volume effects are considered [227]. Notably, the calibration model used in this work exhibits $\langle r_e \rangle \sim N^{1/2}$ scaling. Two main assumptions differentiated the Brenner calculations from the proposed calibration model. First, the calibration model considers a probability distribution of sensor conformations while Brenner et al. performed distance-FRET conversions on an average value. As previously discussed in Chapter 3.2.2.1, premature numerical averaging could lead to numerical artifacts when nonlinear transformations, as are present in distance-FRET conversions, are involved. Secondly, different assumptions were used pertaining to the connectivity of the fluorescent moieties to the polypeptide. Brenner et al. used a simple subtraction method which assumes that the fluorescent moiety is located at a constant offset from the extensible domain and $r_e = r_c - C$. This simple method has previously been reported to lead to numerical artifacts [200]. In contrast, we used a heuristic r_e to r_c conversion (details in Chapter 3.2.2.3) based on previous simulations of the various physical orientations of TSMod components [200].

To determine which of these distinct descriptions is most accurate, we investigated the effects of the assumptions in the two modelling approaches on the predictions of the scaling between $\langle r_e \rangle$ and N. We first examined what scaling is observed when the proposed calibration model is used to calculate the relationship

between ⟨r_e⟩ and N from experimental data. Starting with the published unloaded FRET efficiency measurements of Brenner et al. (Figure 3.9A), the calibration model was used to perform the abovementioned distance-FRET conversions and thus calculate ⟨r_e⟩. Plotting this data as a function of N yielded a ⟨r_e⟩~$N^{0.57}$ scaling (Figure 3.11A). While we are hesitant to over-interpret this result as it infers power-law relationships from data that varies by less than an order of magnitude, it nonetheless supports the notion that $(GPGGA)_n$ mechanics are consistent with unstructured polypeptides.

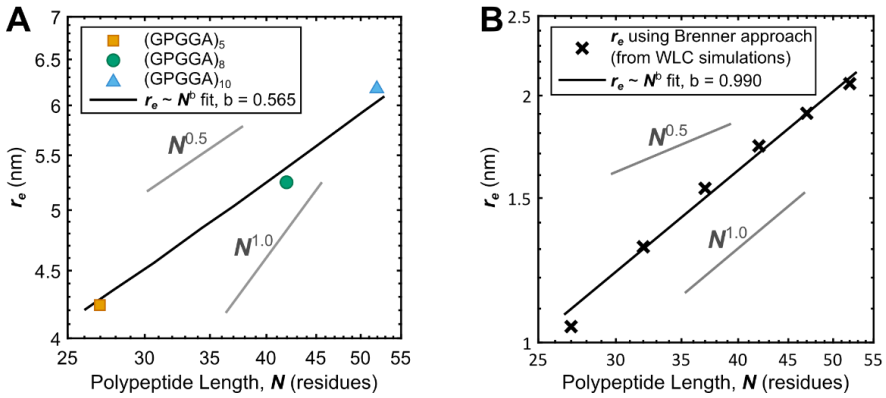

Figure 3.11: Experimental and theoretical examinations of other models [194] of $(GPGGA)_n$ mechanical sensitivity. (A) Measured relationship between average polypeptide end-to-end distance r_e as a function of the number of residues in the $(GPGGA)_n$ extensible domain N shows r_e~N^(1/2) behavior characteristic of unstructured polypeptides; data transformed from Figure 3.9A using the proposed model of TSMod mechanical sensitivity. (B) After simulating unstructured polypeptides of various lengths in the context of the WLC model, calculation of r_e using the approach put forth by [194] yields an artificial r_e~N^1 behavior. Note that plots are logarithmic on both axis such that power-law relationships appear as straight lines.

Next, we investigated the prediction of the observed scaling between ⟨r_e⟩ and N entirely in silico. When the calibration model is used to simulate ⟨E⟩for a collection of TSMods of various lengths N, and subsequently the approach of Brenner et al. is used to

convert these ⟨E⟩ to ⟨r_e⟩, we then observe an apparent ⟨r_e⟩~N^1 scaling over the range of polypeptide lengths examined (25 < N < 50 residues, Figure 3.11B). Note that the polymer mechanics model used as the basis of the calibration model predicts ⟨r_e⟩~$N^{0.5}$ (Figure 3.6B). Thus, we conclude that the observation of a spring-like ⟨r_e⟩~N^1 behavior is a consequence of the assumptions made by Brenner et al., which have previously been shown to lead to poor estimate of ⟨r_e⟩ [200, 214]. In total, these simulations and data show that the calibration model developed in this work is capable of accurately describing the mechanical properties of unstructured polypeptides and suggests that extensible domains based on the consensus sequence $(GPGGA)_n$ fall within this class.

Table 3.4 Model fit parameters compared to literature estimates. Parameters include Förster radius (R_0), fluorescent moiety radius (R_{FP}), and persistence length (L_P).

		Literature Estimates		
FRET-Pair	**Ext. Domain**	**R_0 (nm)**	**R_{FP} (nm)**	**L_P (nm)**
Clover-mRuby2	$(GPGGA)_n$	6.30 (*Lam et al., 2012*)	2.30 (*Hink et al., 2000*)	0.3 - 0.5 (*Becker et al., 2003*)
Clover-mRuby2	$(GGSGGS)_n$	6.30 (*Lam et al., 2012*)	2.30 (*Hink et al., 2000*)	0.45 (*Evers et al., 2006b*)
Cy3-Cy5	$(GPGGA)_{5,8,10}$	5.40 (*Buckhout-White et al., 2014; Sanborn et al., 2007*)	0.95 (*Muddana et al., 2009; Widengren and Schwille, 2000*)	0.3 - 0.5 (*Becker et al., 2003*)

				Constrain R_0 to Lit. Est.		Constrain R_{FP} to Lit. Est.		Constrain R_0 and R_{FP} to Lit. Est.
Experiment	**Environment**	**FRET-Pair**	**Ext. Domain**	**R_{FP} (nm)**	**L_P (nm)**	**R_0 (nm)**	**L_P (nm)**	**L_P (nm)**
Fluorometric#	*in vitro*	Clover-mRuby2	$(GPGGA)_n$	2.31	0.72	6.25	0.70	0.74
Fluorometric#	*in vitro*	Clover-mRuby2	$(GGSGGS)_n$	2.23	0.39	6.49	0.41	0.33
Sens. Em.#	*in cellulo*	Clover-mRuby2	$(GPGGA)_n$	2.42	0.37	5.98	0.33	0.50
Sens. Em.#	*in cellulo*	Clover-mRuby2	$(GGSGGS)_n$	2.34	0.44	6.20	0.43	0.48
FLIM (*Brenner et al., 2016*)	*in vitro*	Cy3-Cy5	$(GPGGA)_{5,8,10}$	0.69	1.24	5.47	1.19	1.15
SM-Pulling (*Brenner et al., 2016*)	*in vitro*	Cy3-Cy5	$(GPGGA)_{5,8,10}$	1.25	0.90	4.80	0.75	1.00

Current work

Table 3.5 Persistence length (L_P) for a variety of published polypeptides. Overall, persistence lengths < 0.2 nm and > 5.0 nm are rarely observed. Synthetic homo-polymers (ex. poly-proline) can achieve larger persistence lengths.

Polypeptide	L_P (nm)	Ref.
Titin	0.2	(*Kellermayer et al., 1997*)
Titin Ig domain	0.4	(*Rief et al., 1997*)
PEVK domain (in titin)	0.55 – 0.65	(*Linke et al., 2002*)
PEVK domain (in titin)	0.92	(*Sarkar et al., 2005*)
Tenascin FN-III domain	0.56	(*Oberhauser et al., 1998*)
Whole spider silk protein	0.3 – 0.5	(*Becker et al., 2003*)
Poly-glycine	0.41	(*Evers et al., 2006b*)
Poly-alanine	1.76	(*Evers et al., 2006b*)
Poly-proline	22.0	(*Evers et al., 2006b*)
Poly-proline	4.5	(*Schuler et al., 2005*)
Panel of short peptides	0.53 – 1.09	(*Ohashi et al., 2007*)
Elastin	0.19	(*Valiaev et al., 2008*)
$(GGSGGS)_n$	0.45	(*Evers et al., 2006b*)
$(GPGGA)_n$ – *in vitro*	0.74	This work
$(GGSGGS)_n$ – *in vitro*	0.33	This work
$(GPGGA)_n$ – *in cellulo*	0.5	This work
$(GGSGGS)_n$ – *in cellulo*	0.48	This work

3.3.3 Summary of model validation in unloaded conditions

To validate this model, we first investigated its ability to describe the behavior of several types of TSMods in terms of the relationship between FRET and the length of the extensible domain in unloaded conditions. These measurements are critical in that they are used to estimate the mechanics of the extensible domain in terms of its persistence length L_P. To do so, estimates of R_0 and R_{FP} were obtained from the literature, L_C was directly calculated from the number of acids comprising the extensible domain, and L_P was used as the single adjustable parameter. With only L_P left unconstrained, the model accurately describes the behavior of TSMods containing $(GPGGA)_n$ and $(GGSGGS)_n$ extensible domains in unloaded conditions in in vitro (Figure 3.1G) and in cellulo (Figure 3.1H) environments with physically reasonable estimates of L_P. Model fits and 95% confidence intervals confirm that L_P estimates for $(GPGGA)_n$ and $(GGSGGS)_n$

polypeptides are significantly different in vitro (0.74 ± 0.05 and 0.33 ± 0.05 nm, respectively), and collapse to one intermediate value in cellulo (0.50 ± 0.02 and 0.48 ± 0.05 nm, respectively) (see Table 3.4 for comparisons). Also, to demonstrate that the literature estimates of R_0 and R_{FP} were appropriate, we performed a sensitivity analysis, leaving either R_{FP} or R_0 unconstrained. We observe negligible improvement in fit quality and achieve similar estimates of L_P (Figure 3.7, Figure 3.8), validating our approach. Overall, these results demonstrate the functionality of the model to measure the L_P of TSMod extensible domains in unloaded conditions and also suggest that the observed mechanics of the extensible domain can change in different environments, although less-so for $(GGSGGS)_n$ polypeptides.

3.3.4 Summary of model validation in loaded conditions

Next, we sought to examine the generalizability of the model as well as validate the ability of the model to describe the behavior of TSMods subject to tensile loads. Therefore, we examined model fits to published fluorescence-force spectroscopy measurements of Cy3-Cy5 dyes linked by $(GPGGA)_n$ extensible domains[194]. Again, with only $\mathbf{L_P}$ unconstrained, the model accurately describes the behavior of these TSMod-like constructs in both unloaded conditions (Figure 3.9A) and under tensile loads (Figure 3.9B). Importantly, each of these datasets is well-described by the same persistence length (L_P = 1.05 nm) indicating that the same mechanical model is appropriate for describing the behavior of unstructured polypeptides in both unloaded and loaded conditions when both measurements are determined in the same

environment. For comparison, we show fits for a range of L_P values from 1.0 to 1.15 nm (lines in Figure 3.9A, shaded region in Figure 3.9B). The robustness of these fits to various parameter constraints was also verified (Figure 3.10). It is important to note that the different estimate of L_P for $(GPGGA)_n$ determined from these measurements in Figure 3.1 is consistent with the idea that in vitro calibration should be applied to sensors used in living cells with caution.

3.3.5 A novel approach for predicting the in cellulo calibration of TSMods

Together these results suggest a simple model-based calibration scheme in which measurements of extensible domain mechanics (L_P) in unloaded conditions can be utilized to predict TSMod behavior under tensile loading. While our modeling efforts indicate that both $(GPGGA)_n$ and $(GGSGGS)_n$ polypeptide mechanics are consistent with unstructured polypeptides (Figure 3.11), we only generate calibration predictions for TSMods containing $(GGSGGS)_n$ extensible domains because they are also less sensitive to environmental changes. In the context of the model, the in cellulo persistence length of the $(GGSGGS)_n$ extensible domain (L_P = 0.48 nm, Figure 3.1H) is combined with literature estimates of the radii [221] and photophysical properties [199] of Clover and mRuby2 to predict the response of $(GGSGGS)_n$-based TSMods under applied loads (Figure 3.9C). This model-based calibration scheme uniquely overcomes the environmental sensitivity of the extensible domain (compare Figure 3.1G and H) by

allowing for in cellulo measurements of L_P to be used to estimate the mechanical sensitivity of TSMods.

3.3.6 Optimized tension sensor reveals gradients of vinculin tension across FAs

To determine which extensible domain length will be optimal for measuring tension across vinculin, we evaluated TSMod mechanical sensitivity across different force regimes by calculating the derivative along the FRET-force curve (Figure 3.9C, Figure 3.12). Given the original vinculin tension sensor (VinTS) reported average loads of ~2.5 pN across vinculin that varied from 1 to 6 pN [131], we choose to further investigate the performance of the TSMod containing the nine-repeat extensible domain, as it exhibits the highest sensitivity in this force regime and is capable of capturing the distribution of the loads on vinculin (Figure 3.12A). This nine-repeat linker also provides a good balance between FRET dynamic range and peak sensitivity (Figure 3.12B, C). An optimized VinTS (opt-VinTS) was created by genetically inserting this TSMod into vinculin at same site, after amino acid 883, as in the original VinTS design [131].

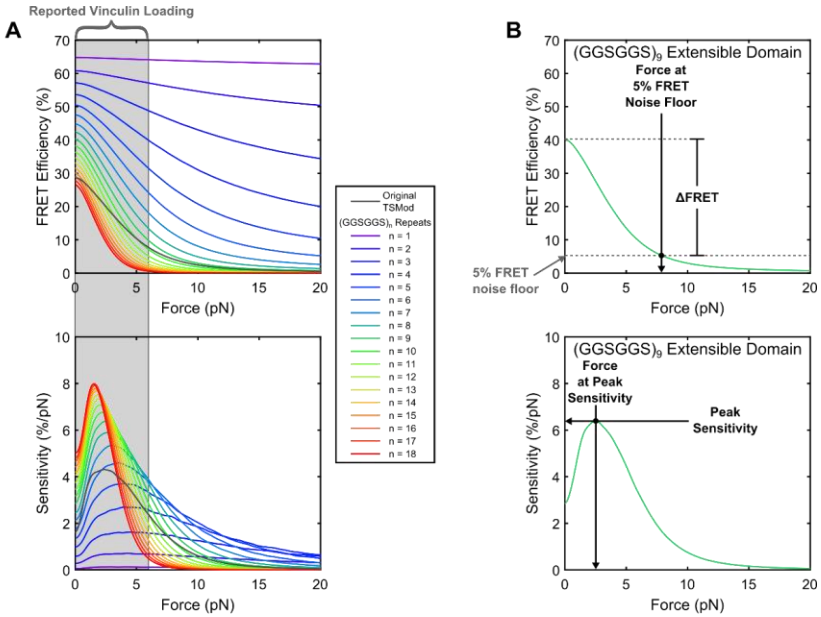

C

	Extensible Domain	maximize ΔFRET (%)	optimize Force at 5% FRET Noise Floor (pN)	maximize Peak Sensitivity (%/pN)	optimize Force at Peak Sensitivity (pN)
TSMod (reference) →	$(GPGGA)_8$	23.7	7.4	4.32	2.4
Clover-mRuby2 based sensors with $(GGSGGS)_n$ extensible domain	n = 1	59.8	> 30	0.13	2.9
	n = 2	56.0	> 30	0.71	4.2
	n = 3	52.5	> 30	1.62	4.5
	n = 4	49.3	> 30	2.70	4.0
	n = 5	46.3	> 30	3.70	4.1
	n = 6	43.7	20.7	4.59	3.5
	n = 7	41.2	13.1	5.34	3.0
	n = 8	39.0	9.9	5.90	2.7
	n = 9	37.0	8.1	6.39	2.5
	n = 10	35.2	6.9	6.76	2.3
	n = 11	33.5	6.1	7.07	2.0
	n = 12	32.0	5.4	7.34	2.0
	n = 13	30.6	4.9	7.50	1.8
	n = 14	29.2	4.5	7.68	1.8
	n = 15	28.0	4.2	7.78	1.6
	n = 16	27.0	3.9	7.90	1.6
	n = 17	25.9	3.6	7.99	1.6
	n = 18	24.9	3.4	7.97	1.5

Figure 3.12: Selection of optimal $(GGSGGS)_n$ extensible domain length in a Clover-mRuby2 based TSMod for measuring ~1-6 pN loads borne by vinculin. (A) Predicted force sensitivities of TSMods containing "minimal" Clover-mRuby2 FRET pair and $(GGSGGS)_n$ extensible domains (n = 1 to 16). (B) Schematic of metrics used to quantify and compare different aspects of TSMod mechanical sensitivity, which describe sensor sensitivity (ΔFRET, top; Peak Sensitivity, bottom) and functional force measurement regimes (Force at 5% FRET noise floor, top; Force at Peak Sensitivity, bottom) (C) Graphical comparison of TSMod mechanical sensitivity properties; green indicates favorable value for a given metric. Nine-repeat $(GGSGGS)_n$ extensible domain shows similar force range as original TSMod (column 2) as well as a good balance between ΔFRET (column 1) and Peak Sensitivity (column 3), which are inversely proportional.

We assessed the performance of opt-VinTS by evaluating its ability to detect changes in vinculin loading across both subcellular and FA length scales. Vin-/- MEFs expressing either VinTS or opt-VinTS showed indistinguishable cell and FA morphologies (Figure 3.13A, A′, C, C′, Figure 3.14). Furthermore, line scans of acceptor intensity across single FAs indicated similar localization of each sensor (Figure 3.13A′′, A′′′, C′′, C′′′). These findings indicate that the two sensors exhibit identical biologically functionality. At a subcellular length scale, consistent with our previous findings [202], both VinTS and opt-VinTS report highest loads (lowest FRET efficiency) in the cell periphery, and no appreciable tensile loading of vinculin in the cell center (Figure 3.13B, D). Based on previous reports of gradients of vinculin loading within individual FAs [228] and a skewed distribution of mechanical stresses at the cell-substrate interface [101, 126, 229, 230], we expected to see similar distally-skewed vinculin tensions. Such gradients are difficult to discern in peripheral FAs of cells expressing the original tension sensor (Figure 3.13B′, B′′, B′′′). However, individual FAs in the periphery of cells expressing opt-VinTS revealed striking gradients of vinculin tension across single FAs (Figure 3.13D′, D′′, D′′′). Quantification of FRET efficiency change across length-normalized FAs (Figure 3.13B′′′, D′′′) reveals an almost 200% improvement in the performance opt-VinTS when compare the original design. In total, these results show that, as predicted by the model, opt-VinTS is significantly more sensitive than the original VinTS.

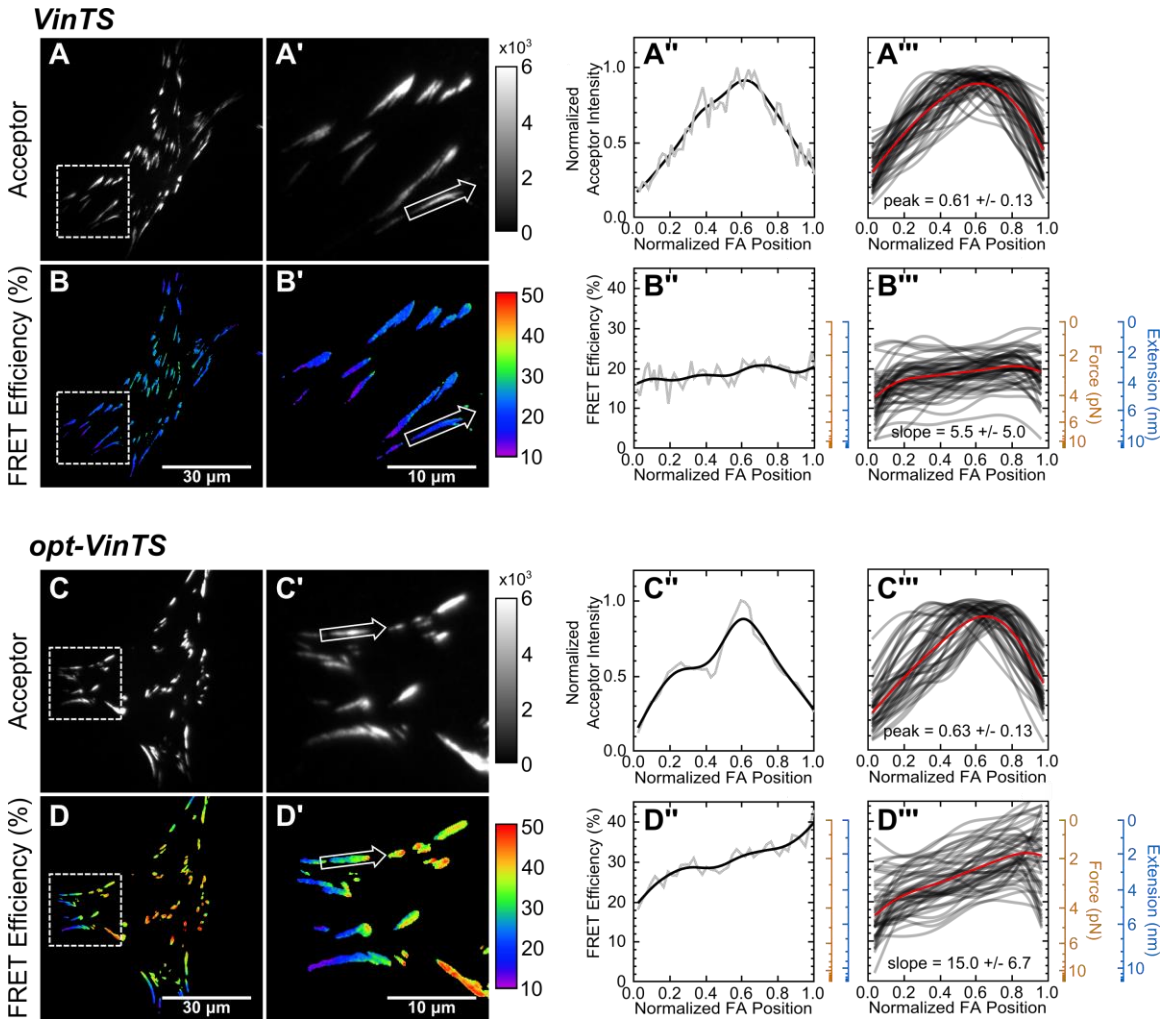

Figure 3.13: Optimized tension sensor reveals sub-FA gradients in vinculin tension. (panels A and B) Representative images of subcellular distribution of VinTS [131] (A, A') along with representative (A'') and aggregate (A''') line scans of single FAs of size > 0.5 mm^2 and axis ratio > 1.5; corresponding masked FRET images (B, B') and line scans (B'', B'''); n = 55 FAs from n = 11 cells from three independent experiments; averaged intensity and FRET profiles in red. (panels C and D) As in panels A and B, but with optimized opt-VinTS construct; n = 49 FAs from n = 10 cells from three independent experiments.

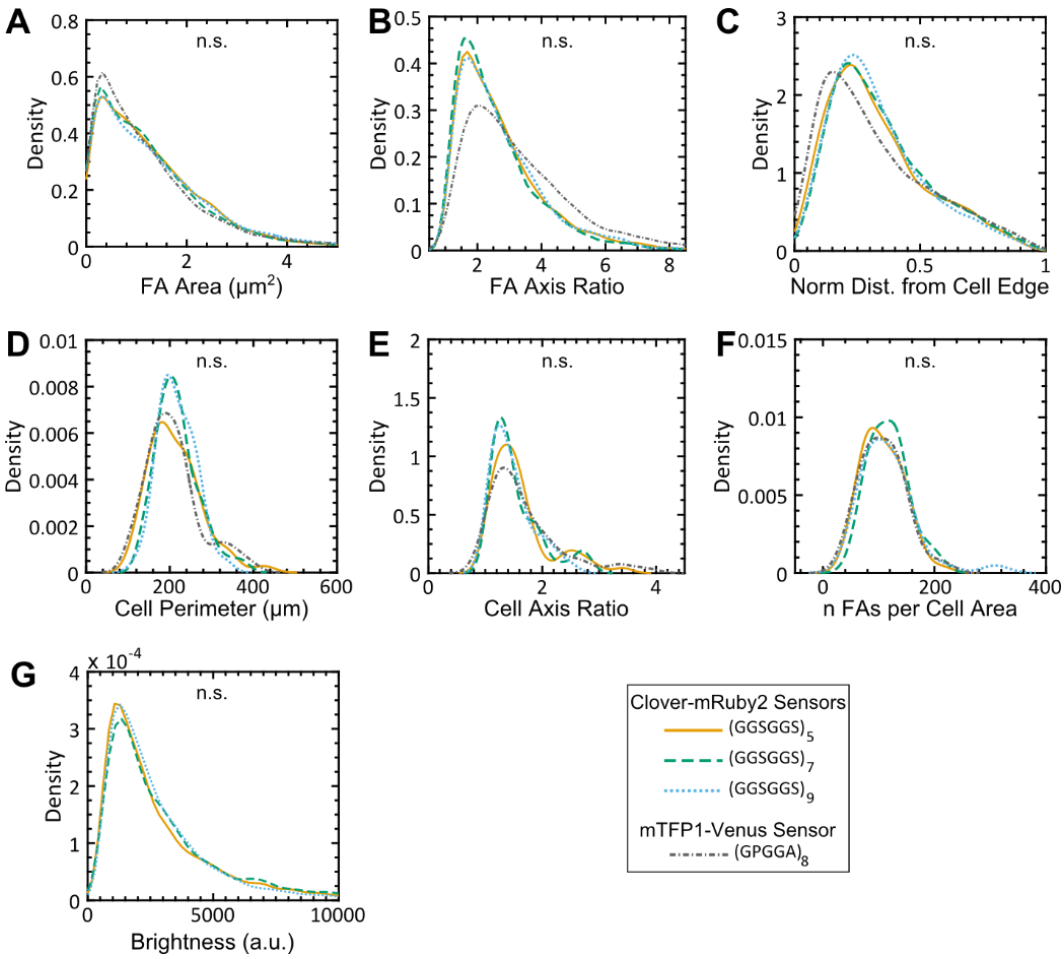

Figure 3.14: FA morphologies, cell morphologies, and sensor localization to FAs are indistinguishable between different versions of VinTS. (A-G) Vin-/- MEFs expressing various version of VinTS show indistinguishable FA area (A), FA axis ratio (B), subcellular distributions quantified as normalized distance from cell edge (C), cell perimeter (D), cell axis ratio (E), number of FAs normalized by cell area (F), sensor localization to FAs in terms of mean acceptor intensity (brightness) (G). Different versions of the tension sensor include those constructed with minimal Clover-mRuby2 modules containing three distinct extensible domains, namely $(GGSGGS)_5$ (n = 54 cells), $(GGSGGS)_7$ (n = 40 cells), $(GGSGGS)_9$ (n = 33 cells), along with the original TSMod containing a $(GPGGA)_8$ extensible domain (n = 48 cells), each from 3 independent experiments; n.s. not significant ($p \geq 0.05$), ANOVA. See Table 3.3 for exact p-values.

3.3.7 Vinculin loading is subject to an extension-based control mechanism

A central premise of mechanotransduction, the process by which cells sense and respond to mechanical stimuli, is that applied loads induce conformational changes in mechanosensitive proteins, leading to biochemically distinct functions. However, it is unknown whether the forces or the extensions experienced by proteins mediate the activation of mechanosensitive signaling pathways. Experimental evaluation of this molecular-scale question has been challenging because force and extension are inherently linked. For example, in the case of molecular tension sensors, the force-extension relationship for the extensible domain is monotonic, so any given force corresponds to a unique extension (Figure 3.15). Therefore, to determine whether conserved forces or extensions mediate vinculin loading, we created a trio of vinculin tension sensors with extensible domains comprised of five, seven, or nine repeats of $(GGSGGS)_n$. As each sensor has a unique force-extension curve, the application of equivalent forces to the three constructs will result in three distinct extensions, and vice versa (Figure 3.15).

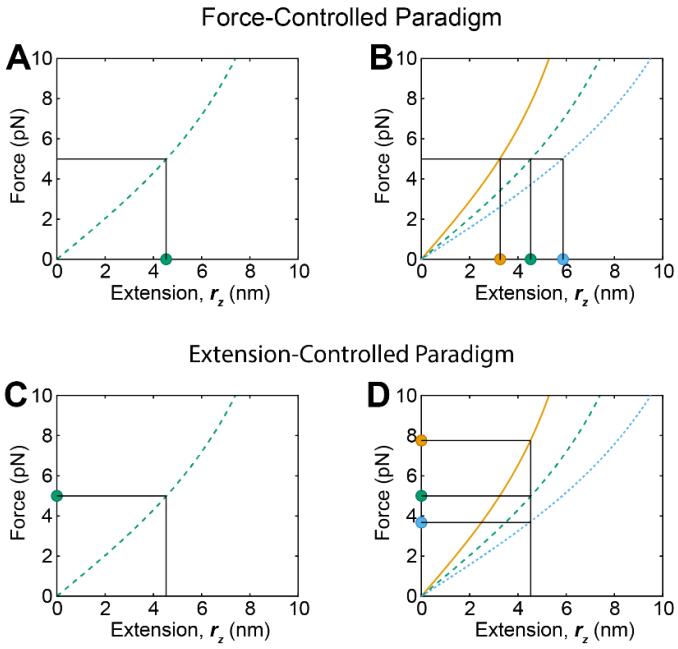

Figure 3.15: Schematic depiction of force-extension relationships and potential force- and extension-control paradigms. (A, B) A force-controlled paradigm cannot be detected if only a single sensor is used (A) but can be discerned if multiple sensors report the same forces, but distinct extensions (B). (C, D) An extension-controlled paradigm also cannot be detected if a single sensor is utilized (C) but can be uncovered if multiple sensors report the same extension and therefore distinct forces across a protein of interest (D). Curves are predictions of the force-extension curve of the WLC model with persistence lengths of 0.5 nm and contour lengths corresponding to the $(GGSGGS)_{5,7,9}$ linkers utilized in this study (orange, green, and blue, respectively).

Cells expressing equivalent amounts of each sensor spread and formed FAs normally (Figure 3.14, Figure 3.16). Using the in cellulo calibration predictions described above (shown in Figure 3.9C), measured FRET efficiencies (Figure 3.16E-H) were converted to sensor forces (Figure 3.16I-L) and extensions (Figure 3.16M-P). Intriguingly, we observed similar distributions of extension (Figure 3.16P), and distinct distributions of tensile forces (Figure 3.16L) in the various sensors. This result strongly suggests that loads across vinculin are governed by an extension-based control rather than the more commonly assumed force-based control paradigm.

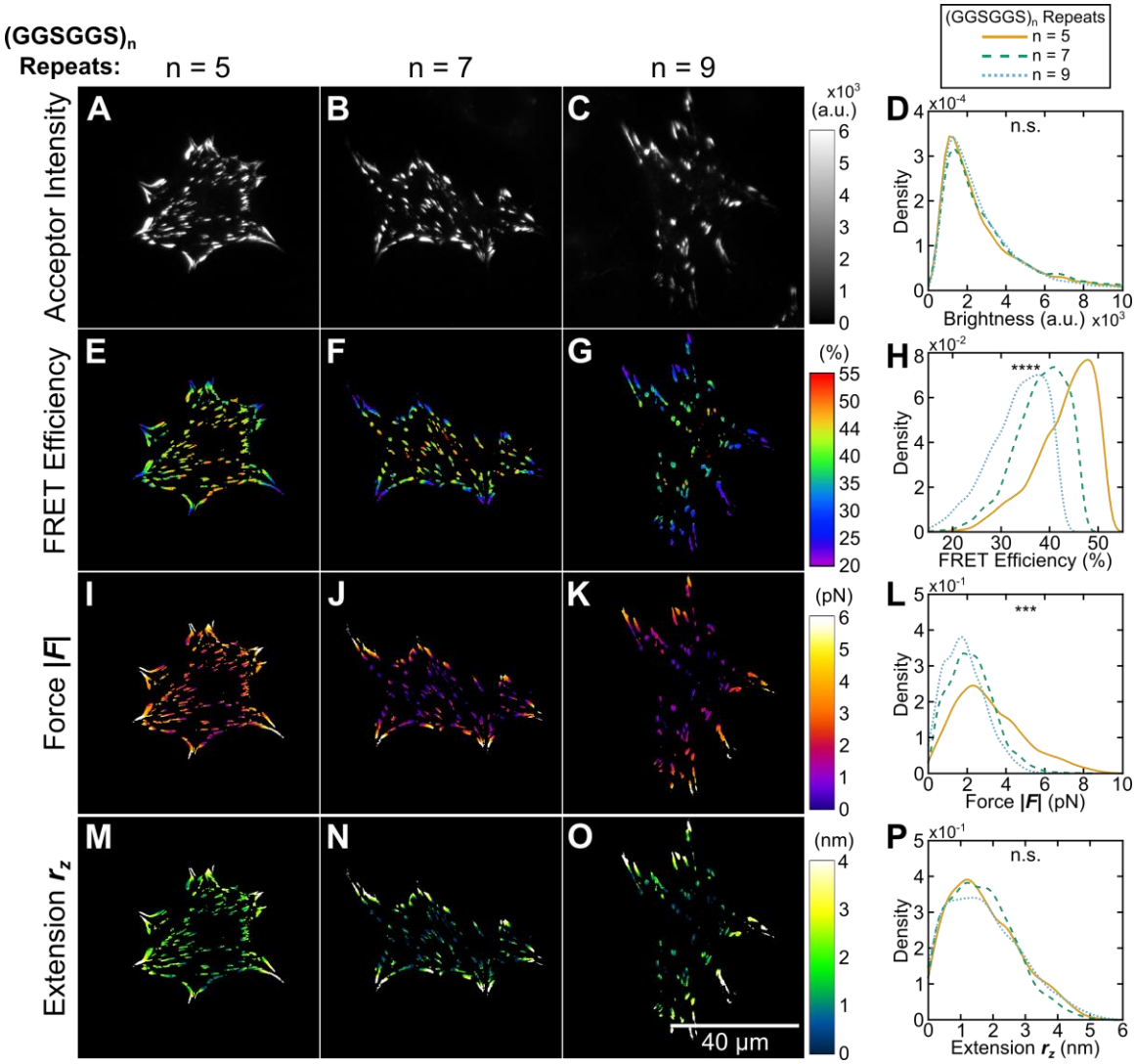

Figure 3.16: Using tension sensors with distinct mechanical sensitivities to test force-based versus extension-based control of vinculin loading. (A-C) Representative images of the localization of a trio of vinculin tension sensors to FAs. (D) Normalized histograms of acceptor intensities at FAs is indistinguishable between the three sensors. (E-G) Representative images of masked FRET efficiency and (H) normalized histograms of average FA FRET reported by each sensor. (I-K) Representative images of forces and (L) normalized histograms of average vinculin tension in FAs reported by each sensor. (M-O) Representative images of extension and (P) cumulative distributions of average vinculin extension in FAs reported by each sensor; n = 54, 40, 33 cells and n = 5618, 4837, 4195 FAs for $(GGSGGS)_{5,7,9}$ extensible domains, respectively; data pooled from three independent experiments; **** $p < 0.0001$, *** $p < 0.001$, n.s. not significant ($p \geq 0.05$), ANOVA. See Table 3.3 for exact p-values and multiple comparisons test details.

3.3.8 Examining extension-based control of vinculin loading with a structural model of a FA

Experiments that showed extension-based control of vinculin loading (Figure 3.16) leveraged three tension sensors with unique force-extension relationships, which were dictated by the unique mechanical responses of the extensible $(GGSGGS)_n$ polypeptide domains. Seeking to gain a better understanding of what kinds of physical interactions might give rise to force-controlled versus extension-controlled loading of different FA components, we developed a simple structural model of a single FA. The FA structural model consists of 170 elements each of which is described as a Hookean spring and can be conceptualized as either a "sensor" element or an alternative "linker" element. Based on the reported stratified organization of layers of proteins within FAs [68], we arranged the two elements in two parallel layers (Figure 3.17A). However, even with this simplified geometry, numerous scenarios are possible. Key variables include the relative stiffness and relative abundance of each element, as well as whether a bulk force input or a bulk extension input is provided to the structure. Therefore, the focus of these modeling efforts was to determine how the force-controlled or extension-controlled loading of individual FA proteins might be impacted by each of these variables in a variety of scenarios.

To examine a single possible physical scenario, structural models were considered in groups of three (Figure 3.17B), since experimental evaluation of force-based versus extension-based control similarly involved three sensors with distinct

mechanical properties (Figure 3.16). Within each grouping of three, the stiffness of the linker elements, k_L, is held constant and only the stiffness of the sensor element was varied (k_{S1}, k_{S2}, or k_{S3}). The stiffness values used for k_{S1}, k_{S2}, and k_{S3} were selected to approximate the relative differences in stiffness between the $(GGSGGS)_{5,7,9}$ extensible domains used in experiments and were estimated from linear fits to their predicted force-extension curves (Figure 3.15). Figure 3.17B depicts a single scenario in which equal numbers of sensor and linker elements ($N_S = N_L$) with comparable average stiffness ($\langle k_{Sj} \rangle = k_L$) are loaded by a bulk extension input (δ_0) as an illustrative example.

Within any particular geometry, we evaluated the extent of force-controlled versus extension-controlled loading of the three distinct sensor elements. Following bulk loading of the structure, which in the illustrative case corresponds to a constant extension δ_0, we solve for the extension of and force across the sensor elements in each of the three assemblies (δ_{Sj} and F_{Sj}, respectively). The extent of extension- controlled versus force-controlled mechanical behaviors is then evaluated by comparing the coefficient of variations, which is defined as standard deviation divided by the mean and abbreviated CV here, of the forces $CV(F_{Sj})$ and extensions $CV(\delta_{Sj})$ experienced by these three different stiffness sensor elements. A control metric quantitatively relating the two magnitudes of variation is defined as the $\log_2$ ratio of the two coefficients of variation:

$$Control\ Metric = \log_2 \left[\frac{CV(F_{Sj})}{CV(\delta_{Sj})} \right] \tag{1}$$

In an extension-controlled assembly the forces will vary more than the extensions $CV(F_{Sj}) > CV(\delta_{Sj})$, resulting in a large and positive control metric, while the opposite will be true for a force-controlled assembly where $CV(F_{Sj}) < CV(\delta_{Sj})$. In the balanced scenario depicted in Figure 3.17B, which contains equal numbers of sensor and linker elements of identical average stiffness, we observe neither extension nor force control following a bulk extension input to the assemblies. Thus, the control metric is close to zero.

In this framework, we investigated the effects of both bulk force (F_0) and extension (δ_0) inputs to a variety of stratified structures comprised of variable abundances and stiffnesses of the two types of springs (Figure 3.17C). To accomplish this, the above calculations were repeated while the relative number of springs and k_L were varied. As we are most interested in relative rather than absolute numbers of elements and element stiffness, the relative numbers and mechanics of the sensor and linker elements are defined as:

$$Relative\ Abundance = \frac{N_S}{N_L} \tag{2}$$

$$Relative\ Stiffness = \frac{\langle k_S \rangle}{k_L} \tag{3}$$

The number of sensor and linker elements (N_S and N_L, respectively) and the stiffness of the linker element (k_L) were set such that the relative abundance and relative stiffness of the two elements varied between 2^{-4} and 2^4. Note that when calculating the relative stiffness, the three distinct spring constants for the three sensor elements were averaged

together. This definition is appropriate as the variation of the stiffness of the sensors springs (k_{Sj}) is significantly smaller (~30% variation) than the range of k_L that was evaluated. These normalized parameters also allow us to draw conclusions that are independent of the absolute values of k and N that are simulated.

With a bulk force input (F_0), simple relationships that obey Hooke's Law are observed, and F_0 is evenly distributed across each sensor element:

$$F_{Sj} = F_0/N_S \tag{4}$$

where F_{Sj} refers to force observed in one of three group models. Subsequently, the force F_{Sj} dictates the extension δ_{Sj} of individual sensor elements following:

$$\delta_{Sj} = F_{Sj}/k_{Sj} \tag{5}$$

In this mechanical assembly, force F_{Sj} remains constant regardless of the stiffness of the sensor element k_{Sj}, while extension δ_{Sj} of the sensor element scales inversely with its stiffness k_{Sj}. This simple solution, where forces are constant, and extensions change with sensor element stiffness, is a prime example of an assembly exhibiting force-based control.

In response to a bulk extension input (δ_0), more complex behaviors are observed. We must first determine the total force F across the assembly following Hooke's Law for springs in series:

$$F = \delta_0 * \left(\frac{1}{k_{Sj} * N_{Sj}} + \frac{1}{k_L * N_L} \right)^{-1} \tag{6}$$

where the effective spring constant for the whole assembly is given by:

$$\left(\frac{1}{k_{Sj} * N_{Sj}} + \frac{1}{k_L * N_L} \right)^{-1} \tag{7}$$

Calculating F_{Sj} and δ_{Sj} as before (Eq. 4 and 5), it becomes apparent that both F_{Sj} and δ_{Sj} will change depending on the relative abundance and stiffness of the sensor and linker elements.

By performing this operation over a variety of relative abundance and stiffness of the sensor and linker elements, we begin to understand what kinds of structural arrangements could give rise to force-controlled versus extension-controlled loading of FA components (Figure 3.17D). Specifically, the assemblies most biased toward extension-controlled behaviors involve linker elements that are much stiffer and/or in greater molecular abundance as compared to sensor elements. However, in the opposite scenario, force-controlled loading could be observed even following a bulk extension input. The sensitivity of the control paradigm to sensor and linker element stiffness and abundance indicates that force-controlled and extension-controlled scenarios are likely mutable and highly dependent upon protein, cellular, and mechanical contexts. In our experimental context, the measured variance in forces and extensions reported by the three sensors (Figure 3.16) indicated a control metric ~1.9 (Figure 3.17D, asterisk). These

measurements indicate, at least for MEFs adhered to fibronectin-coated glass substrates, vinculin exhibits predominantly extension-controlled behavior.

The model also predicts the relationship between sensor element stiffness k_{Sj} and the force borne by the sensor element F_{Sj}. Importantly, for various values of relative abundance or stiffness of the sensor and linker elements, the various control regimes correspond to distinct relationships between sensor element stiffness k_{Sj} and force F_{Sj}. To illustrate this, we investigated three scenarios: a region in the extension-controlled regime consistent with our observations of vinculin, a region where neither force- nor extension-based control is favored, and a region in the force-controlled regime (Figure 3.17D, dashed contour lines). The extension-controlled regime is associated with a linear relationship between sensor element stiffness and force, while the force-controlled regime predicts a constant relationship between these variables, and the intermediate regime corresponds to a relationship between these two limits (Figure 3.17E). The magnitudes of the forces depicted on the y-axis must be considered qualitatively, as they are affected by the magnitude of the bulk extension input (δ_0). Regardless, it is clear that "minimal" Clover-mRuby2 based VinTS with 5, 7, and 9 repeats of a $(GGSGGS)_n$ extensible domain (control metric = 1.9) clearly exhibit a linear relationship between the forces experienced by each sensor and the estimated spring constants, consistent with being in an extension-controlled regime (Figure 3.17E, filled points). Thus, this simple structural model accurately reproduces two distinct features of the mechanical responses observed in the suite of vinculin tension sensors.

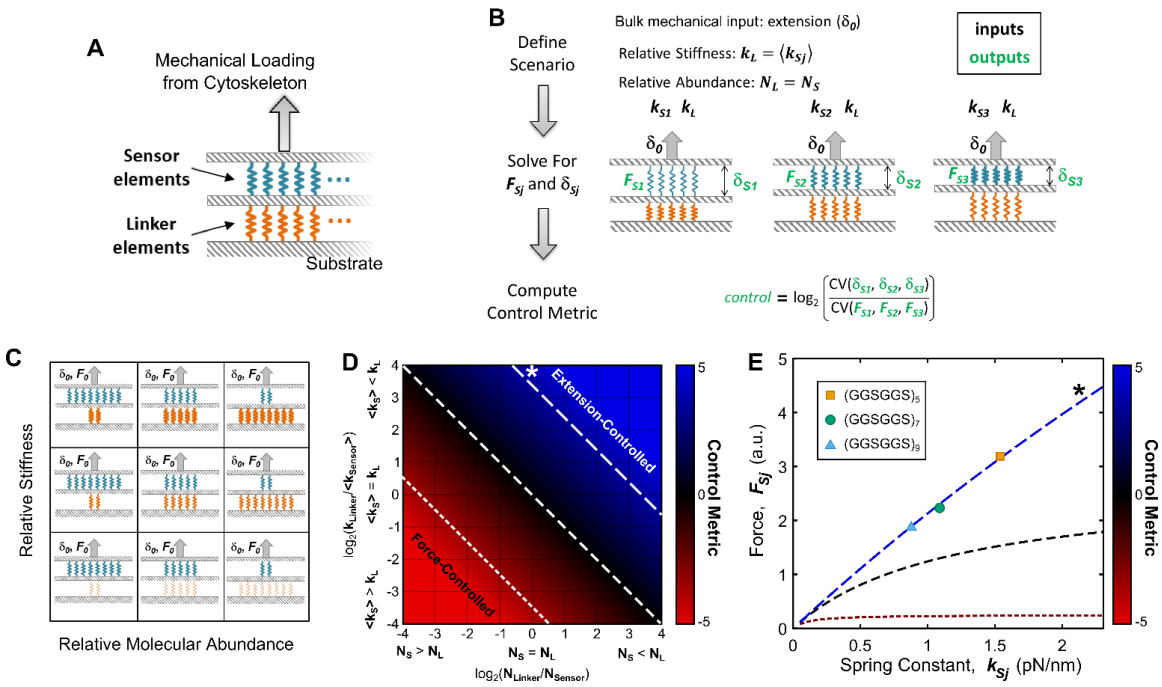

Figure 3.17 Various structural arrangements within FAs could lead to force-based or extension-based control. (A) FA structural model consists of two parallel layers of proteins, which can be conceptualized as either "sensor" (blue) or "linker" (orange) elements. (B) Mimicking what was done in experiments (Figure 3.16), simulations involved three sensor elements with distinct stiffnesses (k_{S1}, k_{S2}, k_{S3}), arranged in a stratified fashion with a single linker element (stiffness k_L), loaded by a bulk extension (or force) input. The forces and the extensions experienced by each sensor element were calculated, and a control metric relating the relative variation in forces to the variation in extensions was calculated. (C) Schematic depiction of parameter space examined using this simple structural model of FAs, wherein the relative number of the sensor and linker element is varied (x-axis) along with their relative stiffness (y-axis); thicker springs indicate stiffer mechanics. (D) Summary of results from simulations quantifying force-controlled versus extension-controlled loading of the sensor element. The Control Metric describes the ratio of variation in forces to the variation in extensions experienced by the sensor elements and will be positive for force-controlled situations and negative for extension-controlled situations. Regions of relative stiffness and abundance are highlighted where, following a bulk extension input, force-controlled loading of the sensor element (sensor element is stiff and in relatively high abundance) or extension-controlled loading of the sensor element (sensor element is soft and/or in relatively low abundance) is observed. (E) FA structural model predictions of the relationship between sensor element stiffness (spring constant) and force, which are linear for the extension-controlled regime (asterisk), and increasingly flat for balanced and force-controlled regimes; dashed contour lines in panel (D) correspond to dashed force-stiffness relationships in panel (E).

Together, these model predictions indicate that the extension-controlled loading of individual FA components is most likely to be observed in response to a bulk extension input, will be observed for soft elements in relatively low abundance, and will result in a linear relationship between sensor element stiffness and load bearing capacity, as has been observed experimentally for vinculin. Determining whether other load-bearing proteins, as well as vinculin in other cellular contexts (ex. three-dimensional matrices), are subject to extension-control will be critically important. By developing a rational-design approach for the creation of calibrated FRET-based tension sensors, we uniquely enable and expedite these types of investigations.

3.3.9 Roadmap for future TSMod design

By expanding the simulated parameter space, the calibration model can also be used to predict the in cellulo mechanical sensitivity of a wide variety of potential TSMod designs. Specifically, as each model parameter corresponds to an alterable variable in sensor design (R_0 = FRET pair, L_P = composition of extensible domain, N = length of extensible domain), we can bypass the need to iteratively "guess and check" the performance of new sensors, and, instead, predict the performance of unstructured polypeptide-based tension sensors in silico. Since our measurements and modeling efforts indicate that both force and extension might be key mechanical variables in different contexts, we report the predicted mechanical responses for simulated sensors in terms of both force and extension. The predicted relationships between force, extension, and FRET for a single sensor can be concisely described by three metrics as depicted in

Figure 3.18A-C: (1) a FRET dynamic range (ΔFRET), which is defined as the change in FRET efficiency from an unloaded state to an experimentally-determined 5% noise floor; (2) a target force (F_{target}), which indicates the midpoint of force range a sensor is functional, and is defined as $F_{target} = \Delta F/2$; and (3) a target extension ($r_{z,target}$), which is analogous to target force. Examining the predicted ΔFRET, F_{target}, and $r_{z,target}$ for a variety of Clover-mRuby2 TSMods containing extensible domains of various lengths and compositions, we generate a "roadmap" for future Clover-mRuby2 sensor design (Figure 3.18D-F, see Table 3.5 for a list of reported polypeptide mechanical properties justifying the range over which simulations were performed). Additional roadmaps were generated for other commonly used FRET pairs (Figure 3.19). With these roadmaps as a guide, the rational design and implementation of future tension sensors with diverse and a priori specified properties is now possible.

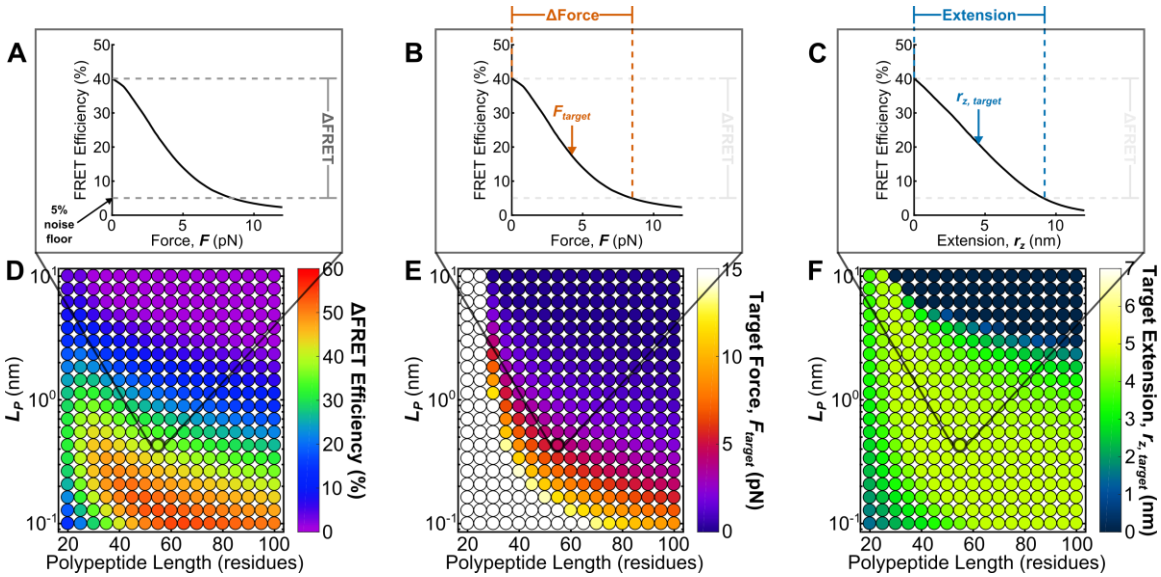

Figure 3.18: Roadmap to enable the rational design of FRET-based molecular tension sensors. (A-C) Representative plots of relationships between FRET efficiencies, forces, and extensions reported by a single sensor, highlighting ΔFRET (A), ΔForce (B), and polypeptide extension r_z (C) required to stretch a sensor from its resting state to the 5% FRET noise floor. (D-F) Parameter space highlighting the predicted ΔFRET at the 5% noise floor (D) as well as the target force F_{target} (E) and target extension $r_{z,target}$ (F) predicted for a variety of Clover-mRuby2-based sensors with a variety of polypeptide lengths (x-axis), and polypeptide mechanical properties (y-axis). Each point represents a single potential TSMod design.

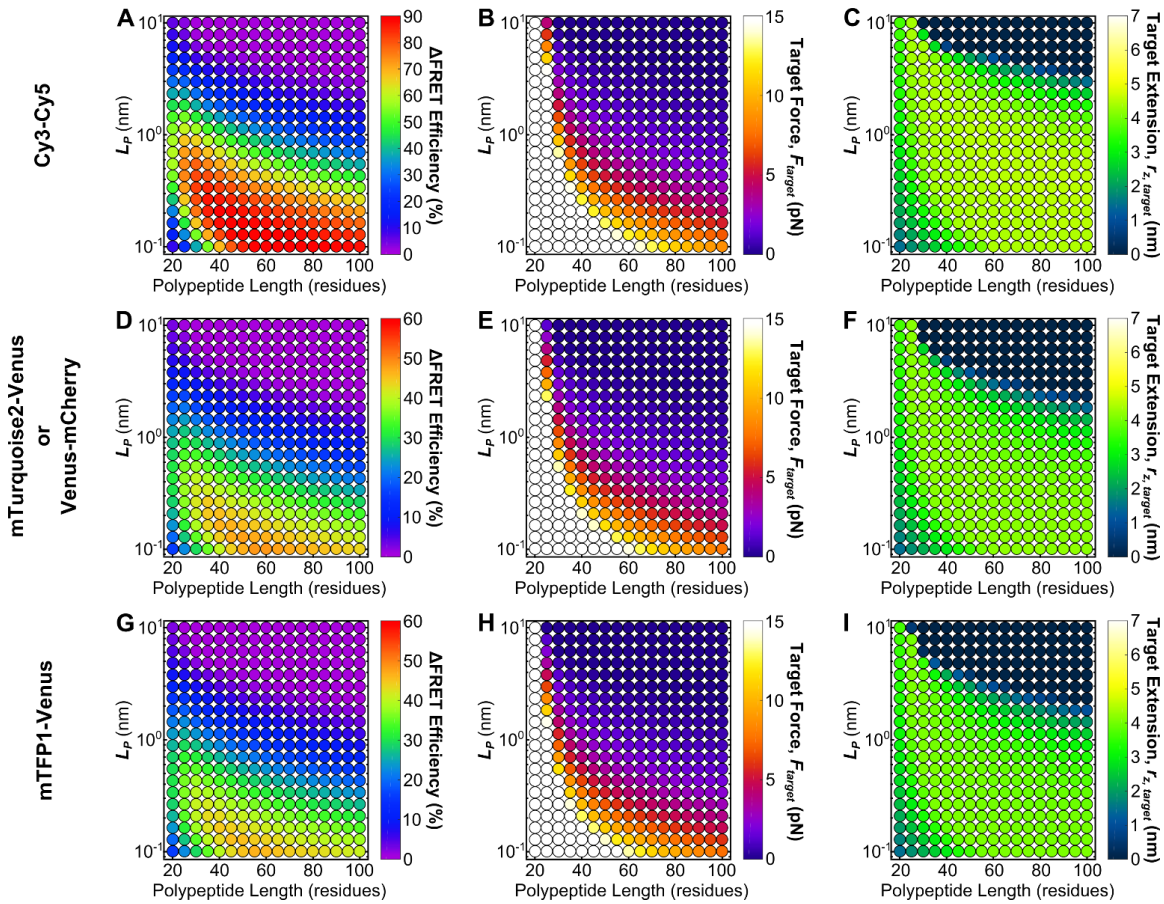

Figure 3.19: Roadmaps to guide the rational design of FRET-based molecular tension sensors for some commonly used FRET-pairs. Parameter space highlighting the predicted ΔFRET at the 5% FRET noise floor (A, D, G), as well as corresponding target force, F_{target} (B, E, H), and target extensions $r_{z,target}$ (C, F, I), for a variety of Cy3-Cy5 (A-C), Venus-mCherry or mTurquoise2-Venus (which have identical R_0) (D-F), and mTFP1-Venus (G-I), based sensors with a variety of polypeptide lengths (x-axis), and mechanical properties (y-axis). Each point represents a single potential tension sensor design.

3.4 Discussion

3.4.1 Updating TSMod design principles

In this study, we created and characterized a suite of molecular tension sensors with improved, predictable, and tunable force sensitivities. Through these

improvements, which included a switch to the Clover-mRuby2 FRET pair, the use of "minimal" FPs, and the modulation of the length and composition of the unstructured polypeptide-based extensible domain, we encountered surprising context-dependent mechanical responses in various TSMods. These context-dependent responses question the applicability of in vitro (single molecule-based) calibrations to sensors that are almost exclusively utilized in cellulo. To overcome this obstacle, we developed and validated a first-principles model which predicts TSMod mechanical sensitivity using in cellulo measurements of the mechanical properties of unstructured polypeptides used as the extensible domain. Then, guided by this model, we created new sensors that provide the next generation of calibrated TSMods for application to diverse mechanobiological investigations.

3.4.2 Probable causes for vinculin tension asymmetries in FAs

Initial experiments employing these new sensors highlight their enhanced ability to detect asymmetric distributions of molecular tension within single FAs. Similar tension asymmetries have been observed external to the cell using both high resolution traction force microscopy [101, 126] and extracellular tension sensors [229, 230]. Intracellularly, gradients in vinculin tension have been reported in cells adhered to micropost arrays, although tension asymmetries were mainly attributed to the presence of the discontinuous substrates [228]. We show that these asymmetric molecular loads, high at the distal tips and low at the proximal edge of FAs are transmitted through vinculin even on continuous substrates. Tension asymmetries in continuous systems are

likely due to interactions between vinculin and load-transmitting intracellular binding partners, such as F-actin.

3.4.3 Implications of molecular extension-control for rigidity sensing

This next generation of calibrated TSMods also enabled the investigation of a question that was previously technically inaccessible: are the forces across or extensions of proteins subject to cellular control? The observation that vinculin loading is characterized by repeatable patterns of extension suggests that protein extension, rather than force, may govern the activation of vinculin-dependent and possibly other mechanosensitive signaling pathways. Extrapolated to longer length scales, this result agrees well with reports that cells induce similar strains within extracellular environments of differing stiffness [154] and that strain determines the activation of touch-sensitive channels in in vivo models [231]. However, while vinculin appears to be under extension-control in 2D culture systems we note that the simple FA structural model demonstrates that the extent of force-controlled versus extension-controlled protein loading is highly sensitive to the relative abundance and stiffness of various proteins within the bulk structure. Thus, it seems likely that other load-bearing proteins might be subject to either type of control or that a specific protein in distinct cellular contexts could switch control modalities. The prediction of >1000 possible tension sensor designs should allow the creation of tension sensors for any need in either extension- or force-based control paradigms.

3.5 Summary

In sum, this work provides the biophysical foundation for understanding molecular tension sensor function and delivers a suite of in cellulo-calibrated sensors whose distinct and predictable mechanical sensitivities can be leveraged to gain unique molecular understanding of the role of mechanical forces and extensions in biological systems. These advancements should expedite deployment of molecular tension sensors in diverse biological contexts where mechanical cues and cellular force generation have long been thought to play critical, but unexplored, roles.

4 Investigating Asymmetric Distribution of Vinculin Loads Within Individual Focal Adhesions

4.1 Introduction

Both external mechanical cues and internally generated forces have profound effects on FA structure and mechanosensitive signaling [43, 148, 232]. Regardless of their origins, forces transmitted through FAs are borne by discrete molecular linkages within these structures. Studies of isolated proteins have highlighted the potential for force-induced conformational changes [15, 233], phosphorylation events [102, 234], and protein-protein interactions [18, 19, 235], providing probable links between forces and signaling outputs. However, the extent to which these loads and load-induced changes in protein function occur in these complex multi-molecular assemblies inside cells is still debated. Uncovering how forces transmit through specific protein linkages within these molecularly diverse [75] and architecturally complex [68] structures is therefore an essential first step to a mechanistic understanding of FA and cellular mechanosensing [43].

Further complicating the picture of molecular force transmission are the multiple actomyosin architectures. Specifically, measurements of bulk cell-generated forces using traction force microscopy point towards two types of force-generating actin structures. Classically, actomysoin force-generation has been associated with stress fiber (SF) formation [93, 236]. These primarily RhoA-mediated structures form from anti-parallel bundles of F-actin, cross-linked by proteins such as α-actinin [237]. Furthermore, due to

the high concentration of myosin II [238] and enrichment in non-migratory cell types, SFs are typically associated with large forces, cellular contractility, and static stresses. In contrast, other work indicates that the forces arising from actin polymerization and retrograde flow in actin networks proximal to lamellipodial protrusions (LPs) can also generate high traction stresses [99, 146]. Forces in these branched actin networks arise due to both Rac1-mediated actin polymerization [94] as well as myosin II activity [97, 98, 239, 240]. Interestingly, Rac1 protrusion and myosin II contraction contribute to a net rearward movement of actin [97]. Time-lapse images of actin dynamics using fluorescence speckle microscopy [241] gave rise to the term retrograde "flow" [242], implying dynamic, frictional forces load FAs associated with these structures. While forces originating from both structures are high, their dramatically different dynamics and unknown connectivity through complex FA structures warrants further investigation.

Direct visualization of molecular loads using FRET-based tension sensors has provided some insight into the molecular players involved in FA force transmission. In our previous measurements (Chapter 3) vinculin loads varied widely throughout the cell and the highest loads were concentrated at the periphery (Figure 3.13, 3.16). Higher forces in the cell periphery have also been seen for the FA protein talin [140] as well as the actin cross linker filaminA [138], suggesting that forces arising from various actin structures are transmitted through multiple molecular linkages at FAs. Furthermore, in a number of these peripheral FAs, we observed distinct patterns of vinculin loading

within individual FAs. Specifically, we observed highest molecular loading of vinculin at the tip of the FA distal to the cell body, suggesting different connectivity to actin in the front as opposed to the rear of FAs. These spatial gradients in mechanical loading have also been observed using high resolution traction force measurements [101], extracellular tension sensors [229, 230]. However, the actin structures associated with these distinct loading patterns were not determined. Thus, the goal of this chapter was to determine which cytoskeletal structures cause the formation of high loads and spatially varying loads within FAs.

In this chapter we examined the extent to which two distinct actomyosin structures, namely SFs and LPs, contributed to vinculin loading and spatial loading profile in FAs. Interestingly, we observed high vinculin loads (>4pN) in FAs associated with both structures. However, the tensile loading profiles observed in Chapter 3 were an exclusive property of SF-associated FAs. FAs associated with LPs showed uniformly high loads from distal to proximal edge. We monitored the formation of these loads and loading profiles throughout the cell spreading process and found that formation of SFs and gradient loading profiles temporally coincide. Finally, we investigated the molecular determinates of vinculin loading and spatial loading profile in terms of regulation by Rho-family GTPase as well as the requirements for actin binding and talin binding.

4.2 Methods

4.2.1 Cell culture and transfection

Vinculin -/- mouse embryonic fibroblasts (Vin-/- MEFs) were kindly provided by Dr. Ben Fabry and Dr. Wolfgang H. Goldmann [183], (Friedrich-Alexander-Universitat Erlangen-Nurnberg). Vin-/- MEFs were stably modified with various FRET-based vinculin tension sensor constructs using lentiviral transduction methods as described in Chapter 4.2.3. All MEFs were maintained in high-glucose DMEM with sodium pyruvate (D6429, Sigma Aldrich, St. Louis, MO) supplemented with 10% FBS (HyClone, Logan, UT), 1% v/v non-essential amino acids (Invitrogen, Carlsbad, CA), and 1% v/v antibiotic-antimycotic solution (Sigma Aldrich). HEK293 cells were maintained in high-glucose DMEM (D5796, Sigma Aldrich) supplemented with 10% FBS (HyClone) and 1% v/v antibiotic-antimycotic solution (Sigma Aldrich). Cells were grown at 37 °C in a humidified 5% CO_2 atmosphere. Cells were transfected at 50-75% confluence in 12-well tissue culture plates using Lipofectamine 2000 (Invitrogen) following the manufacturer's instructions.

4.2.2 Construction of viral expression plasmids

Construction of pcDNA3.1-VinTS transient expression construct has been described previously [131]. Mutant versions of the vinculin tension sensor deficient in actin binding (I997A) or talin binding (A50I) were generated via PCR. Specifically, the vinculin tail domain with I997A mutation was generated using forward primer 5'-AGC GGC CGC GGA GTT CCC AGA GCA G-3', reverse primer 5'-C ACT GAA TTC TTA

CTG ATA CCA TGG GGT CTT TCT G-3', and template DNA pET15b GgVcl 884-1066 ΔAB (generous gift from S. Campbell). The product was insert into pcDNA3.1-VinTS using 5'-NotI/3'-XbaI, yielding pcDNA3.1-VinTS-I997A. An analogous strategy was used to generate pcDNA3.1-VinTS-A50I using forward primer 5′-AAT AAG CTT GCC ATG CCC GTC TTC CAC AC-3′, reverse primer 5′-GCC GGA TCC GCA AGC CAG TTC-3′, template DNA pEGFP-C1/GgVcl 1-851 A50I mutant (Addgene Plasmid #46269) and 5'-HindIII/3'-BamHI restriction sites. To achieve lentiviral expression of VinTS and mutant VinTS constructs, these constructs plus the upstream CMV-promoter were extracted via 5′NruI/3′XbaI digestion and ligated (T4 DNA Ligase; New England BioLabs, Ipswich, MA) into pRRL vector that had been digested with 5′EcoRV/3′XbaI and dephosphorylated using Antarctic Phosphatase (New England BioLabs, Ipswich, MA).

4.2.3 Generating stable cell lines

Second generation viral packaging plasmids psPax2 (Plasmid #12260) and pMD2.G (Plasmid #12259) were purchased from Addgene. pRRL VinTS and VinTS mutant constructs, psPax2, and pMD2G plasmids were co-transfected into HEK293-T cells using Lipofectamine 2000. After 4 hours, the transfection mixture was exchanged for full media. After an additional 72 hours, media containing viral particles was harvested and stored at -80C.

One day prior to viral transduction, Vin-/- MEFs were plated in 6-well dishes at a density of 100,000 cells per dish. Cells were transduced with 500μL viral mixture in full media supplemented with 2μg/mL Polybrene (Sigma Aldrich) to enhance viral uptake.

After three passages, transduced cells were sorted into several groups based on intensity of the fluorescent signal due to expression of the construct.

4.2.4 Estimating endogenous expression of VinTS constructs

Traditionally, rescue of proteins to endogenous expression levels are estimated via western blot. However, due to species differences between the cells and the DNA constructs being expressed, this was not possible in our system. In place of this approach, we verified endogenous expression level of each vinculin tension sensor construct using an immunofluorescence based-approach where the species differences were less noticeable. Still, an antibody calibration step was required. First, primary antibody species specificity was established by comparing relative immunofluorescent labelling of mouse vinculin-Venus and chicken vinculin-Venus in Vin-/- MEFs with a vinculin antibody (mouse anti-vinculin V9131; Sigma-Aldrich, St. Louis, MO) and a secondary antibody tagged with Alexa-647 (Thermo Fisher Scientific, Waltham, MA). Then, WT MEFs and VinTS-expressing Vin-/- MEFs (VinTS MEFs) were immunofluorescently labeled using the same protocol. Mean intensity for Alexa-647 labeling at FAs in WT MEFs, corrected for antibody specificity, was taken as a standard for endogenous vinculin expression. Mean Venus intensity of VinTS MEFs that also showed the Alexa-647 labeling consistent with this endogenous level was used to determine the sensor expression level that corresponds to endogenous vinculin expression. Subsequent analyses were only performed on VinTS MEFs within this range of acceptor intensities.

4.2.5 Cell seeding and spreading assays

Glass bottom dishes (World Precision Instruments, Sarasota, FL) were incubated with 10 μg/ml fibronectin (Fisher Scientific, Waltham, MA) in PBS at 4ºC overnight. Dishes were rinsed once with PBS prior to cell seeding. VinTS MEFs were seeded at a density of 25,000 cells per dish and allowed to spread in complete media for 4 hours. For cell spreading assays, multiple samples were created and fixed at 15, 30, 60, or 120 minute timepoints post-seeding.

4.2.6 Immunofluorescence

After spreading, cells were rinsed once with PBS and fixed for 10 min with 4% paraformaldehyde (Electron Microscopy Sciences). Cells were then permeabilized in 0.1% Triton-X100 for 5 min at room temperature, rinsed in PBS, then blocked for 1hr with 2% bovine serum albumin (BSA) in PBS (blocking buffer). For experiments involving V14-RhoA-HA or V12-Rac1-HA, anti-HA mouse antibody (sc-7392, Santa Cruz Biotechnologies, 1:100) was diluted in blocking buffer, and applied to samples for 1 hr at RT. After three 5 min rinses with PBS and another 1 hour blocking step, goat anti-mouse AlexaFluor 405 secondary antibody (Life Technologies A31553, 1:500) and AlexaFluor 647 conjugated phallodin (Life Technologies, A22287, 1:100) diluted in blocking buffer were applied to the sample for 1 hr at RT. Finally, cells were rinsed three times and left immersed in PBS for imaging. In place of the primary antibody incubation, AlexaFluor-647 conjugated phallodin was used to label F-actin structures in all experiments other experiments in this chapter.

4.2.7 FRET imaging

FRET imaging was performed as described in Chapter 3.2.3, using combinations of the mTFP1 excitation/emission filters and the Venus excitation/emission filters described therein. In addition to acquiring images in the donor, acceptor, and FRET channels, F-actin structures were visualized in the Cy5 channel (500 ms exposure) using the QUAD filter set described in Chapter 3.2.3. For experiments involving V14-RhoA-HA or V12-Rac1-HA, immunolabeling of HA tag with AlexaFluor 405 secondary antibody was visualized in the DAPI channel (1000 ms exposure) of the QUAD filter set.

4.2.8 FRET image analysis, focal adhesion and cell segmentation

Calculation of FRET efficiency by sensitized emission and subsequent identification and quantification of FAs and cells were performed as described in Chapter 3.2.4.

4.2.9 Gradient quantification

To enable detection of gradient loading profiles (i.e. non-uniform distribution of FRET efficiency), we implemented a calculation based on the comparison of two centroids: a geometric centroid which provides information on the location of the FA and a $FRET^{-1}$-weighted centroid, which is shifted towards areas of higher tension (lower FRET). The intensity weighted centroid for a given imaging channel (e.g. FRET) was calculated using:

$$x_{ch} = \frac{\sum_{pixels} I_{ch,i} x_i}{\sum_{pixels} I_{ch,i}} \; ; \; y_{ch} = \frac{\sum_{pixels} I_{ch,i} y_i}{\sum_{pixels} I_{ch,i}}$$

where $I_{ch,i}$ is the intensity in the imaging channel at a single pixel, x_i is the x position of the pixel, and y_i is the y position of the pixel. Since cells and focal adhesions are randomly oriented in the imaging window, a cell centroid provides the frame of reference required to determine the relative locations of the geometric and $FRET^{-1}$-weighted centroids. Thus, if stronger gradients are defined as more distally skewed tensions (away from the cell center), then the comparison of two distance formulas can provide a measure of gradient strength following:

$$\boldsymbol{Gradient\ Strength} = \sqrt{(x_{FRET^{-1}} - x_{cell})^2 + (y_{FRET^{-1}} - y_{cell})^2} - \sqrt{(x_{geo} - x_{cell})^2 + (y_{geo} - y_{cell})^2}$$

This was used to calculate spatial loading gradient strength or just "Gradient Strength" as depicted in Figures 4.2, 4.3, 4.4, and 4.5.

4.2.10 Statistics

All statistical analyses were performed using JMP Pro 12 software (SAS, Cary, NC). ANOVAs were used to determine if statistically significant differences ($p < 0.05$) were present between groups. If statistical differences were detected, Tukey's HSD or Dunnett's (if a single control group was present for comparison purposes) post-hoc testing were used to perform multiple comparisons and assess statistical differences between individual groups.

4.3 Results

4.3.1 Two distinct spatial profiles of vinculin loading in FAs

To probe how various actin structures contribute to vinculin loading, we stably expressed a FRET-based vinculin tension sensor (VinTS) [131] in vinculin -/- mouse embryonic fibroblast (MEF) cells and plated them on fibronectin-coated glass coverslips for 4 hours. Using quantitative FRET imaging in combination with fluorescent labeling of F-actin with Alexa Fluor 647-conjugated phalloidin, we were able to simultaneously visualize vinculin tension (inversely proportional to FRET efficiency) and actin structures. We observed FAs primarily associated with two actin structures: stress fibers (SFs, which includes both ventral and dorsal populations), and lamellipodial protrusions (LPs) (Figure 4.1A). Other classes of F-actin structure such as ventral arcs and filopodia are rarely observed in this system.

Consistent with our observations from Chapter 3, VinTS localization and distribution within each type of FA were indistinguishable as measured by peak acceptor intensity location and multiple line scans across individual FAs (Figure 4.1B-D). Furthermore, visualizing FRET signals from segmented FAs, we observed high vinculin loads in both SF- and LP-associated FAs (Figure 4.1E). FRET efficiencies frequently <15% (>4pN force) were observed in FAs associated with both actin structures. In contrast, FAs positioned more central under the cell body exhibited FRET efficiencies consistent with an unloaded state as measured by soluble TSMod (E = 28.6%). We have previously shown that these subcellular variations in VinTS FRET efficiency are absent in cells

expressing soluble TSMod [202], indicating that differences reflect changes in vinculin loading rather than differences in cell thickness, pH, or crowding throughout the cell.

While average loads across vinculin in each type of FA were comparable (Figure 4.1E), closer examination of VinTS loading across individual FAs showed marked differences between vinculin in SF- and LP-associated FAs (Figure 4.1A, R1 and R2, respectively). In contrast to the indistinguishable sensor localization between the two types of FAs, the pattern of vinculin loading was strikingly distinct. Specifically, user-drawn line scans quantifying acceptor intensity (proportional to sensor concentration) and FRET efficiency change across length-normalized FAs revealed that the asymmetric or gradient loading of vinculin we previously observed is due to loading from SF termini. In these SF-associated FAs, VinTS FRET efficiencies were lowest towards the distal tip, reaching <10% FRET efficiency (>6pN force) in some instances (Figure 4.1F). In contrast, vinculin with LP-associated FAs showed uniformly high loading (Figure 4.1G). Based on these qualitative observations, we decided to investigate further into the relationship between SF formation and the emergence of spatial gradients in the mechanical loading of vinculin in SF-associated FAs.

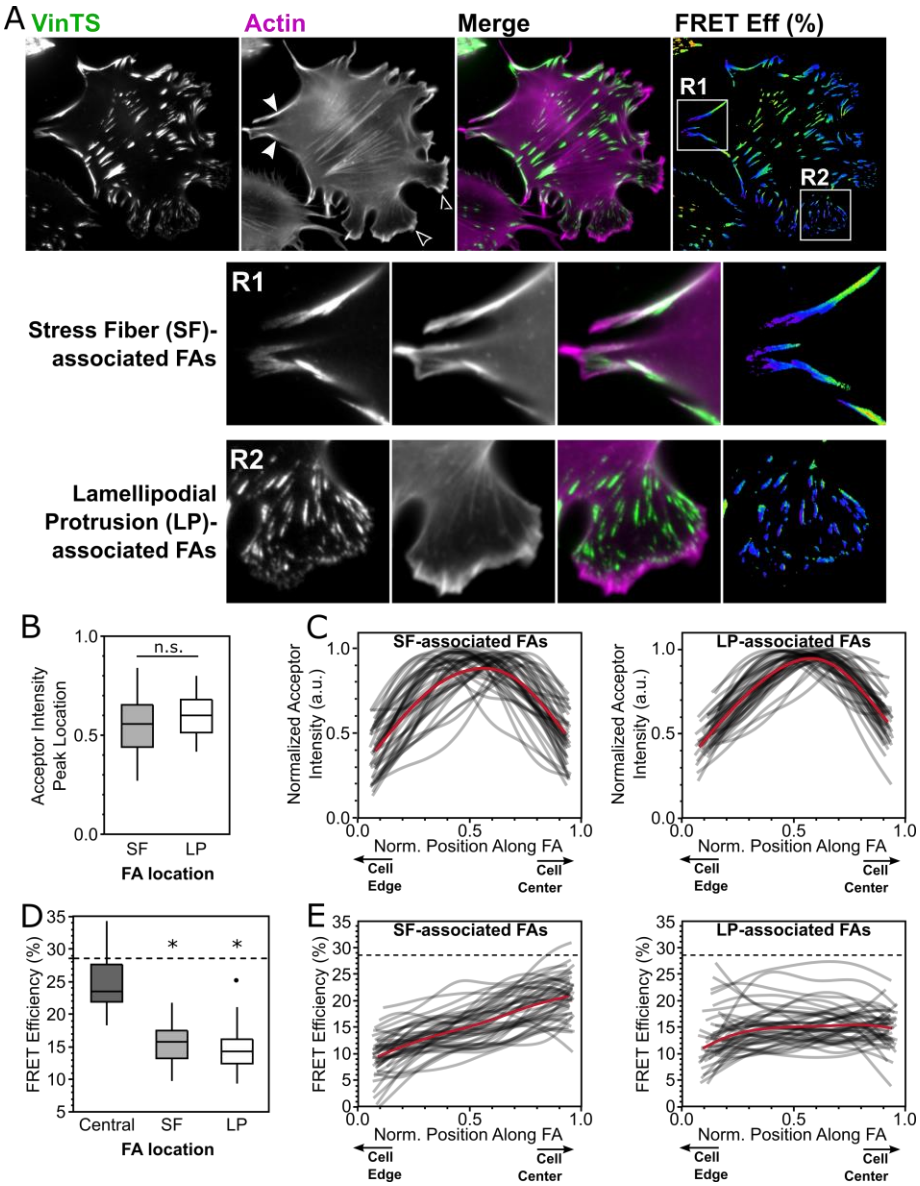

Figure 4.1: Spatial gradients in vinculin loading are associated with specific actomyosin structures. (A) Representative image of VinTS-MEFs fixed and stained with phalloidin-647 showing vinculin tension high in the cell periphery in FAs connected to both actin stress fibers (R1) and in lamellipodial protrusions (R2). (B-E) Line scan profiles of acceptor intensity (B, C) and FRET efficiency (D, E) along user-identified SF- or LP-associated FAs; n = 9 cells and n = 45 FAs from three independent experiments. (B) Quantification of acceptor intensity peak location along length-normalized FAs; n.s. not significant, Student's t-test, two-tailed, assuming unequal variances. (C) Distribution of VinTS in SF- and LP-associated FAs in terms of normalized acceptor intensity. (D) Average FRET efficiency in user-identified SF and LP FAs as compared to a central population; * $p < 0.05$, determined by ANOVA and Dunnett's test. (E) Distribution of vinculin loads in SF- and LP-associated FAs; dashed lines indicate zero load.

4.3.2 Automated quantification of the magnitude of tension gradients

Since identification and line scanning of SF- and LP-associated FAs is relatively low-throughput and relies on the user to identify SFs and LPs, we first sought a means to automate key analyses. The object-based segmentation algorithms utilized by our lab lent themselves well to the task [133, 202]. For illustrative purposes, we have depicted representative user-drawn line scans of acceptor intensity and FRET efficiency for single SF-associated and LP-associated FAs and subsequent gradient strength calculations (Figure 4.2, see Chapter 4.2.9 for details). Briefly, for every FA object identified by a water algorithm [203], the X and Y coordinates of two centroids were computed to sub-pixel precision: (1) a geometric centroid defined by the FA mask and (2) a $FRET^{-1}$-weighted centroid, which is shifted towards areas of higher tension (lower FRET). Using the cell centroid as a frame of reference, the relative distance between these two centroids, normalized to FA length, provided an unbiased, automated measurement of gradient strength (Figure 4.2). Positive values indicate that the $FRET^{-1}$-weighted centroid is shifted distal to the cell body relative to the geometric centroid, as is generally the case for the SF-associated FAs that exhibit strong gradients in vinculin loading profiles.

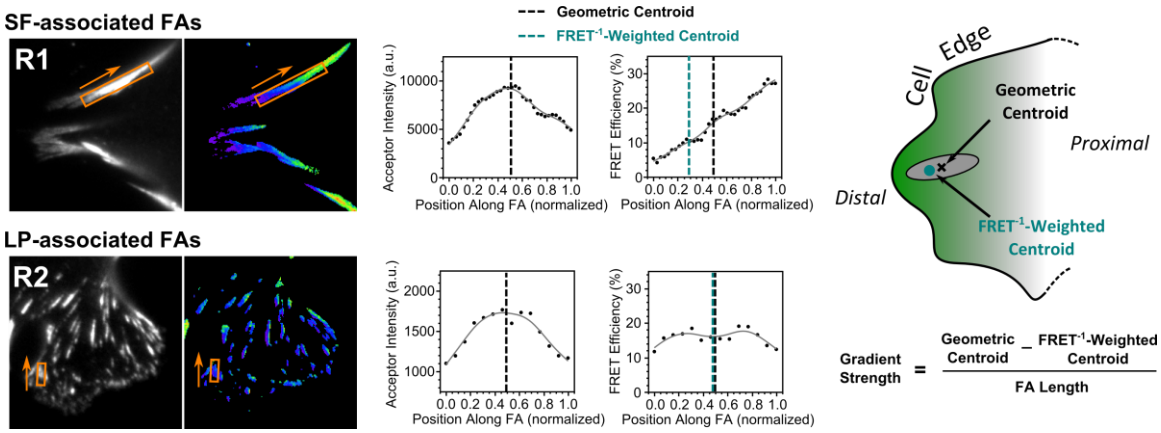

Figure 4.2: Schematic depicting automated spatial tension gradient measurements. Representative manually-drawn line scans along SF- and LP-associated FAs (A) show the emergence of gradient loading of vinculin only in FAs connected to SFs (B). Automated image analysis algorithms capture the same information in a single measurement we refer to as "Gradient Strength", which describes the relative shift in FRET^{-1}-weighted centroid away from the geometric centroid of individual FAs (B, C).

4.3.3 Gradient loading of vinculin coincides with SF formation during cell spreading

Having established an automated method to detect changes in vinculin's spatial loading profile, we next sought to better define the temporal dynamics involved in the establishment of these tension asymmetries. Towards this end, we examined the evolution of vinculin tension and tension gradients at various time points during the cell spreading process. Given the apparent relationship between SF formation and vinculin tension gradients, we hypothesized that tension gradients would be absent early in the cell spreading process, when Rac-mediated protrusion-based mechanisms are active , but gradually strengthen as SFs mature due to RhoA-dependent pathways [83, 89, 236]. Indeed, visualization of FRET in masked FAs (Figure 4.3A) and quantification of the average FRET^{-1}-weighted centroid in peripheral FAs showed a rapid strengthening of

tension gradient that coincided with the formation of SFs (Figure 4.3B). Interestingly, despite the differences in actin architectures and vinculin tension gradients, vinculin tension levels remained high throughout the cell spreading process (Figure 4.3C), suggesting vinculin's early involvement and continued role in force transmission through both protrusion and contractile phases of spreading. Together, these findings indicate that the vinculin tension gradients vary in time and their emergence is correlated with the emergence of SFs in spreading cells.

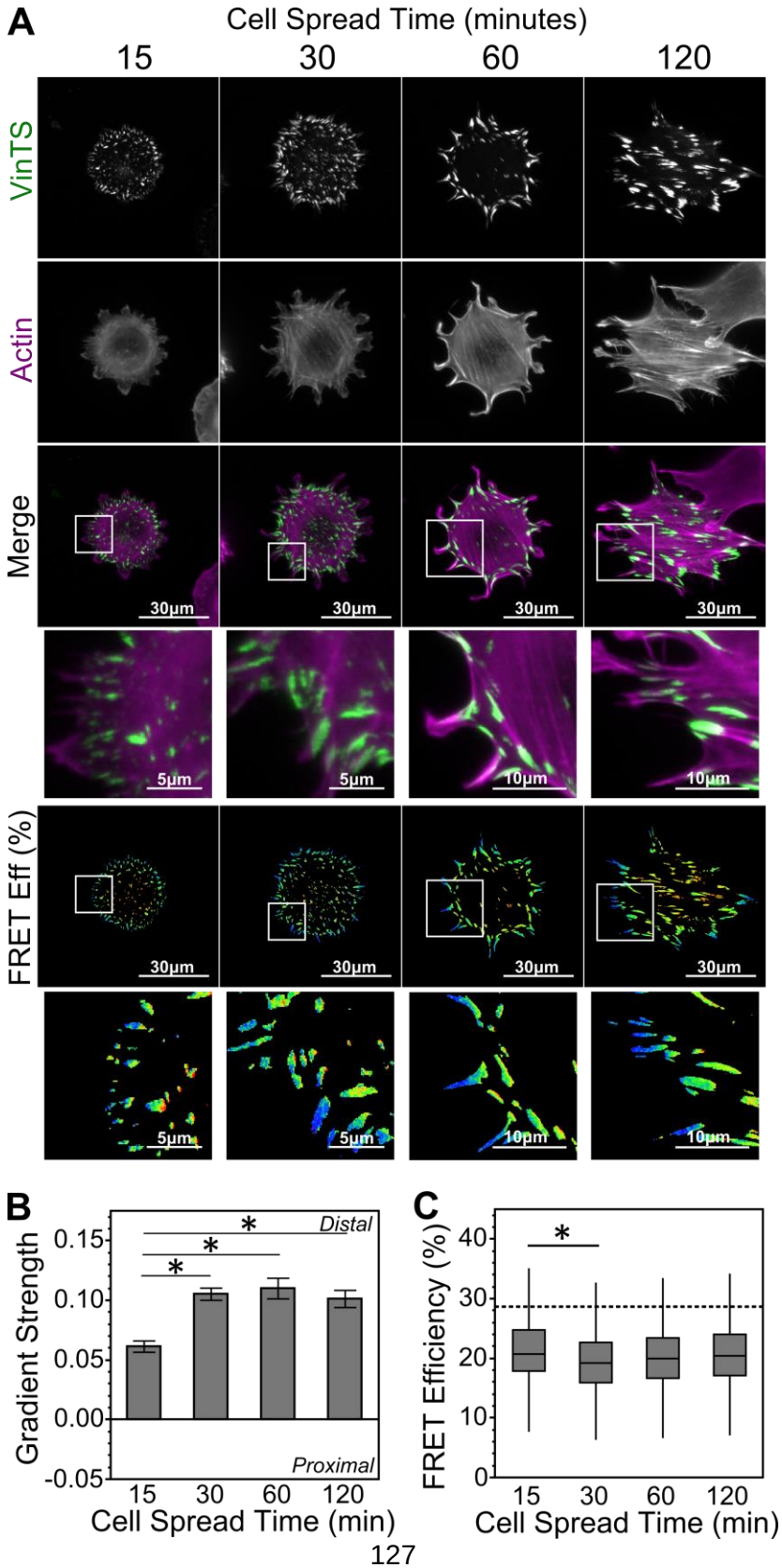
A
Cell Spread Time (minutes)
15
30
60
120
VinTS
Actin
Merge
FRET Eff (%)
30µm
5µm
10µm
B
Gradient Strength
0.15
0.10
0.05
0.00
-0.05
Distal
Proximal
*
15
30
60
120
Cell Spread Time (min)
C
FRET Efficiency (%)
40
30
20
10
0
*
15
30
60
120
Cell Spread Time (min)

Figure 4.3: Emergence of gradient loading of vinculin during the cell spreading process. (A) Representative images of VinTS MEFs spread for 15, 30, 60 or 120 minutes then fixed and stained with phalloidin-647. (B) Quantification of gradient strength in peripheral FAs at each spreading timepoint. (C) Box-and-whisker plot of cell-averaged FRET efficiencies in spreading cells; dashed line indicates zero load. Data represents n = 52, 71, 83, and 80 cells from 15, 30, 60, and 120 minute timepoints, respectively; pooled from 3 independent experiments; * $p < 0.05$ as determined by ANOVA and Tukey's HSD.

4.3.4 Vinculin loading profiles can be altered by RhoGTPase activation

Evidence from both fully spread and actively spreading cells indicated the involvement of the Rho-GTPases RhoA and Rac1 in the formation and maintenance of gradient loading profiles. To more directly test this hypothesis, we examined how expression of constitutively active forms of RhoA (V14-Rho) and Rac1 (V12-Rac) influenced the establishment of vinculin tension gradients in peripheral FAs (Figure 4.4). FAs in mock-transfected cells were primarily associated with SFs and thus exhibited strong vinculin tension gradients. Surprisingly, despite the visible increase in SF number and thickness, transient expression of V14-Rho did not significantly affect the strength of these tension gradients in peripheral FAs (Figure 4.4B), although tension across vinculin did increase from baseline (Figure 4.4C). In contrast, expression of V12-Rac induced LPs throughout the cell periphery that was accompanied by a significant reduction in the vinculin tension gradient (Figure 4.4A, B). While SF- and LP-associated FAs showed marked differences in spatial loading profile, expression of V12-Rac increased molecular tension across vinculin to levels indistinguishable from those of V14-Rho (Figure 4.4C). Taken together, these results confirm the involvement of RhoA and Rac1 in the

formation and maintenance of vinculin's spatial loading profile and demonstrate that molecular loading of vinculin and vinculin's spatial loading profile are separable. Furthermore, it clearly demonstrates that vinculin can be substantially loaded by actomyosin structures associated with Rac1 as well as RhoA.

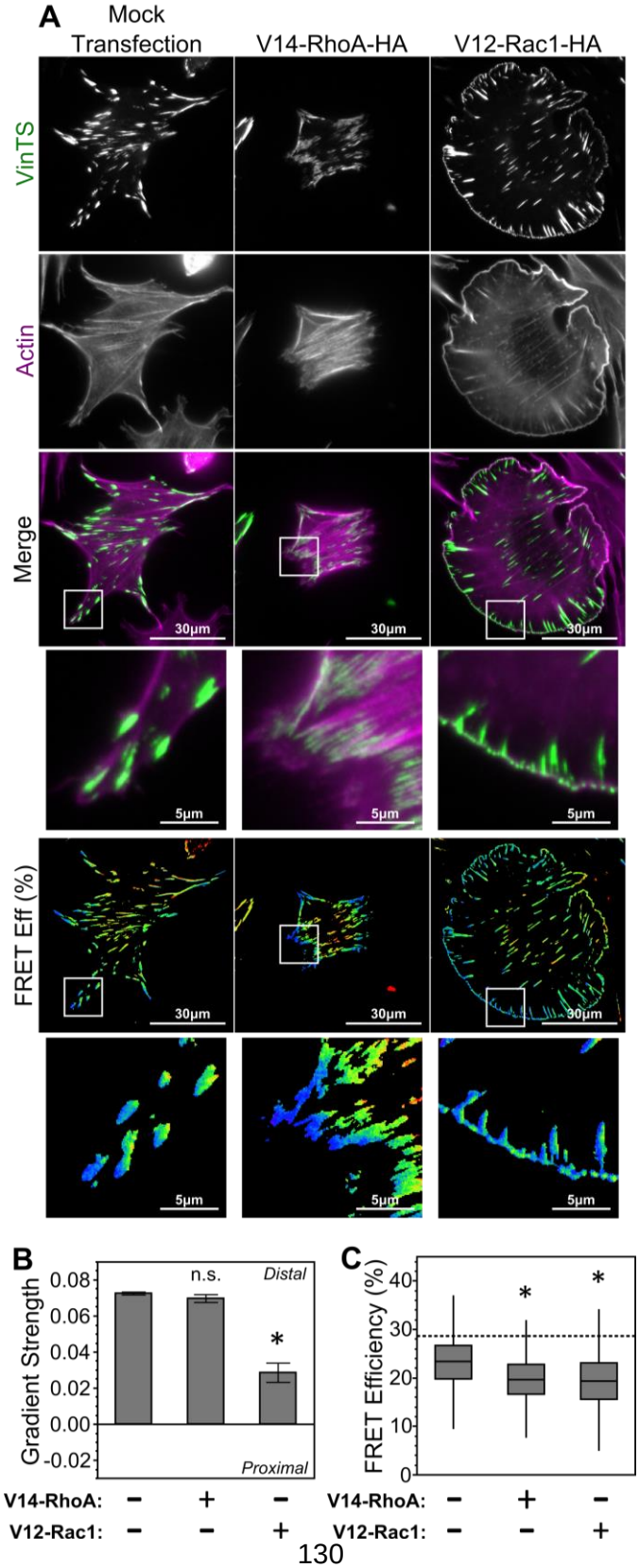
A
Mock Transfection
V14-RhoA-HA
V12-Rac1-HA
VinTS
Actin
Merge
FRET Eff (%)
30μm
5μm
B
Gradient Strength
0.08
0.06
0.04
0.02
0.00
-0.02
n.s.
*
Distal
Proximal
C
FRET Efficiency (%)
40
30
20
10
0
*
*
V14-RhoA: − + −
V12-Rac1: − − +
V14-RhoA: − + −
V12-Rac1: − − +

Figure 4.4: Constitutively-active forms of RhoA and Rac1 impact vinculin spatial loading profile. (A) Representative images of VinTS MEFs either mock transfected or transiently expressing constitutively-active forms of Rac1 (V12) or RhoA (V14), fixed and stained with phalloidin-647. (B) Quantification of gradient strength in peripheral FAs with each treatment (C) Box-and-whisker plot of cell-averaged FRET efficiencies; dashed line indicates zero load. Data represents n = 84, 63, and 64 cells for mock-transfected, V14-Rho and V12-Rac groups, respectively; pooled from 3 independent experiments; * $p < 0.05$ as determined by ANOVA and Dunnett's test.

4.3.5 Talin and actin modulate vinculin loading and spatial loading profile

At a molecular level, vinculin loading is primarily mediated through interactions with talin through vinculin's head domain [160] and actin in vinculin's tail domain [99]. Based on evidence for the cooperative role that these two binding interactions has in vinculin activation [172], we hypothesized that a similar cooperative mechanism involving both talin and actin would be required for both loading vinculin and establishment of vinculin tension gradients. To test this hypothesis and more precisely probe the involvement of these molecular players in these processes, we created versions of VinTS containing point mutations that disrupt binding to talin in the head domain (A50I) [243] and actin in the tail domain (I997A) [99]. Cells stably expressing either mutant form of VinTS spread and form FAs in a manner consistent with previous observations by our lab and other groups [99]. Disruption of either talin binding (A50I-VinTS) or actin binding (VinTS-I997A) dramatically reduced the strength of the tension gradient across vinculin in individual FAs, despite the presence of actin SFs (Figure 4.5A, B). However, actin binding and talin binding differentially affect the magnitude of the loads borne by vinculin. Specifically, cells expressing VinTS-I997A showed complete

reduction in tension to an unloaded state (Figure 4.5C). one would not expect significant variation in tension across individual FAs. In contrast, despite the reduction in vinculin tension gradient in VinTS-A50I FAs, average vinculin tension levels remained high (numbers). Similar to the RhoA vs Rac1 modulation of vinculin tension and tension gradients, molecular point mutation studies indicate that these two variables are separable. Whereas vinculin-actin interactions are required for both vinculin loading and vinculin tension gradients, vinculin-talin interactions are dispensable for vinculin loading, but required for the establishment of RhoA-mediated vinculin tension gradients.

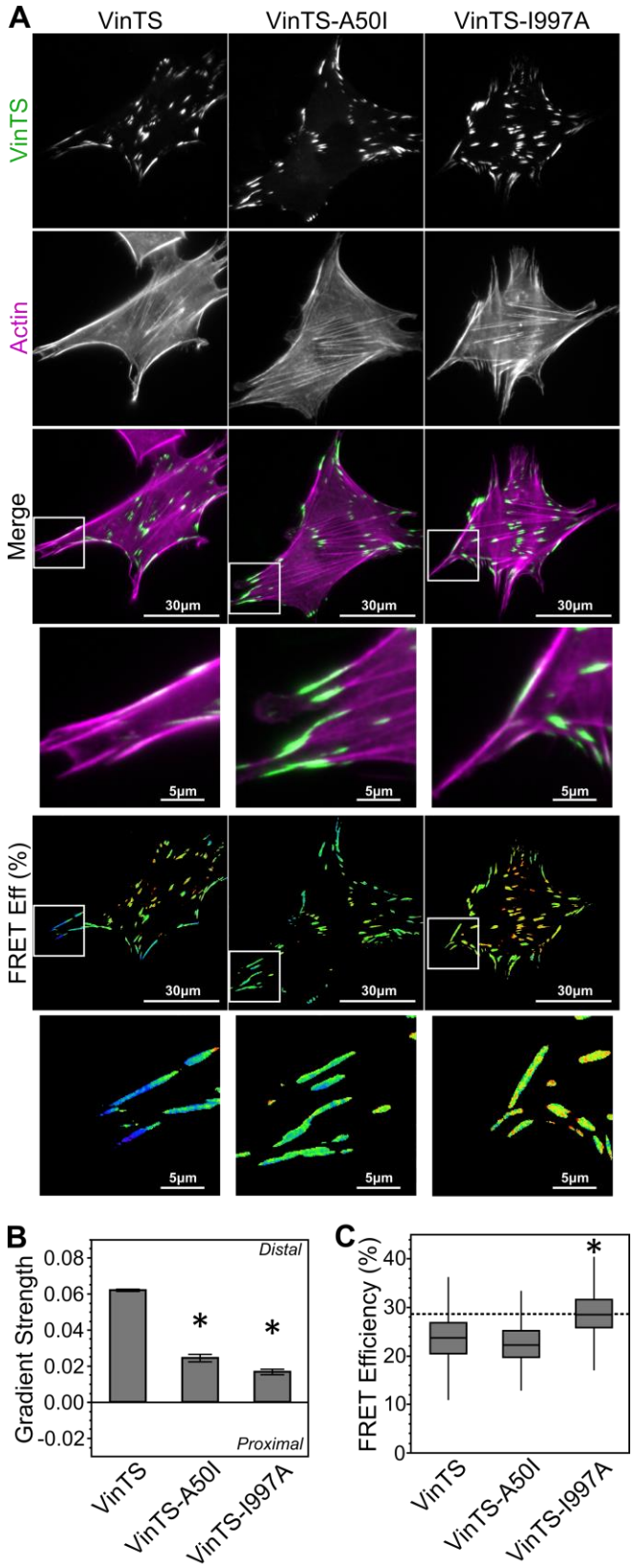
A
VinTS
VinTS-A50I
VinTS-I997A
VinTS
Actin
Merge
30μm
5μm
FRET Eff (%)
B
Gradient Strength
Distal
Proximal
0.08
0.06
0.04
0.02
0.00
-0.02
*
*
VinTS
VinTS-A50I
VinTS-I997A
C
FRET Efficiency (%)
40
30
20
10
0
*
VinTS
VinTS-A50I
VinTS-I997A

Figure 4.5: Vinculin's interactions with talin are dispensable for vinculin loading but required for gradient loading profile. (A) Representative images of vinculin -/- MEFs stably expressing VinTS, VinTS-A50I (talin-binding mutant) or VinTS-I997A (actin binding mutant), fixed and stained with phalloidin-647. (B) Quantification of gradient strength in peripheral FAs for each tension sensor construct. (C) Box-and-whisker plot of cell-averaged FRET efficiencies; dashed line indicates zero load. Data represents n = 69, 33, and 35 cells for cells expressing VinTS, VinTS-A50I, and VinTS-I997A, respectively; pooled from 2 independent experiments; * $p < 0.05$ as determined by ANOVA and Dunnett's test.

4.4 Discussion

4.4.1 Role of talin in establishment of vinculin tension gradients

One of the primary goals of this chapter was to provide a more comprehensive investigation into the origins of the gradient mechanical loading profiles observed by us (in Chapter 3) and others [101, 229, 230]. By tracking cells through mechanical processes like spreading and initiating changes in cytoskeletal architecture through the RhoGTPases RhoA and Rac1, we found a strong association between vinculin gradient loading and the formation of actin SFs. Interestingly, the uniformly high loads we observed in association with LPs could also be brought about by perturbation of vinculin's interactions with talin. This suggests a critical role for talin-vinculin interactions in the maintenance of gradient loading of vinculin. Talin could serve to reposition vinculin within the 3D architecture of the FA [244], enabling or inhibiting vinculin's ability to bind actin, which have been shown to be highly orientation dependent [178]. However, the reverse is also true, as vinculin plays a critical role in loading and stabilizing talin in FAs [35, 245]. The results presented in this chapter

provide important information as to the talin-dependent mechanical engagement of vinculin that could factor into these studies on rigidity sensing.

4.4.2 Vinculin is mechanically engaged in both LP- and SF-associated FAs

Besides the origins of gradient loading, we discovered that static loads from SFs as well as frictional forces from LPs serve to load vinculin. These findings support vinculin's well-established role in generating traction forces [173, 176, 177] and engaging with actin retrograde flow [99]. Since our observations indicate that vinculin is engaged in a variety of mechanical contexts, vinculin might be a preferred means by which cells gauge matrix stiffness or mechanically sense their microenvironment. Additionally, while talin interactions are required for development of sub-FA gradients in tension, vinculin tension sensors unable to bind talin still report significant loads. This talin-independent loading of vinculin could represent an alternative force transmission pathway that is engaged in different physical contexts.

4.4.3 New information for models of FA force-dependent growth

Attempts to understand FA force sensitivity and force-dependent growth have led to the development of molecular models that capture certain aspects of these processes. There are many simple models that consider a general protein within FAs that serves to transmit forces between the ECM and the actin cytoskeleton, in turn modulating FA growth, translocation, and disassembly [246-249]. Thus far, updates to these models have primarily focused on the details of force-sensitive kinetics of FA

plaque proteins [250], or propose molecular mechanisms underlying rigidity sensing [251]. While all these models sufficiently describe the phenomenon of FA strengthening in the presence of force they make distinct predictions about the distribution of loads within FAs as well as the most critical molecular players. Thus, the molecular-scale measurements of vinculin loading in this study should enable refinement and fine-tuning of these models and potentially shed light on mechanisms underlying more complex processes like rigidity sensing and cell migration.

4.5 Summary

The mechanical interactions between a cell and its local microenvironment are largely mediated by FAs, which bridge the gap between the force-generating actomysosin cytoskeleton and the ECM. Traditionally, cellular force generation has been associated with the formation of large contractile actin stress fibers (SFs). However, more recent studies have observed large forces produced behind lamellipodial protrusions (LPs) in lamellar actin networks, indicating actin retrograde flow is a different, but equally powerful source of cellular forces. In this chapter, we investigated the extent to which these two distinct actin structures transmit forces to vinculin at the subcellular and sub-FA level. We found, almost universally, high vinculin loads in association with either actin structure. Only mutating the actin binding site in vinculin's tail domain significantly reduced loading of vinculin. In contrast, we observed a unique sub-FA loading profile for vinculin that was associated only with SFs and was abrogated

by perturbing vinculin's interactions with talin. Overall, this work highlights that vinculin loads and vinculin spatial loading profiles are differentially regulated in cells and might therefore serve distinct purposes in FA and cellular mechanosensitivity (Further investigate the implications for these loads in Chapter 5).

5 Detection of Force-Dependent Protein-Protein Interactions in Focal Adhesions

5.1 Introduction

The molecular diversity of FAs as well as their positioning between the ECM and the force-generating cytoskeleton enables the potent regulation of many mechanosensitive functions in cells. Ultimately, bulk mechanical loads are borne by specific protein linkages, as has been demonstrated using genetically-encoded molecular tension sensors for the FA proteins talin, vinculin, and α-actinin, as well as extracellular sensors of integrin tension [155, 190, 193]. Such direct visualization of protein loading provides a powerful indication of "hotspots" of mechanosensitive signaling. However, the mechanisms by which molecular loads lead to the activation of biochemical signaling pathways are poorly understood and experimentally challenging to elucidate.

Traditionally, mechanosensitive signaling mechanisms are thought to involve the formation of novel force-dependent protein complexes, which facilitate downstream reinforcement or signaling events. Prominent examples include talin stretch causing vinculin recruitment [18, 235], the tension-dependent p130Cas phosphorylation by Src family kinases [19], as well as more recent demonstrations of tension sensitive Filamin/FilGAP [56] and a novel role for actinin in integrin binding and adhesion maturation [252]. While these and other studies have highlighted the important role of molecular force in the formation of protein-protein interactions (PPIs), such demonstrations have largely been limited to tightly-controlled in vitro environments.

Furthermore, force-sensitive PPIs have mostly been identified for isolated pairs of purified proteins. Discovery-based technologies such as mass-spectrometry, have provided us with valuable information as to the molecular diversity of FAs [75], but are not designed to detect force-sensitive PPIs that are likely crucial to mechanosensitive signaling. While critical first steps, a listing of components of the FA [75] and evidence for molecular interactions in vitro [18, 19] have not provided full realizations of mechanotransduction processes in cells. Further progress is needed to describe and understand the force-sensitive scaffolding and signaling events occurring within FAs in intact cells and tissues.

In this chapter, we address this need through the development of an imaging-based technique termed fluorescence force co-localization (FFC). Broadly, this technique combines imaging of a FRET-based tension sensor with standard fluorescence-based detection of other proteins of interest. Thus, experiments provide valuable information on the co-localization of proteins to areas of high molecular tension. We first investigated the extent to which such data would be sensitive to genuine force-sensitive PPIs *in silico* using stochastic simulations of force-dependent (and force-independent) protein recruitment to FAs. These simulated data motivated the development of robust analysis techniques to visualize (through ratiometric images) and summarize (through a metric termed Recruitment Index), the molecular enrichment of proteins to areas of high force. Based on the importance of vinculin in mediating FA and cellular mechanosensitivity (Chapter 2.5), we applied FFC techniques to investigate vinculin

tension-dependent signaling mechanisms in FAs. In favor of a screen-based approach and to avoid over-expression artifacts, we used standard IF-based detection methods to visualize the localization of 20 core FA proteins to areas of high vinculin tension. Initial FFC experiments yielded numerous positive hits, indicating many key FA proteins are enriched in areas of high vinculin tension. Through two additional measurements, we were able to isolate a vinculin tension-sensitive signaling node comprised of 5 proteins: FAK/α-actinin/VASP/migfilin/zyxin. Further investigation into these top candidates revealed that migfilin localization to FAs was particularly sensitive to vinculin tension and that the vinculin tension-dependent recruitment of migfilin constituted a genuine force-dependent PPI. Together these studies (1) establish a methodology to detect force-sensitive PPIs in subcellular structures and (2) reveal not only a novel vinculin binding partner in migfilin, but also reveal a predominantly vinculin tension-dependent regulation important in this interaction.

5.2 Methods

5.2.1 Cell culture

Mouse embryonic fibroblasts (MEFs) from littermate embryos of mice carrying a vinculin null allele that lacks vinculin exon 3 (Vin-/- MEFs), along with wild-type littermate controls (WT MEFs), were generously provided by Dr. Ben Fabry [183]. Vin-/- MEFs were stably modified with a Forster Resonance Energy Transfer (FRET)-based vinculin tension sensor (VinTS MEFs) or a tension-insensitive control sensor (VinTS-

I997A MEFs) using lentiviral transduction methods as described in Chapter 4.2.3. All MEFs were maintained in high-glucose Dulbecco's Modified Eagle's Medium (D6429, Sigma Aldrich) supplemented with 10% fetal bovine serum (HyClone), non-essential amino acids (Life Technologies), and Antibiotic Antimycotic solution (Sigma Aldrich). HEK293-T cells, used for viral production, were maintained in high-glucose Dulbecco's Modified Eagle's Medium with L-glutamine and sodium bicarbonate (D5796, Sigma Aldrich) supplemented with 10% fetal bovine serum (HyClone) and Antibiotic Antimycotic solution (Sigma Aldrich).

5.2.2 Stable expression of VinTS constructs

Viral vectors containing VinTS and VinTS-I997A were constructed as described in Chapter 4.2.2. Viral production in HEK293-T cells, transduction of Vin-/- MEFs with various tension sensor constructs, and subsequent verification of endogenous expression were performed as described in Chapters 4.2.3. and 4.2.4.

5.2.3 Immunofluorescence and proximity ligation assay

Immunofluorescence staining of VinTS and VinTS-I997A MEFs was performed as described in Chapter 4.2.6 using primary antibodies outlined in Table 5.1 and either donkey anti-mouse AlexaFluor-647 (Life Technologies, A31571) or donkey anti-rabbit AlexaFluor-647 (Life Technologies, A31573) secondary antibodies.

Proximity ligation assays were conducted using the Duolink® In Situ Red Starter Kit Mouse/Rabbit (Sigma Aldrich) according to the manufactures guidelines. PLA

antibody pairs included mouse anti-Vinculin (Sigma Aldrich, V9131, 1:500) with rabbit anti-vinculin (Abcam, ab73412, 1:400) and mouse anti-vinculin (Sigma Aldrich, V9131, 1:500) with rabbit anti-migfilin (Novus Biologicals, NBP1-86665). All PLA experiments were done in parallel with negative controls that involved primary incubation steps with only a single primary antibody.

Table 5.1: List of antibodies used in FFC screen

Gene ID	Common Name	Company	Catalog Number	Dilution
ACTN4	Actinin-α4	Abcam	ab108198	1:250
PTK2	FAK	BD Biosciences	610088	1:100
PTK2_pY397	FAK (pY397)	Life Technologies	44625G	1:50
PTK2_pY861	FAK (pY861)	Life Technologies	44626G	1:100
PTK2_pY925	FAK (pY925)	Cell Signaling	3284S	1:100
FHL2	FHL2	Sigma Aldrich	HPA006028	1:100
TGFB1I1	HIC5	BD Biosciences	611165	1:300
ILK	ILK	Millipore	04_1149	1:200
ITGA5	Integrin-α5	Millipore	AB1928	1:1000
LPP	LPP	Cell Signaling	3389S	1:200
FBLIM1	Migfilin	Novus Biologicals	NBP1_86665	1:200
PARVA	α-Parvin	Thermo Fisher	PA5_17185	1:300
PXN	Paxillin	Thermo Fisher	AHO0492	1:250
PXN_pY31	Paxillin (pY31)	Abcam	ab32115	1:250
PXN_pY118	Paxillin (pY118)	Cell Signaling	2541S	1:100
LIMS1	PINCH1	Abcam	ab108609	1:100
n/a	pY	Cell Signaling	9411S	1:1000
TLN1	Talin	Sigma Aldrich	T3287	1:300
VASP	VASP	Cell Signaling	3132S	1:100
VASP_pS157	VASP (pS157)	Abcam	ab47268	1:100
VCL	Vinculin	Sigma Aldrich	V9131	1:500
ZYX	Zyxin	*Gift from Dr. Mary Beckerle		1:600

5.2.4 Microscopy and FRET imaging

Samples were imaged at 60x magnification on the microscope system described in Chapter 3.2.3. FRET imaging was performed as described in Chapter 3.2.3 using combinations of the mTFP1 excitation/emission filters and the Venus excitation/emission

filters. Fluorescence imaging of WT and Vin-/- MEFs was performed using the FITC and Cy5 excitation and emission filters from the DA/FI/TR/Cy5-4X4 M-C Brightline Sedat filter set (Semrock) with exposure times of 500ms in FITC and 1000 ms in Cy5.

5.2.5 FRET efficiency calculations

Calculation of FRET efficiency by sensitized emission and subsequent identification and quantification of FAs and cells were performed as described in Chapters 3.2.4 and 3.2.5.

5.2.6 Simulations of FFC data

Overview

The goal of fluorescence-force co-localization (FFC) is to detect force-sensitive protein-protein interactions in subcellular structures such as FAs. To do so, this technique combines FRET-based measurements of molecular tension across one protein and correlates them with the localization of other molecular species. However, as we describe in Chapter 5.3, FFC data can be visualized and interpreted in a number of ways. Additionally, other mechanisms of protein recruitment are undoubtedly active within a cell that could lead to false positives or false negatives in FFC measurements. To gain intuition as to how to analyze, visualize, and quantify FFC data and examine the extent to which it can be used to infer information about force-dependent interactions in FAs, we examined simulated FFC data in a controlled in silico setting. The following sections

describe the general structure of these simulations, the inputs and outputs from the model, as well as assumptions and limitations to the simulated FFC data.

Model Structure

Simulations of fluorescence-force co-localization (FFC) data were written in MATLAB (Mathworks). These simulations involve the stochastic accumulation of three molecules, X, Y, and Z, to binding sites in 100 FAs in a single cell. In the context of our FFC experiments X represents the vinculin tension sensor, for which we collect information on its localization (acceptor intensity, proportional to sensor concentration) as well as tension (inversely proportional to FRET); Z represents the IF-labeled protein-of-interest, for which we collect only information on localization (IF signal); Y represents some other FA component for which we have no information on either force or localization. The accumulation of X, Y, and Z to FA structures through time was simulated as a Markov chain dictated by user-input probabilities of intermolecular interactions as well as interactions with FA binding sites. We defined a simple scenario in which X and Y accumulations are independent and mediated by only FA binding sites through binding and unbinding probabilities $P_{X,on}$, $P_{Y,on}$, $P_{X,off}$, and $P_{Y,off}$. In contrast, the accumulation of Z to FA structures is entirely dependent on X and Y. Z is recruited by X or Y via force-independent ($P_Z(X)$ and $P_Z(Y)$, respectively) or force-dependent ($P_Z(F_X)$ and $P_Z(F_Y)$, respectively) interactions, where F_X and F_Y are the forces across individual X and Y molecules, respectively. Note, for simplicity we simulated permanent X-Z and Y-Z interactions, thus the release of Z is dependent upon X and Y unbinding probabilities

$P_{X,off}$ and $P_{Y,off}$. Simulations were run for t = 200 time-steps and observed to reach equilibrium at t < 50 for a wide range of input parameters. At t = 200, the number of X and Z molecules as well as F_X were recorded and written to a text file. These three values are analogous to the real FFC data acquired in an experiment: (1) X = [VinTS] = VinTS acceptor intensity, (2) F_X = molecular tension = $FRET^{-1}$ reported by VinTS, and (3) Z = [protein-of-interest] = IF signal intensity.

Setting number of binding sites and forces

In addition to the user input probabilities that describe the strength of intermolecular interactions, two other key variables dictate the form of these simulations: (1) the number of binding sites assigned to each FA structure and (2) the forces assigned to individual X and Y molecules at each binding site. The number of binding sites in each of the 100 FA structures were assigned to reflect the log-normal distribution seen to govern FA size [253], with $\mu = 5$ and $\sigma = 1$. However, since there is no general agreement as to the functional form of force distributions borne by FA molecules, we assigned $\langle F_X \rangle$ for each FA based on our own observed distributions of vinculin forces in FAs, which have a $\mu = 1.6$ and $\sigma = 1.0$. Since we also observe a distribution of forces within individual FAs (i.e. on a pixel-by-pixel basis), we also assigned an underlying normal distribution of forces across individual X molecules according to the relationship between mean(F) and stdev(F) observed in our VinTS data. In the case that F_X and F_Y were uncorrelated, the same procedure was used to assign $\langle F_Y \rangle$ values, otherwise $F_Y = F_X$.

Functional form of force-dependent interactions

While force-independent interactions occur at some set probability, the probability of force-dependent binding events are dictated by both the input force-dependent binding probability ($P(F)_0$) and the force across the molecule (F). This relationship between the $P(F)_0$ and P(F) can take on several functional forms. We assumed an underlying linear relationship: $P(F) = F * P(F)_0$. In this way, increased force-dependent interactions will occur with both higher baseline $P(F)_0$ values (a.k.a. $P_Z(F_X)$ and $P_Z(F_Y)$ in Chapter 5.3.2) and at higher forces.

Assumptions and Limitations of the Model

The initial form of these FFC simulations include several simplifying assumptions that we discuss here. However, even with these underlying assumptions, this minimal model provided valuable insight into the interpretation of FFC data (see Chapter 5.3). Added complexity to the model could help interpret specific force-sensitive interactions for which there is evidence of some of the following effects. First, in its initial form, these FFC simulations assume single force-independent and force-dependent binding site to be present on both X and Y molecules. However, multivalent binding interactions likely occur, as has been shown between talin and vinculin molecules [18, 235]. We also considered an unlimited cytosolic pool of X, Y, and Z molecules. The limiting reagent in these simulations was the number of binding sites

present in each FA. Moreover, X, Y, and Z molecules accumulate as single molecular species, while there is evidence of pre-assembly in the cytosol for known binding partners (e.g. Vinculin-VASP or ILK-PINCH-Parvin) [254]. Also, we assume forces to linearly increase force-dependent binding probabilities, but other functional forms (step, exponential, etc.) could be considered in future simulations. Finally, we caputure all possible alternative recruitment pathways in a single "Y" molecule. Given the molecular complexity of FAs, it is likely that multiple molecular linkages and routes to FA molecule accumulation exist. Regardless, these simulations provide a robust platform from which to investigate and facilitate interpretation of FFC data.

5.2.7 Statistics

All statistical analyses, were performed using JMP Pro 12 software (SAS, Cary, NC). ANOVAs were used to determine if statistically significant differences ($p < 0.05$) were present between groups. If statistical differences were detected, Tukey's HSD post-hoc testing Bonferroni corrected for multiple comparisons, were used to assess statistical differences between individual groups.

5.3 Results

5.3.1 Stochastic simulations guide interpretation of fluorescence-force co-localization data

Fluorescence image co-localization, a technique widely utilized in the biomedical sciences, infers functional interactions between proteins based on correlations in their intensities. Based on this concept, we investigated the possibility that correlations between the mechanical load experienced by one protein and the localization of another protein could be used to detect potential force-dependent PPIs within mechanosensitive structures like FAs. Experimentally, this technique, which we refer to as fluorescence-force co-localization (FFC), would involve the straightforward combination of molecular tension sensors with immunofluorescence (IF)-based labeling of other molecular species. In effect, we could add a third dimension to classic co-localization methods and determine the functional relationships between two proteins as a function of force. While FFC, like traditional co-localization, could not be used to measure direct molecular interactions, it offered a powerful means to detect potential force-sensitive PPIs in intact cells.

To probe the feasibility of isolating potential force-sensitive PPIs in FAs using FFC, we developed a simple stochastic simulation of protein recruitment to FAs. Details on the construction and implementation of these simulations can be found in Chapter 5.2.6. Briefly, the model includes three molecules, X, Y, and Z, that are recruited to FAs through different mechanisms (Figure 5.1). While X and Y molecules freely associate and

disassociate from FA binding sites (Figure 5.1A), Z cannot. Instead, Z recruitment to FA structures is dependent upon either X or Y via force-independent and/or force-dependent mechanisms (Figure 5.1B, C, respectively). The strengths of interactions are defined by force-independent binding probabilities $P_Z(X)$ and $P_Z(Y)$, and force-dependent binding probabilities $P_Z(F_X)$ and $P_Z(F_Y)$. Importantly, in FFC experiments, only the localization and mechanical loading of X (i.e. vinculin tension sensor) and the localization of Z (i.e. protein of interest) can be monitored. The strength of recruitment of Z molecules by some alternative molecule Y is unknown. Y is meant to represent some alternative mechanosensitive recruitment pathway and was included in these simulations to estimate the limits of FFC.

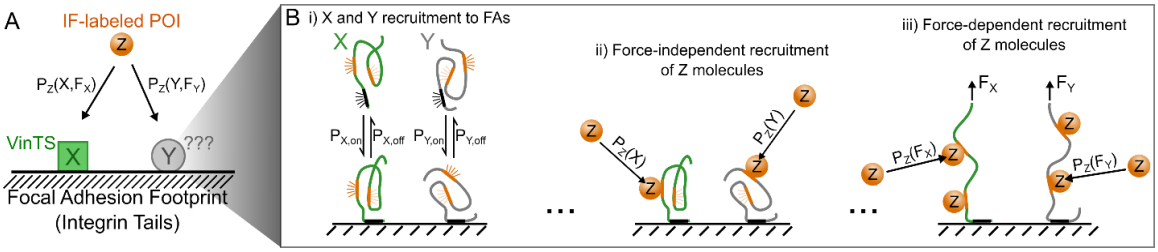

Figure 5.1: Schematic depiction of molecular FFC simulations. (A) A protein of interest, Z, can be recruited to focal adhesions via two separate pathways (X or Y). Both of these pathways, individually, recruit Z molecules via force-independent and force-dependent mechanisms ($P_Z(X, F_X)$ and $P_Z(Y, F_Y)$, where X and Y denote the force-independent contribution and F_X and F_Y denote the contribution of these molecular forces to Z recruitment. (B) Underlying events simulated include (i) binding and unbinding of X and Y molecules to the surface (conceptualized as the FA footprint or integrin tails), (ii) force-independent binding of Z to either X or Y and (iii) force-dependent binding of Z to either X or Y, which is a function of F_X and F_Y, respectively. All events occur in a stochastic manner, so the order of events depicted is arbitrary and does not impact the simulation outputs.

5.3.2 Normalization strategy to visualize force-dependent interactions in simulated data

To establish a baseline, we examined how purely force-independent and force-dependent X-Z interactions manifest as intensity correlations or force correlations. As expected, simulations of force-independent X-Z interactions of increasing strength led to the rapid evolution of intensity correlations (Figure 5.2A). No correlations between Z and F_X were observed (Figure 5.2B). Intriguingly, stronger force-dependent interactions also caused increases in intensity correlations (Figure 5.2A'), likely because both the presence of a molecule X as well as the force across that molecule (F_X) augment Z recruitment. While these intensity correlations were not surprising, they did raise concerns as to our ability to detect force-sensitive interactions in the presence of force-independent ones. Even in a purely force-dependent interaction scenario, correlations between Z and F_X only reach moderate levels around R = 0.5 (Figure 5.2B'). Moreover, adding in a moderate force-independent interaction to this scenario of $P_Z(X) = 0.5$ almost completely abrogated our correlations with force (Figure 5.2B').

Given that these underlying intensity correlations were likely hindering our ability to detect force-sensitive interactions, we next sought to determine if there was a better metric to detect force-dependent X-Z interactions. Encouragingly, a ratiometric Z/X measurement had no impact on the null result in a force-independent simulation (Figure 5.2C) and produced moderately stronger force correlations as a function of $P_Z(F_X)$ (Figure 5.2C'). Furthermore, these force correlations were much more robust to

underlying intensity correlations brought about by $P_Z(X) = 0.5$ and were detectable when $P_Z(F_X)$ was less than half of $P_Z(X)$ (Figure 5.2C'). Essentially, this ratiometric Z/X quantity allowed us to identify the molecular enrichment of Z relative to X in high-force FAs. Therefore, we choose normalized Z/X measurements in visualizing force-dependent interactions.

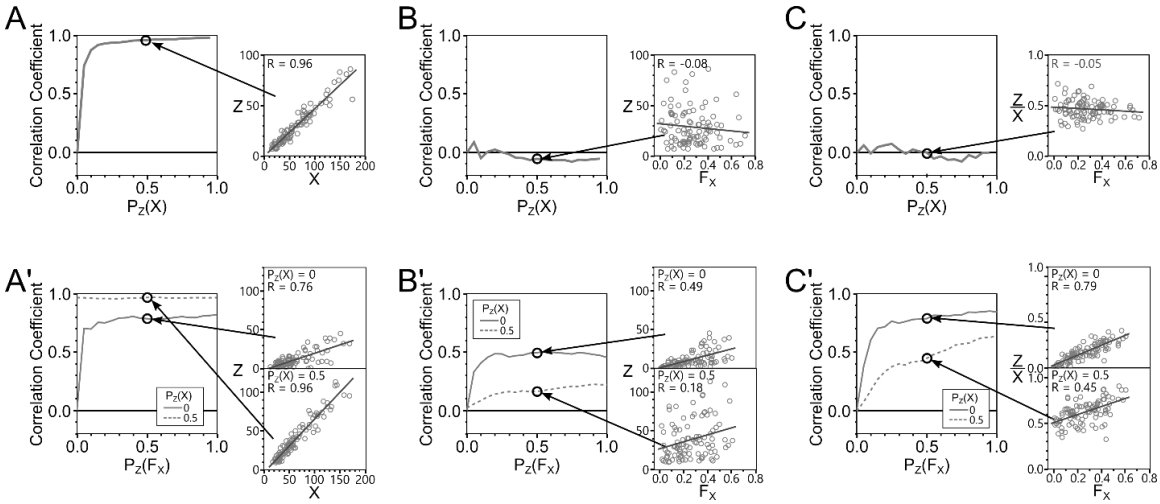

Figure 5.2: Comparison of multiple metrics to detect force-independent and force-dependent interactions in FFC simulations. (A, A') Intensity correlations between Z and X rapidly occur in the presence of stronger force-independent (A) or force-dependent (A') X-Z interactions. Scatter plots show the data from a single simulated cell at P = 0.5 intermediate binding strength. (B, B') As in (A, A') except the depicted correlations are between F_X and Z. Z localization does not correlate with force when only force-independent interactions are possible (B), and Z-F_X correlations are still low even strong force-dependent binding (B') (C, C') Alternative ratiometric measure (Z/X) does not impact the force-independent correlations (C) but enhances detection of force-dependent interactions between Z and F_X (C'), especially in the presence of moderate force-independent interactions ($P_Z(X) = 0.5$, dashed lines in A', B', C').

5.3.3 Recruitment Index describes molecular enrichment in loaded FAs

While this normalization strategy provided a simple means by which to isolate and visualize force-dependent enrichment of proteins in FFC images, correlation

analyses in general are highly sensitive to outliers. Therefore, we explored one other alternative metric to describe the relative enrichment of Z in loaded versus unloaded FAs on a cell-by-cell basis. This metric, termed recruitment index, takes the log ratio of intensities in high-force FAs relative to low-force FAs. Again however, there was a question of whether to compare absolute (Z) or normalized (Z/X) intensities. Surprisingly, use of either response variable in calculations of recruitment index yielded similar results (Figure 5.3A, B). Z/X slightly out-performed Z in a balanced $P_Z(X) = P_Z(F_X) = 0.5$ simulation, but due to the small number sensitivities inherent in a ratio of ratios, we favored recruitment index defined as:

$$RI = \log_2\left(\frac{\langle Z_{HIGH}\rangle}{\langle Z_{LOW}\rangle}\right)$$

where $\langle Z_{HIGH}\rangle$ and $\langle Z_{LOW}\rangle$ are the mean intensities of Z in high tension and low tension FAs, respectively. Furthermore, recruitment index provided reliable detection of force dependent interactions (or lack thereof) in simulations of force-dependent interactions (Figure 5.3C), force-independent interactions (Figure 5.3D), or a combination of the two (Figure 5.3E). Overall, recruitment index provides a measurement less sensitive to outliers and has intuitive physical meaning; a 2-fold increase amount of Z in loaded FAs log2(2) = 1, will be reflected the same was as a 2-fold decrease log2(0.5) = -1.

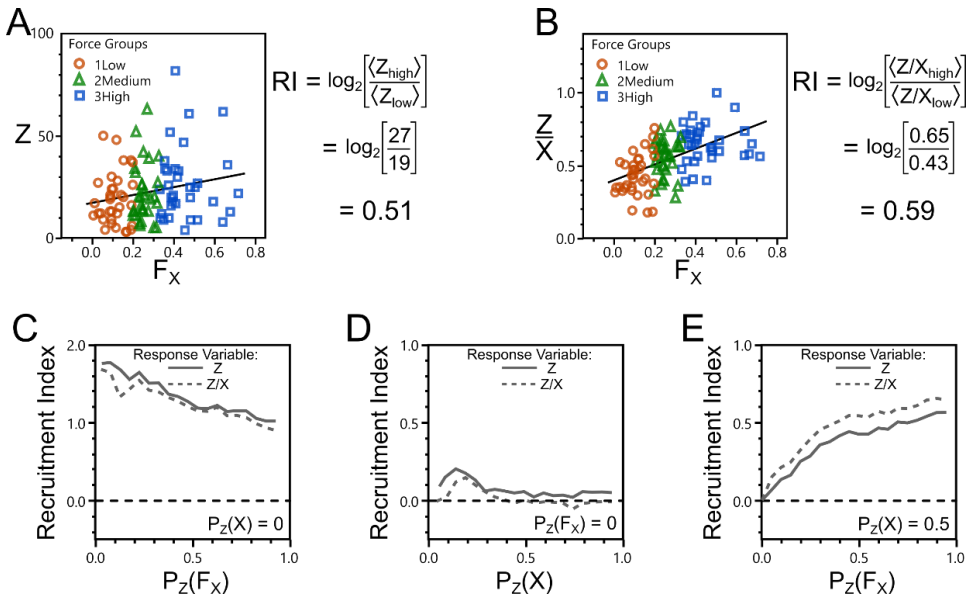

Figure 5.3: Calculating protein Recruitment Index. (A, B) Representative scatter plots of Z vs F_X (A) and ratiometric Z/X vs F_X from simulations with a balance between force-independent and force-dependent Z-X interactions ($P_Z(X) = P_Z(F_X) = 0.5$). To describe the molecular enrichment of proteins of interest (Z) in high tension FAs (high F_X), one can either use absolute intensities (Z, panel A) or ratiometric measurements (Z/X, panel B) in calculating recruitment index (RI). (C) Purely force-dependent interactions yield large values for RI regardless of the strength of force-independent interactions (x-axis, $P_Z(F_X)$. (D) In the absence of force-dependent interactions RI = 0. (E) In the presence of a constitutive force-independent X-Z interaction, RI increases proportional to the strength of the force-dependent interaction (x-axis, $P_Z(F_X)$), regardless of whether Z or Z/X is used as the response variable.

5.3.4 Simulations indicate Recruitment Index is robust to most alternative protein recruitment pathways

Finally, we examined the robustness of recruitment index measurements to protein recruitment via alternative ($P_Z(X)$) or parallel ($P_Z(Y)$, $P_Z(F_Y)$) pathways. Given a moderate force-sensitive X-Z interaction ($P_Z(F_X) = 0.5$), recruitment index was approximately 1.5. Adding in force-independent recruitment of Z by X ($P_Z(X)$) or Y ($P_Z(Y)$) caused significant decreases to RI ~ 0.5, but no further decreases even when protein recruitment was dominated by these force-independent mechanisms (Figure 5.4,

dashed lines). Additionally, in this simplified system, force-independent recruitment mechanisms alone yielded RI ~ 0, indicating false positives would not be expected using this metric (Figure 5.4, solid lines). However, considering the force-dependent recruitment of Z through the alternative pathway Y ($P_Z(F_Y)$), an underlying assumption in these simulations becomes important: are F_X and F_Y correlated or uncorrelated? In the case that F_X and F_Y are uncorrelated, $P_Z(F_Y)$ has little effect on the previous observations (Figure 5.4). However, in a situation where F_X and F_Y are highly correlated, force-dependent Y-Z interactions are easily mistaken for the force-dependent X-Z interactions and yield high RI ~ 1.5 regardless of the presence or absence of the underlying $P_Z(F_X)$ of interest. Thus, if forces borne by proteins in the mechanosensitive pathway of interest (F_X) are correlated with some alternative pathway (F_Y), then the potential for false positives exists.

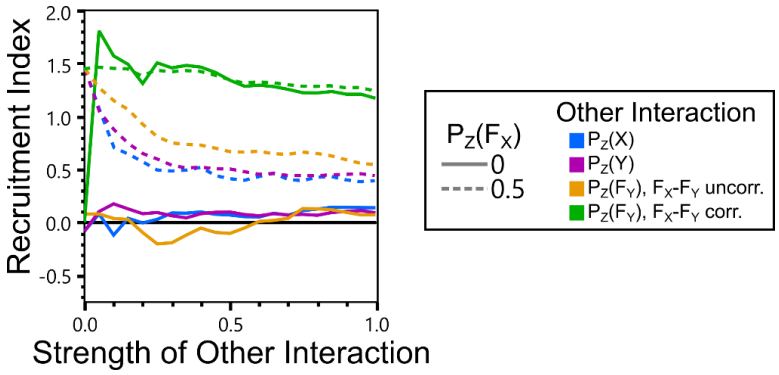

Figure 5.4: Robustness of Recruitment Index to alternative recruitment pathways. The ability to detect a force sensitive interaction (compare $P_Z(F_X) = 0$ to $P_Z(F_X) = 0.5$, solid versus dashed lines), depends on the strength of alternative recruitment of Z through Z-X force-independent interactions (blue), Z-Y force independent interactions (green), and Z-Y force-dependent interactions where forces borne by X (F_X) and Y (F_Y) are either uncorrelated (orange) or correlated (green).

In summary, we found that recruitment index enabled robust detection of force-sensitive interactions in simulated FFC data, even in the presence of (1) strong force-independent recruitment by either the measured protein (X, VinTS) or alternative recruitment pathways (Y) and (2) force-dependent recruitment through a parallel pathway Y in the limit that F_X and F_Y are uncorrelated. Together these results provided quantitative insight into the proper interpretation of FFC data, highlighting the importance of examining ratiometric changes in raw FFC data (Z/X normalization strategy), and defined recruitment index as a robust metric to concisely describe the relative enrichment of proteins in high versus low tension FAs.

5.3.5 Candidate selection for FFC screen

With a conceptual framework in place, we moved on to select candidates to include in the FFC screen for vinculin force-sensitive protein associations. Due to the tremendous molecular diversity of FAs, selection criteria were designed to restrict this list to the proteins most central to FA force transmission and mechanosensitivity (Table 5.1). First, the candidate list was restricted to the 60 proteins identified in the consensus integrin adhesome [75]. Since a number of these candidates were relatively peripheral in this network, we further narrowed the list to those proteins with 2 or more interactions with other core components or actin (34 components). Additionally, as FFC is an IF-based technique, it relies heavily on the availability of high quality antibodies to specifically label proteins at FAs. Proteins for which antibodies were commercially unavailable, or for which antibody staining yielded nonspecific or predominantly

cytosolic IF signals were also excluded from the list. Although this requirement for high-quality antibodies did restrict our screen to 14 proteins, FFC has the added advantage of enabling probing of protein phosphorylation states in addition to total protein localization. Considering this, we further expanded the candidate list to include phospho-specific antibodies against FAK (3), paxillin (2) and VASP (1). Not including positive (pY) and negative (vinculin) controls for force-sensitive associations, the final list included 20 candidates (Table 5.1).

5.3.6 Measuring vinculin force-dependent protein associations in FAs using FFC

As previously described, loads across vinculin were measured using the vinculin tension sensor (VinTS) [131] stably expressed in vinculin -/- mouse embryonic fibroblasts (MEFs). These cells, referred to as VinTS-MEFs, were plated on fibronectin-coated glass in 24-well plates. After 4 hours, cells were fixed, permeabilized, and labeled for proteins and protein phosphorylation states (see Table 5.1 for a full list of antibodies) using AlexaFluor 647 secondary antibody. Signals from the mTFP1-Venus based tension sensor and the far-red IF signal are spectrally distinct, enabling simultaneous and quantitative measurement of vinculin load (inversely proportional to FRET efficiency) and protein enrichment in FAs (Figure 5.5A).

The final FFC dataset included 348,467 FAs from 3,363 cells with at least 101 cells per candidate screened. Importantly, the amount of vinculin IF signal (vinculin antibody labeling of VinTS) was equivalent regardless of vinculin tension levels (RI = -0.02,

negative control for FFC, Figure 5.5B, C). In contrast, phospho-tyrosine (pY), which is a classic marker for force-dependent signaling [255, 256] was 2-fold enriched in FAs in which vinculin bears high loads (RI = 1.06, positive control for FFC, Figure 5.5B, C). From a global perspective, vinculin tension was associated with distinct FA composition. Both known vinculin binding partners (e.g. VASP, Figure 5.5B, C) as well as proteins with no known interactions with vinculin (e.g. migfilin) were significantly enriched in areas of high vinculin tension. Indeed, 18/20 candidates showed preferential localization to FAs in which vinculin bears high loads. Notably, members of the IPP complex of proteins (ILK, LIMS1, α-parvin) show differential enrichment, suggesting that individual proteins within this complex could act independently of vinculin load at FAs. Heterogeneity in the responses of LIM-domain containing proteins is also interesting, as LIM domains play a role in directing proteins to areas of high mechanical strain. Overall, this striking preference for many proteins to localize to areas of high vinculin tension supports the idea that, through vinculin's numerous binding partners, vinculin plays a critical role in force-dependent assembly of FAs [131, 182]. However, it was clear that more information was required to isolate probable vinculin tension-sensitive interactions.

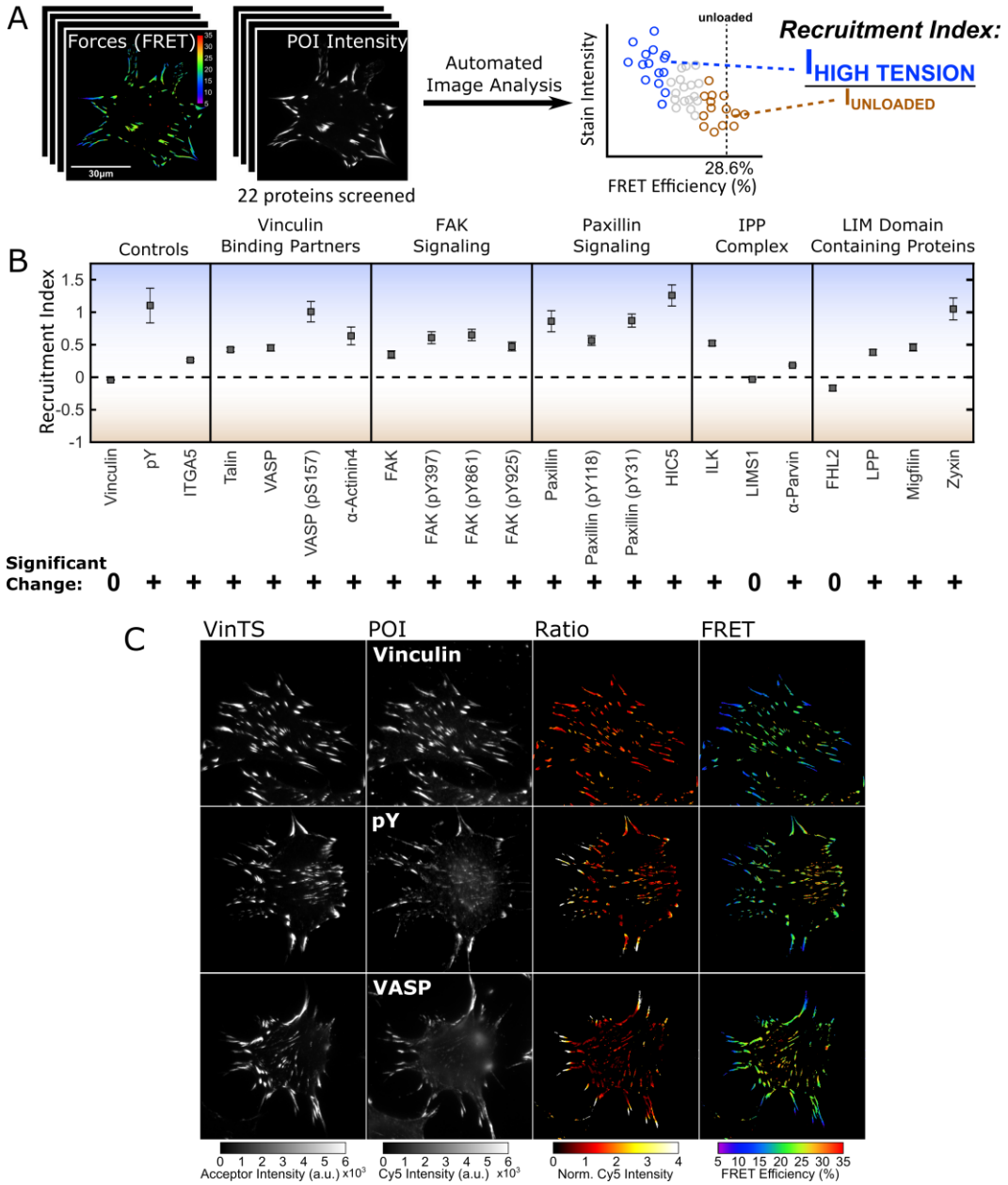

Figure 5.5: FFC reveals vinculin tension is associated with distinct molecular composition. (A) Overview of FFC technique; representative image of VinTS MEF co-stained for a protein of interest. Automated image analysis allows for the calculation of a recruitment index (see Figure 5.3 for calculations) which describes the molecular enrichment of that protein in FAs where vinculin is loaded; positive values indicate protein enrichment in FAs where vinculin bears high tension. (B) 22 proteins of interest were screened using this FFC technique; "+" indicates a significant difference and "0" indicates no significant difference from zero, as measured by one-sample t-test, two-tailed, Bonferroni corrected for multiple comparisons. (C) Representative images of FFC data for Vinculin, pY and VASP.

5.3.7 FA composition is altered in vinculin -/- cells

These initial hits in the FFC screen could represent one of three types of behaviors. In biochemical nomenclature, those proteins that associated with high tension could be downstream (i.e. respond to or are recruited to FAs by tension), upstream (i.e. play a causative role in the development of vinculin tension) or fall in to a pathway parallel to vinculin tension (i.e. coincidental correlation). To begin to distinguish between genuine vinculin tension sensitivity and other possibly parallel pathways, we measured the change in localization of these 20 proteins to FAs following vinculin knockout (Figure 5.6A). We hypothesized that proteins recruited to FAs in a vinculin tension-sensitive manner would be less abundant in FAs lacking vinculin. A quantitative comparison of the relative levels of IF staining in WT versus vinculin -/- MEFs revealed only a subset of these candidate proteins required vinculin for their recruitment to FAs (Figure 5.6B). As expected, vinculin binding partners VASP and α-actinin4 were significantly reduced in vinculin -/- MEFs. Other proteins known to interact with vinculin, but generally involved in upstream mechanisms to recruit vinculin itself (e.g. talin, paxillin, HIC5) were either unchanged or found in higher abundance in FAs lacking vinculin. Like vinculin tension sensitivity, LIM domain containing proteins show a diversity of responses to vinculin knockout. Finally, the differential regulation of FAK/pFAK and Paxillin/pPaxillin suggested upregulation of a FAK-paxillin signaling node in vinculin -/- cells as has been observed previously. Interestingly, FAK, for which there is only weak evidence of vinculin interactions, is significantly reduced in vinculin -

/- cells. This binary comparison of FA composition in WT and vinculin -/- cells provided a simple means to identify proteins likely to interact with vinculin even after the FFC screen.

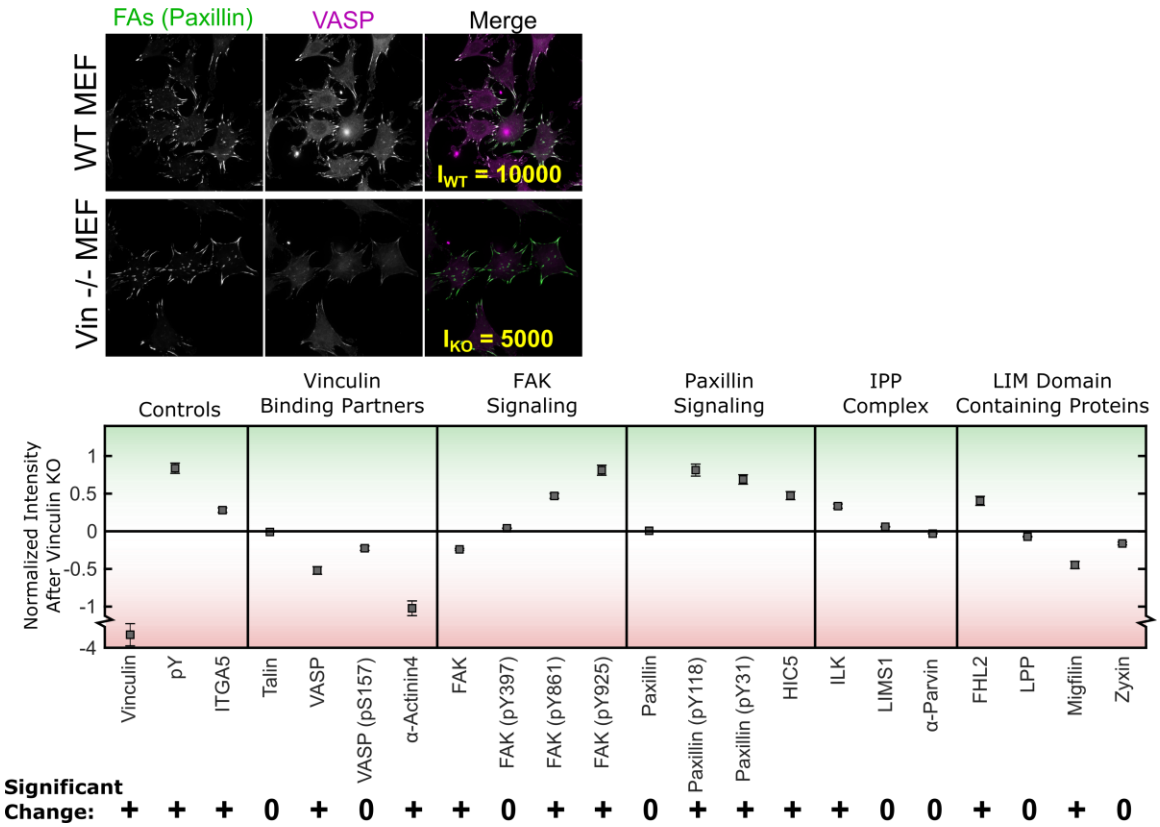

Figure 5.6: FA composition is dramatically altered in cells lacking vinculin. (A) Representative calculation of KO:WT ratio. The IF signal from VASP staining was calculated on a cell-by-cell basis in FAs identified based on a paxillin costain. The ratio of intensities in vinculin -/- (I_{KO}) compared to wild-type (I_{WT}) MEFs provides a measurement of the change in localization due to a loss of vincuilin. Taking the $\log_2$ of this ratio yields positive values if a protein is enriched following KO or negative values if a protein's localization is reduced in vinculin -/- MEFs. (B) Measurements of KO:WT ratio were made for 22 proteins of interest included in the FFC screen; "+" indicates a significant difference and "0" indicates no significant difference from zero, as measured by one-sample t-test, two-tailed, Bonferroni corrected for multiple comparisons.

5.3.8 Spatial gradients in tension also impact FA composition and signaling state

In addition to vinculin tension, the origins of molecular loading are thought to be an important variable in FA mechanosensitive signaling. Based on our results from Chapter 4, we observed two primary actin structures responsible for loading vinculin in the cell periphery, namely actin stress fibers (SFs) and lamellipodial protrusions (LPs). We hypothesized that, the ability to distinguish between these two populations of FAs could enable further clustering and therefore identification of interacting proteins. Importantly, we already developed the means to automatically detect SF- versus LP-associated FAs based on shifts in $FRET^{-1}$-weighted centroid (Chapter 4.2.9, Figure 4.3.2). Based on this classification, we were able to measure a quantity analogous to recruitment index, but that describes the preferential enrichment of proteins in SF-associated relative to LP-associated FAs (Architectural Preference, Figure 5.7A). While the resulting changes in protein localization were smaller than those brought about by vinculin tension or vinculin knockout, significant change in FA composition were associated with the two distinct spatial loading profiles of vinculin (gradient vs uniform, Figure 5.7B). Proteins known to play actin regulatory roles were predictably enriched in SF-associated FAs (VASP, α-actinin4). On the other hand, pY groups were most strongly detected in LP-associated FAs, consistent with its use as a classic marker for nascent FAs and adhesion dependent signaling mechanisms.

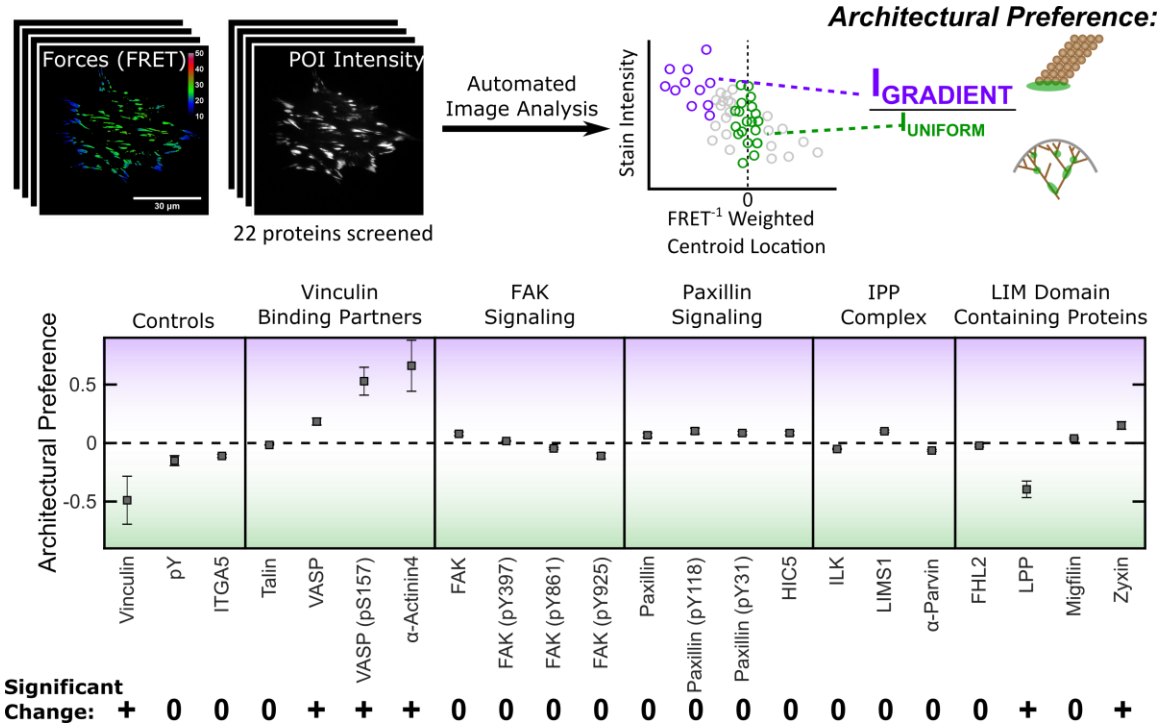

Figure 5.7: Origins of vinculin tension, as measured by spatial gradient loading profile also impact FA composition and signaling state. (A) Architectural Preference calculations are based on the premise of findings from Chapter 4, that vinculin associated with stress fibers (SFs) exhibits gradient loading profile in individual FAs and thus a shift in the $FRET^{-1}$-weighted centroid location from 0 (geometric centroid). Thus, comparing the relative intensities of co-stained proteins of interest in gradient (SF-associated) versus uniformly loaded (LP-associated) FAs provides an indication of the mechanical structures loading vinculin and mechanical context to the FA. Positive values indicate a proteins preferential localization to SF-associated FAs, while negative values indicate a protein's preference for LP-based FAs. (B) Architectural preference was calculated for 22 proteins of interest included in the FFC screen; "+" indicates a significant difference and "0" indicates no significant difference from zero, as measured by one-sample t-test, two-tailed, Bonferroni corrected for multiple comparisons.

These differences in FA composition due to actin architectural preference were not as striking as those brought about by vinculin tension or vinculin knockout. Therefore, we sought to verify a causative role for these different actin structures in modulating FA composition and signaling. We hypothesized that the localization of proteins previously seen to prefer SF structures (with positive Architectural Preference

values), would be repressed in cells only forming LP structures. To test this, we measured changes in FA composition following expression of constitutively active Rac1 (V12). As previously seen in Chapter 4.3 (Figure 4.3.4), transient V12-Rac expression induced broad LP structures (Figure 5.8A, C) which were accompanied by significantly muted vinculin tension spatial gradients. The intensity of both FAK (Arch. Pref. = 0.08) and VASP (Arch. Pref. = 0.22) were found to be significantly reduced in these predominantly LP-associated FAs (Figure 5.8B, D). Compared to mock-transfected cells, VinTS MEFs expressing V12-Rac showed a 10% and 27% drop in average FAK and VASP intensities, respectively (Figure 5.8B, D). These values agree well with the measured architectural preference metrics (Arch. Pref. = 0.08 and 0.23, respectively), indicating that we had measured small, but meaningful changes in FA composition associated with these distinct forms of actin.

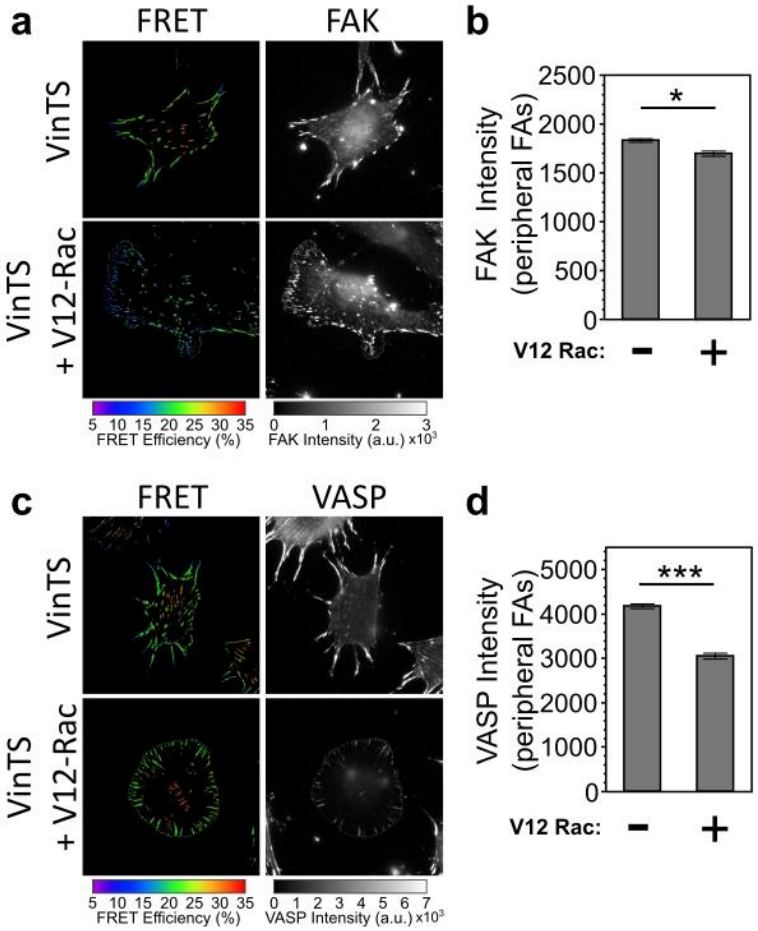

Figure 5.8: Verifying the impact of actin architecture on FA localization of FAK and VASP. (A) Representative images of VinTS masked FRET efficiency and FAK localization in VinTS MEFs either mock transfected or transiently expressing constitutively active V12-Rac1. (B) Quantification of average FAK intensity in peripheral FAs; FAs identified on the acceptor channel of VinTS; n = 21 and 12 cells and n = 1,006 and 1,082 FAs for mock transfected and V12-Rac expressing cells, respectively; * $p < 0.05$, Student's t-test, two-tailed, assuming unequal variances. (C, D) As in (A, B), except cells were stained for VASP; n = 25 and 8 cells and n = 1,011 and 782 FAs for mock transfected and V12-Rac expressing cells, respectively; *** $p < 0.001$, Student's t-test, two-tailed, assuming unequal variances.

5.3.9 Multivariate representation of vinculin mechanotransduction in FAs

To this point, our results indicated that vinculin alone (Figure 5.6), vinculin tension (Figure 5.5), as well as the actin structures loading vinculin (Figure 5.7) all

contribute to changes in composition and likely signaling. To better visualize interactions between these contributing factors and identify a potential vinculin tension-sensitive signaling node, we created a multivariate representation of the combined datasets (Figure 5.9). Other plausible interpretations of this multivariate plot are discussed in the Chapter 5.4). We reasoned that the most likely candidates to exhibit genuine vinculin force-dependent interactions would likely display both loss following vinculin knockout (brighter hues of red) as well as appear as hits in the FFC screen (positive values on y-axis). Interestingly, all five proteins whose localization was reduced in vinculin -/- cells showed evidence of force-dependent localization. Surprisingly, this list includes proteins with little (FAK) or no established (migfilin, zyxin) interactions with vinculin [75] (preppi.org [257]). The other two proteins (VASP, α-actinin4) have been seen to interact with vinculin in vitro [161, 166, 258], and VASP may play a mechanical role in the maintenance of cell-cell junctions [259], but the potential for novel force-dependent interactions between these proteins in FAs has yet to be explored. Furthermore, these top five candidates all appear, on average to preferentially localize to SF-associated FAs (positive values on the x-axis). These five proteins, whose FA localization is coupled to both vinculin and vinculin tension in SF-associated FAs, represent the most likely candidates to exhibit genuine vinculin force-dependent interactions, and were thus the topic of further study.

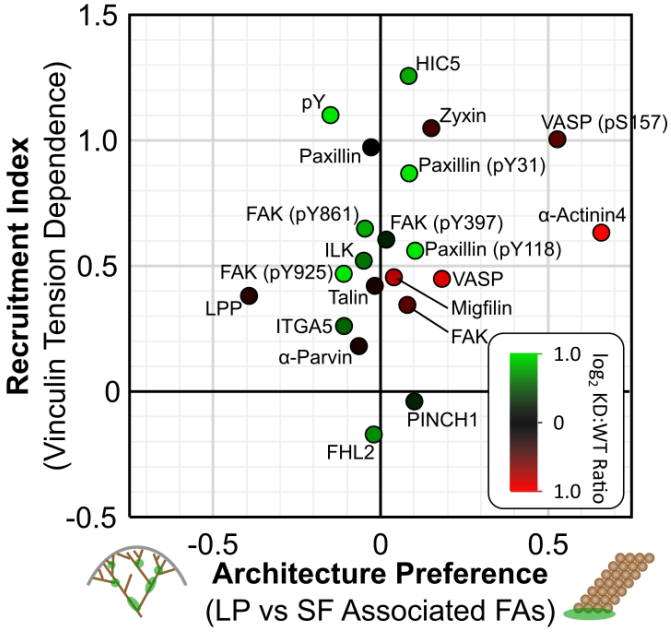

Figure 5.9: Multivariate plot of vinculin-dependent FA composition. Multivariate depiction of vinculin-dependent signaling node was constructed by compiling data about candidate proteins' Architectural Preference (Figure 5.8, x-axis), Recruitment Index (Figure 5.6, y-axis), and KO:WT ratio (Figure 5.7, shades of red to green). See figures 5.6, 5.7, 5.8 for statistical analyses.

5.3.10 Verification of novel vinculin force-dependent PPIs in FAs

Like traditional co-localization, FFC alone is limited by the resolution of light microscopy and can only be used to detect potential, but not verify true PPIs. To determine if novel interactions were forming in a vinculin tension-dependent manner, we used a control sensor containing a point mutation that specifically disrupts vinculin's ability to bind actin (VinTS-I997A) in two final steps.

First, since VinTS-I997A can no longer bear loads (verified in Chapter 4.3.5), we hypothesized that the localization of proteins exhibiting genuine force-dependent interactions would be disrupted specifically by this mutation. Unfortunately, the inability of VinTS-I997A to bear loads also means that we lose critical information (force)

required to calculate recruitment index. In place of this, we fell back on the observation that increasing force-dependent interactions between proteins leads to stronger intensity correlations (Figure 5.2A'). Based on this, we evaluate differences in intensity correlations between either VinTS or VinTS-I997A and our top five candidates. We also evaluated intensity correlations with two negative control groups (vinculin, talin), to further confirm the validity of these analyses. As expected, IF labeling of either vinculin or talin in VinTS and VinTS-I997A cells yielded strong intensity correlation coefficients (Figure 5.10). In contrast, all five candidate proteins exhibited reduced intensity correlations in cells expressing VinTS-I997A. These striking results indicate that, either directly or indirectly, vinculin's ability to bear load influences its interactions, whether they be direct or indirect with VASP, α-actinin4, FAK, migfilin, and zyxin.

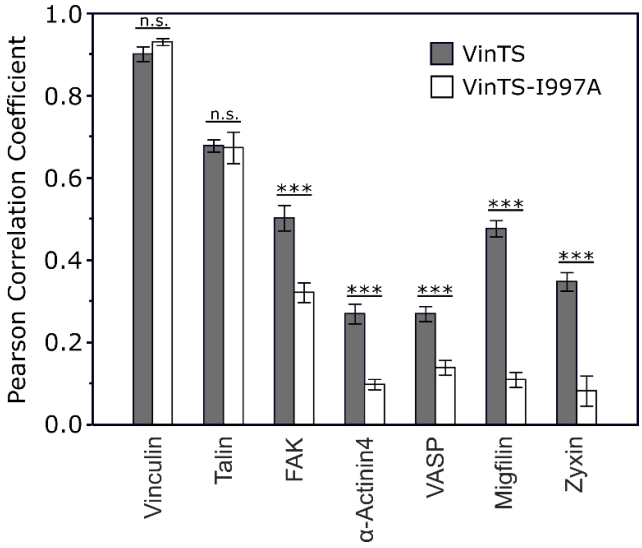

Figure 5.10: Intensity correlations between VinTS and proteins of interest are disrupted by I997A actin binding mutation. Pearson correlation coefficients for the relationship between VinTS or VinTS-I997A acceptor intensity (proportional to sensor concentration) and IF signal for various proteins of interest; n.s. not significant, *** $p < 0.001$ as determined by ANOVA and Tukey's test.

Since the localization of migfilin appeared to be most strongly dependent upon vinculin tension, we used a proximity ligation assay (PLA) [260] to test the hypothesis that vinculin tension is required for the formation of novel vinculin-migfilin complexes in FAs. PLA enables detection of PPIs using complimentary proximity probes, which are antibodies that only produce signal when they bind to targets that reside in close proximity. Thus, comparing PLA signals in cells expressing VinTS and VinTS-I997A provided a means by which to detect vinculin tension-dependent PPIs. We note that in all instances, comparisons of PLA signal were made between cells of comparable spread area and FA number. In a control experiment, VinTS and VinTS-I997A cells exhibited sparse PLA signals when labeled with either a mouse anti-vinculin (V9131) or a rabbit anti-vinculin (ab73412) antibody alone (Figure 5.11A). However, when cells were incubated with both V9131 and ab73412 showed numerous PLA puncta co-localized with the vinculin tension sensor (acceptor channel), indicating that both antibodies frequently labeled the same vinculin molecule. Quantitative analysis of PLA puncta on a per-cell basis revealed no significant difference between VinTS and VinTS-I997A in these control experiments (Figure 5.11B). Using PLA to probe for vinculin tension sensitive vinculin-migfilin PPIs, we observed similarly low PLA signals with single antibodies. When both antibodies were used (anti-vinculin to label VinTS and anti-migfilin to label migfilin), VinTS cells exhibited marked increases in PLA puncta, indicating that vinculin and migfilin indeed interact (Figure 5.11C). Furthermore, these signals were not present with the force-insensitive VinTS-I997A sensor, indicating that these vinculin-migfilin

PPIs are indeed dependent upon and can be modulated by vinculin tension alone. Only with vinculin's actin binding domain intact are increased numbers of PLA puncta detected (Figure 5.11D).

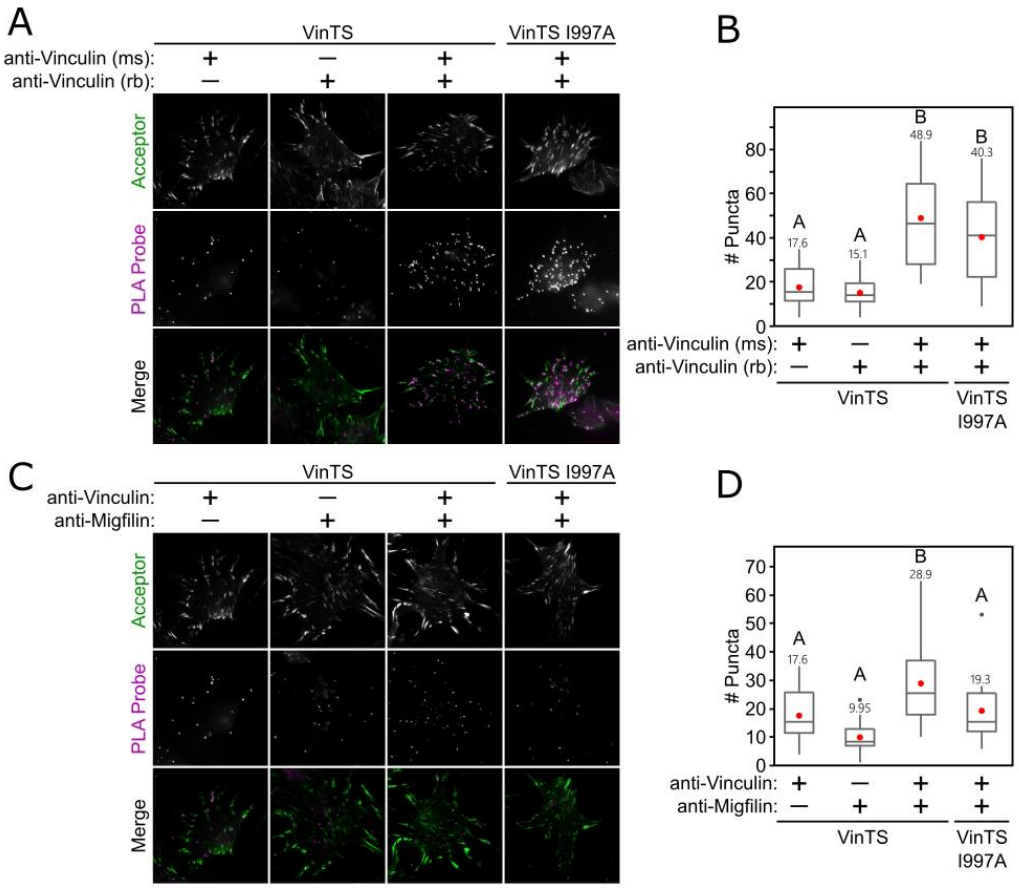

Figure 5.11: Detection of vinculin tension-dependent PPIs in FAs. (A-B) Representative images (A) and quantification (B) of positive control PLA experiment. Samples incubated with either antibody alone produce low background PLA signals. Bright puncta are observed in dual-labeled samples, indicating frequent double-labeling of single vinculin molecules by both mouse anti-vinculin and rabbit anti-vinculin antibodies. From left to right, n = 12, 22, 12, and 14 cells. (C-D) Representative images (A) and quantification (B) of PLA between vinculin (VinTS or VinTS-I997A) and migfilin. Background signals are observed for samples incubated with either mouse anti-vinculin or rabbit anti-migfilin antibodies alone; significant increase in number of PLA puncta and number of PLA puncta associated with FAs are observed only for dual-labeled VinTS. The number of PLA puncta in cells expressing VinTS-I997A were not significantly different from background. From left to right, n = 12, 20, 28, and 14 cells. (B, D) Statistically indistinguishable groups assigned based on ANOVA and Tukey's test with a significance threshold of $p < 0.05$.

5.4 Discussion

5.4.1 Strengths and weaknesses of FFC

In this chapter, we demonstrate some of the benefits and work through some of the drawbacks to using a new imaging-based tool we call fluorescence-force co-localization (FFC). This simple and straightforward technique can provide powerful information as to the molecular enrichment of proteins in areas of high molecular tension (in this case borne by the FA protein vinculin). To our knowledge, this technique is uniquely capable of probing the mechanosensitivity of PPIs in cells. Additionally, as IF-based techniques are used to detect the localization of protein candidates, we were able to quickly screen 20 proteins of interest for their involvement in a potential vinculin tension sensitive signaling node. Even if high-quality antibodies are not available for a particular protein, FFC could be extended to co-localize a FRET sensor with some other far-red tagged FPs, such as iRFP670 [261]. In this manner, for instance, the involvement of the vinculin binding partners ponsin and vinexin [262, 263] in this signaling node could be probed by transient expression of iRFP670-tagged versions of these proteins.

Like traditional co-localization techniques, FFC cannot on its own be used to infer direct molecular interactions between proteins due to resolution limits of traditional light microscopy systems. Thus, FFC is subject to the over-interpretation issues often associated with traditional co-localization techniques [264]. Acknowledging these potential difficulties, we constructed a stochastic model to simulate what potential FFC data might look like. We discovered that visualization of correlations between force

and protein localization required ratiometric measurements rather than raw intensities. Additionally, we define a "Recruitment Index" which can be used to describe the molecular enrichment of other proteins in areas of high molecular tension, simplifying data interpretation to: did my protein of interest go up or go down?

Regardless, to establish direct, force-sensitive PPIs, we needed to compliment FFC with other techniques. Considering several higher resolution techniques exist, including bimolecular FRET [265], fluorescence cross-correlation spectroscopy [266, 267], or proximity labeling technologies [260, 268, 269], we chose the simplest and chose to examine a probable vinculin-migfilin interaction using a proximity ligation assay [260]. Besides its ease of use, PLA also provides the unique ability to detect transient or low-frequency interactions that would normally be hidden from techniques with low signal to noise like bimolecular FRET or mass spectrometry. Additionally, PLA is performed on intact samples, and thus retains spatial information about molecular interactions. Importantly, PLA is not intrinsically force-sensitive. It is only through combination with FFC and that force-sensitive PPIs can be identified and verified.

5.4.2 Implications of force-sensitive PPI between vinculin and migfilin

The FFC screen presented here was critical to discovering a novel force-dependent PPI between vinculin and migfilin, a LIM domain containing protein. Such PPIs are often implicated in mechanical reinforcement events in FAs themselves, as occurs with the talin-vinculin interaction [18, 235] or with signaling events that are

initiated by force-dependent activation or recruitment of protein tyrosine kinases [103] or exposure of cryptic kinase substrate domains [19]. It is also well-established that mechanical signals can affect the nuclear translocation of transcription factors and transcriptional co-regulatory proteins like YAP/TAZ [25] or MRTF [112]. Interestingly, LIM-domain containing proteins are capable of both of these common mechanisms of mechanical regulation as they have been seen to both localize to areas of high mechanical load and also shuttle to the nucleus to regulate transcription [270]. For instance, another of the LIM-domain containing proteins examined in this study, FHL2 has recently been shown to redistribute from FAs to the nucleus in a mechanosensitive manner [271], although our results indicate that this likely occurs independent of vinculin or vinculin tension (Figures 5.3.5, 5.3.6). Regardless, the novel vinculin tension-sensitive migfilin interaction discovered in this study could regulate an analogous mechanosensitive transcriptional outcome. Considering migfilin's established role in regulating genes associated with cardiac overload [272], this possible transcriptional regulation by a force-dependent PPI offers a tempting line for further investigation.

5.5 Summary

In this chapter, we set out to identify the role of vinculin tension in modulating FA composition and signaling through force-dependent interactions with other FA components. However, it was clear that multiple techniques and pieces of information

are required to discern between vinculin tension-dependent changes and compensatory mechanisms within the cell. To accomplish this, we created and adapted a suite of techniques. First, we first examined what proteins failed to localize to FAs lacking vinculin itself and compared the relative IF signals for the 22 protein candidates in WT vs Vin-/- MEFs. Another added dimension came from work done in Chapter 4, where we noticed distinct vinculin spatial loading profiles that corresponded to unique actin architectures. Using this knowledge, we were able to extract information about the actin structures responsible for loading vinculin from the FFC dataset. Importantly, we found that all three of these factors (vinculin, vinculin tension, and actin architecture inferred from vinculin spatial loading profile) had a significant impact on FA composition, indicating their involvement in signaling. This rich dataset was then compiled into a multivariate visualization of a signaling node associated with vinculin tension. Within this network, vinculin tension played particularly important roles in the localization of FAK, VASP, α-actinin4, migfilin, and zyxin. We used PLA to detect a genuine novel vinculin tension-dependent interaction, constituting the first discovery-based identification of force-sensitive signaling inside cells. Finally, while this work focused on the role of vinculin in FA-based mechanosensitive signaling, the analyses presented here make FFC readily translatable to studying mechanosensitive processes in diverse contexts.

6 Conclusions and Future Directions

While the work presented in this dissertation represents a significant advance towards a more mechanistic understanding of mechanobiology, it also opens the door to further investigations in a range of research areas. Most immediately, exploration of cell responses to a variety of mechanical stimuli could provide insight into more physiologically- or pathophysiologically-relevant processes. Furthermore, the technological advances presented in this work also open to the door to studies of mechanically-based signaling in a variety of other systems, including those where very small or very large forces may be very important.

6.1 Exploring the limits of extension-based control of protein loading

The stiffness of the cellular microenvironment is an important regulator of cell behavior and fate. Traditionally, cell responses to substrate rigidity were thought to be governed by some mechanical setpoint, either stress or strain. Extrapolating this idea to the molecular scale, we uncovered a surprising extension-based control for the loading of the FA protein vinculin (Chapter 4). However, these experiments were all performed where the mechanical input was fibronectin-coated glass. If vinculin extension-control and force-control are favored on various stiffness substrates, then vinculin may play a key and currently unappreciated role as a regulator in rigidity sensing. Given FRET sensors and hydrogels have previously been used in concert [139, 140], albeit without the ability to measure the forces experienced by vinculin, experimental evaluation of this

hypothesis is feasible. Experimental modulation of cellular contractile state using cytoskeletal inhibitors could also provide easy means to determine the limits of vinculin extension-control. Excitingly, these experiments could shed light on poorly-understood mechanosensitive mechanisms underlying disease states characterized by either pathological cell contractility, such as asthma [273, 274], or tissue stiffness, which includes cancer [275, 276] and fibrosis [277, 278].

Another major question raised by this work is if other load-bearing proteins are subject to extension-based or force-based control. This could be immediately tested for several proteins for which molecular tension sensors exist, including talin [139, 140], α-actinin [130], filamin [130] at FAs, but also E-cadherin [279], VE-cadherin [280], and PECAM [280] at adherens junctions. Determining the balance of molecular force- versus extension-control in different proteins comprising different subcellular structures could provide insight into mechanosensitive mechanisms across longer length scales [119] and in diverse subcellular structures.

6.2 Elucidating integrin-specific mechanotransduction

In addition to stiffness, the type and density of various ECM components are critical variables in many biological and disease-related processes. Changes in ECM characteristics are hallmarks of disease states like cancer [275, 276] and are critically involved in fibrosis and wound healing [277, 278]. At the cellular level, ECM type can have profound effects on adhesion-dependent signaling, cell contractility, and tissue

formation [281-283]. Even cellular interactions with a single ECM component (e.g. fibronectin), are accomplished through multiple integrin heterodimers, which differentially regulate FA maturation, force transmission, and mechanosensitive signaling pathways [74]. Thus, a comprehensive understanding of mechanotransduction in an integrin-specific fashion is likely critical to a complete understanding mechanosensitive disease.

The tools developed in this dissertation should enable even more informative investigations into these integrin-specific mechanotransduction pathways. Specifically, the improved FRET-based tension sensors described in Chapter 3 should enable robust detection of changes in protein loading downstream of specific integrin ligation. Changes in protein loading could indicate changes in the magnitude of mechanosensitive signaling. Similarly, the FFC technique developed in Chapter 5 should allow for identification of ECM-specific mechanosensitive signaling nodes. We used this technique to identify a vinculin-specific node in a fibronectin-based environment, but vinculin could mediate different signaling in collagen-based or laminin-based ECMs. The FFC technique could be used to characterize the type of mechanosensitive signals activated in response to diverse types of ECM proteins. Such investigations into molecular forces and force-sensitive molecular interactions will be critical to our understanding of mechanosensitive diseases and the interactions between cells and ECM components used in biomaterials and biomimetic scaffolds.

6.3 Monitoring time-varying mechanosensitive processes in FAs

Mechanical loads are often temporally varying in physiological settings. More recently it has been shown that cells dynamically probe the mechanics of static substrates [101]. Thus, observing mechanosensitive processes through time will be critical to further elucidation of mechanotransduction and mechanosensitive disease mechanisms [16]. This need for dynamic perspective on mechanical processes was recently recognized in the realm of super-resolution microscopy, spurring the development of a technique called scanning angle interference microscopy [284]. This technique has enabled the dynamic observation of the 3D localization of FA proteins in migrating cells, but its full potential is just beginning to be realized [185]. Besides visualizing dynamic protein 3D location, the ability to monitor the formation and/or disruption of force-sensitive PPIs through time would provide a very powerful perspective on mechanosensitive processes. This could theoretically be accomplished through a simple extension of the work done in Chapter 5 of this dissertation. In this work, we initially chose to use IF-based detection of protein localization due to its amenability to our screen-based approach. However, in place of IF methods, co-expression of a fluorescently tagged protein-of-interest could enable dynamic FFC measurements and elucidation of the spatiotemporal regulation of force-dependent PPIs. Recently developed FPs in the near-IR range have been developed that make these dynamic measurements even more feasible [285], reducing the potential for spectral

interference between FRET imaging and the FP-tagged protein of interest. These dynamic FFC measurements could provide critical information about the order of events in mechanosensitive processes in live cells.

6.4 Implementation of Molecular Tension Sensors In New Systems

6.4.1 Studying Protein Loading in Other Subcellular Structures

A growing interest in understanding how cells interpret mechanical signals from their microenvironment has driven the development of molecular tension sensors for several proteins. However due to difficulties in calibrating the tension-sensing module (TSMod) portion of the tension sensor, the same TSMod has been frequently recycled to measure loads in other proteins. For example, the TSMod developed in 2010 by Grashoff et al. [131] has been adapted for use in measuring the loads across 5 other proteins (reviewed in [190, 286]), among others currently in development. Despite the range of loads reported by this single sensor, effort at optimizing new TSMods for specific proteins have been limited [139, 194, 195]. Furthermore, molecular tension sensors are often used in a qualitative fashion, reporting on relative changes rather than absolute magnitudes of force. The work in Chapter 3 of this dissertation addresses these limitations, providing both a biophysical understanding to TSMod function required for their rational design as well as a straightforward means to calibrate sensors to absolute forces. The future application of optimized and calibrated sensors should enable

investigations of protein loading and mechanotransduction in biological contexts previously out-of-reach.

6.4.2 Moving Tension Sensors In Vivo

One of the long-term goals of this dissertation was to facilitate future studies of mechanosensitive signaling in more physiologically-relevant systems. Deployment of tension sensors to in vivo systems could provide powerful information into the role of mechanotransduction in higher-order biological regulation. Due to challenges associated with FRET imaging through relatively thick, autofluorescent tissues, initial success is more likely to come from explant studies, engineered tissues, or early embryonic development. Evidence for tension sensor function in vivo does exist [287, 288], however challenges associated with limited dynamic range and questions as to the forces involved in vivo have been raised [289]. The work presented in Chapter 3 of this dissertation takes some of the first steps towards successful tension sensor use in vivo. Notably, we provide the ability to rationally tune the sensitivity of sensors to specific forces, allowing for their deployment in diverse mechanical environments regardless of whether very high or very low forces are involved. Secondly, we describe a straightforward means to sensor calibration in vivo. Employing this method should mitigate concerns about the applicability of in vitro calibrations to sensors used in cellulo or in vivo. Additionally, the FFC methods described in Chapter 5 could theoretically translate to in vivo work and identification of force-sensitive regulation in intact tissue. Overall, more widespread application of the tools described in this

dissertation could shed light on the role of mechanics in biology and provide powerful information to expedite progress in a variety of fields including developmental biology, biophysics, and tissue engineering.

References

[1] C.C. DuFort, M.J. Paszek, V.M. Weaver, Balancing forces: architectural control of mechanotransduction, Nature reviews. Molecular cell biology, 12 (2011) 308-319.

[2] C. Hahn, M.A. Schwartz, Mechanotransduction in vascular physiology and atherogenesis, Nature reviews. Molecular cell biology, 10 (2009) 53-62.

[3] D.E. Jaalouk, J. Lammerding, Mechanotransduction gone awry, Nature reviews. Molecular cell biology, 10 (2009) 63-73.

[4] Y. Sun, C.S. Chen, J. Fu, Forcing stem cells to behave: a biophysical perspective of the cellular microenvironment, Annual review of biophysics, 41 (2012) 519-542.

[5] M.A. Wozniak, C.S. Chen, Mechanotransduction in development: a growing role for contractility, Nature reviews. Molecular cell biology, 10 (2009) 34-43.

[6] T. Mammoto, D.E. Ingber, Mechanical control of tissue and organ development, Development, 137 (2010) 1407-1420.

[7] C.S. Chen, M. Mrksich, S. Huang, G.M. Whitesides, D.E. Ingber, Geometric control of cell life and death, Science, 276 (1997) 1425-1428.

[8] R. McBeath, D.M. Pirone, C.M. Nelson, K. Bhadriraju, C.S. Chen, Cell shape, cytoskeletal tension, and RhoA regulate stem cell lineage commitment, Developmental cell, 6 (2004) 483-495.

[9] S.A. Ruiz, C.S. Chen, Emergence of patterned stem cell differentiation within multicellular structures, Stem cells, 26 (2008) 2921-2927.

[10] C.M. Lo, H.B. Wang, M. Dembo, Y.L. Wang, Cell movement is guided by the rigidity of the substrate, Biophysical journal, 79 (2000) 144-152.

[11] T. Lecuit, P.F. Lenne, Cell surface mechanics and the control of cell shape, tissue patterns and morphogenesis, Nature reviews. Molecular cell biology, 8 (2007) 633-644.

[12] D.T. Butcher, T. Alliston, V.M. Weaver, A tense situation: forcing tumour progression, Nature reviews. Cancer, 9 (2009) 108-122.

[13] A.J. Engler, S. Sen, H.L. Sweeney, D.E. Discher, Matrix elasticity directs stem cell lineage specification, Cell, 126 (2006) 677-689.

[14] J.L. Leight, M.A. Wozniak, S. Chen, M.L. Lynch, C.S. Chen, Matrix rigidity regulates a switch between TGF-beta1-induced apoptosis and epithelial-mesenchymal transition, Molecular biology of the cell, 23 (2012) 781-791.

[15] S.W. Moore, P. Roca-Cusachs, M.P. Sheetz, Stretchy proteins on stretchy substrates: the important elements of integrin-mediated rigidity sensing, Developmental cell, 19 (2010) 194-206.

[16] B.D. Hoffman, C. Grashoff, M.A. Schwartz, Dynamic molecular processes mediate cellular mechanotransduction, Nature, 475 (2011) 316-323.

[17] B.L. Pruitt, A.R. Dunn, W.I. Weis, W.J. Nelson, Mechano-transduction: from molecules to tissues, PLoS Biol, 12 (2014) e1001996.

[18] A. del Rio, R. Perez-Jimenez, R. Liu, P. Roca-Cusachs, J.M. Fernandez, M.P. Sheetz, Stretching single talin rod molecules activates vinculin binding, Science, 323 (2009) 638-641.

[19] Y. Sawada, M. Tamada, B.J. Dubin-Thaler, O. Cherniavskaya, R. Sakai, S. Tanaka, M.P. Sheetz, Force sensing by mechanical extension of the Src family kinase substrate p130Cas, Cell, 127 (2006) 1015-1026.

[20] D.A. Thompson, On Growth and Form, Cambridge Univ. Press1942.

[21] J. Wolff, The Law of Bone Remodelling, Springer.

[22] P.F. Davies, Flow-mediated endothelial mechanotransduction, Physiol Rev, 75 (1995) 519-560.

[23] C. Grobstein, Mechanisms of organogenetic tissue interaction, Natl Cancer Inst Monogr, 26 (1967) 279-299.

[24] A.S. LaCroix, K.E. Rothenberg, B.D. Hoffman, Molecular-Scale Tools for Studying Mechanotransduction, Annual review of biomedical engineering, (2015).

[25] S. Dupont, L. Morsut, M. Aragona, E. Enzo, S. Giulitti, M. Cordenonsi, F. Zanconato, J. Le Digabel, M. Forcato, S. Bicciato, N. Elvassore, S. Piccolo, Role of YAP/TAZ in mechanotransduction, Nature, 474 (2011) 179-183.

[26] R.J. Pelham, Jr., Y. Wang, Cell locomotion and focal adhesions are regulated by substrate flexibility, Proceedings of the National Academy of Sciences of the United States of America, 94 (1997) 13661-13665.

[27] M.J. Paszek, N. Zahir, K.R. Johnson, J.N. Lakins, G.I. Rozenberg, A. Gefen, C.A. Reinhart-King, S.S. Margulies, M. Dembo, D. Boettiger, D.A. Hammer, V.M. Weaver, Tensional homeostasis and the malignant phenotype, Cancer cell, 8 (2005) 241-254.

[28] A.W. Orr, B.P. Helmke, B.R. Blackman, M.A. Schwartz, Mechanisms of mechanotransduction, Developmental cell, 10 (2006) 11-20.

[29] F. Guilak, D.L. Butler, S.A. Goldstein, F.P. Baaijens, Biomechanics and mechanobiology in functional tissue engineering, Journal of biomechanics, 47 (2014) 1933-1940.

[30] N.R. Schiele, J.E. Marturano, C.K. Kuo, Mechanical factors in embryonic tendon development: potential cues for stem cell tenogenesis, Current opinion in biotechnology, 24 (2013) 834-840.

[31] M.S. Kellermayer, S.B. Smith, H.L. Granzier, C. Bustamante, Folding-unfolding transitions in single titin molecules characterized with laser tweezers, Science, 276 (1997) 1112-1116.

[32] K.C. Neuman, A. Nagy, Single-molecule force spectroscopy: optical tweezers, magnetic tweezers and atomic force microscopy, Nature methods, 5 (2008) 491-505.

[33] M.L. Hughes, L. Dougan, The physics of pulling polyproteins: a review of single molecule force spectroscopy using the AFM to study protein unfolding, Rep Prog Phys, 79 (2016) 076601.

[34] A. Basu, T. Ha, The light side of the force, eLife, 5 (2016).

[35] M. Yao, B.T. Goult, H. Chen, P. Cong, M.P. Sheetz, J. Yan, Mechanical activation of vinculin binding to talin locks talin in an unfolded conformation, Scientific reports, 4 (2014) 4610.

[36] L. Rognoni, J. Stigler, B. Pelz, J. Ylanne, M. Rief, Dynamic force sensing of filamin revealed in single-molecule experiments, Proceedings of the National Academy of Sciences of the United States of America, 109 (2012) 19679-19684.

[37] M. Rief, M. Gautel, F. Oesterhelt, J.M. Fernandez, H.E. Gaub, Reversible unfolding of individual titin immunoglobulin domains by AFM, Science, 276 (1997) 1109-1112.

[38] S. Furuike, T. Ito, M. Yamazaki, Mechanical unfolding of single filamin A (ABP-280) molecules detected by atomic force microscopy, FEBS letters, 498 (2001) 72-75.

[39] H. Chen, S. Chandrasekar, M.P. Sheetz, T.P. Stossel, F. Nakamura, J. Yan, Mechanical perturbation of filamin A immunoglobulin repeats 20-21 reveals potential non-equilibrium mechanochemical partner binding function, Scientific reports, 3 (2013) 1642.

[40] V. Ortiz, S.O. Nielsen, M.L. Klein, D.E. Discher, Unfolding a linker between helical repeats, Journal of molecular biology, 349 (2005) 638-647.

[41] V. Vogel, Mechanotransduction involving multimodular proteins: Converting force into biochemical signals, Annual review of biophysics and biomolecular structure, 35 (2006) 459-488.

[42] M.A. Schwartz, D.W. DeSimone, Cell adhesion receptors in mechanotransduction, Current opinion in cell biology, 20 (2008) 551-556.

[43] B. Geiger, J.P. Spatz, A.D. Bershadsky, Environmental sensing through focal adhesions, Nature reviews. Molecular cell biology, 10 (2009) 21-33.

[44] M.L. Gardel, K.E. Kasza, C.P. Brangwynne, J. Liu, D.A. Weitz, Chapter 19: Mechanical response of cytoskeletal networks, Methods in cell biology, 89 (2008) 487-519.

[45] S. Na, O. Collin, F. Chowdhury, B. Tay, M. Ouyang, Y. Wang, N. Wang, Rapid signal transduction in living cells is a unique feature of mechanotransduction, Proceedings of the National Academy of Sciences of the United States of America, 105 (2008) 6626-6631.

[46] Y. Wang, E.L. Botvinick, Y. Zhao, M.W. Berns, S. Usami, R.Y. Tsien, S. Chien, Visualizing the mechanical activation of Src, Nature, 434 (2005) 1040-1045.

[47] C.Y. Lee, J. Lou, K.K. Wen, M. McKane, S.G. Eskin, S. Ono, S. Chien, P.A. Rubenstein, C. Zhu, L.V. McIntire, Actin depolymerization under force is governed by lysine 113:glutamic acid 195-mediated catch-slip bonds, Proceedings of the National Academy of Sciences of the United States of America, 110 (2013) 5022-5027.

[48] B. Guo, W.H. Guilford, Mechanics of actomyosin bonds in different nucleotide states are tuned to muscle contraction, Proceedings of the National Academy of Sciences of the United States of America, 103 (2006) 9844-9849.

[49] J.C. Friedland, M.H. Lee, D. Boettiger, Mechanically activated integrin switch controls alpha5beta1 function, Science, 323 (2009) 642-644.

[50] F. Kong, A.J. Garcia, A.P. Mould, M.J. Humphries, C. Zhu, Demonstration of catch bonds between an integrin and its ligand, The Journal of cell biology, 185 (2009) 1275-1284.

[51] V. Vogel, M. Sheetz, Local force and geometry sensing regulate cell functions, Nature Reviews Molecular Cell Biology, 7 (2006) 265-275.

[52] J. Arnadottir, M. Chalfie, Eukaryotic mechanosensitive channels, Annual review of biophysics, 39 (2010) 111-137.

[53] A.W. Holle, X. Tang, D. Vijayraghavan, L.G. Vincent, A. Fuhrmann, Y.S. Choi, J.C. del Alamo, A.J. Engler, In situ mechanotransduction via vinculin regulates stem cell differentiation, Stem cells, 31 (2013) 2467-2477.

[54] D. Riveline, E. Zamir, N.Q. Balaban, U.S. Schwarz, T. Ishizaki, S. Narumiya, Z. Kam, B. Geiger, A.D. Bershadsky, Focal contacts as mechanosensors: externally applied local mechanical force induces growth of focal contacts by an mDia1-dependent

and ROCK-independent mechanism, The Journal of cell biology, 153 (2001) 1175-1186.

[55] D.E. Leckband, Q. le Duc, N. Wang, J. de Rooij, Mechanotransduction at cadherin-mediated adhesions, Current opinion in cell biology, 23 (2011) 523-530.

[56] A.J. Ehrlicher, F. Nakamura, J.H. Hartwig, D.A. Weitz, T.P. Stossel, Mechanical strain in actin networks regulates FilGAP and integrin binding to filamin A, Nature, 478 (2011) 260-263.

[57] C. Guilluy, V. Swaminathan, R. Garcia-Mata, E.T. O'Brien, R. Superfine, K. Burridge, The Rho GEFs LARG and GEF-H1 regulate the mechanical response to force on integrins, Nature cell biology, 13 (2011) 722-727.

[58] J.M. Mallion, J.P. Baguet, J.P. Siche, F. Tremel, R. De Gaudemaris, Left ventricular hypertrophy and arterial hypertrophy, Advances in experimental medicine and biology, 432 (1997) 123-133.

[59] S.E. Winograd-Katz, S. Itzkovitz, Z. Kam, B. Geiger, Multiparametric analysis of focal adhesion formation by RNAi-mediated gene knockdown, The Journal of cell biology, 186 (2009) 423-436.

[60] K.J. Simpson, L.M. Selfors, J. Bui, A. Reynolds, D. Leake, A. Khvorova, J.S. Brugge, Identification of genes that regulate epithelial cell migration using an siRNA screening approach, Nature cell biology, 10 (2008) 1027-1038.

[61] M. Prager-Khoutorsky, A. Lichtenstein, R. Krishnan, K. Rajendran, A. Mayo, Z. Kam, B. Geiger, A.D. Bershadsky, Fibroblast polarization is a matrix-rigidity-dependent process controlled by focal adhesion mechanosensing, Nature cell biology, 13 (2011) 1457-1465.

[62] S.E. Winograd-Katz, R. Fassler, B. Geiger, K.R. Legate, The integrin adhesome: from genes and proteins to human disease, Nature reviews. Molecular cell biology, 15 (2014) 273-288.

[63] M.R. Morgan, M.J. Humphries, M.D. Bass, Synergistic control of cell adhesion by integrins and syndecans, Nature reviews. Molecular cell biology, 8 (2007) 957-969.

[64] A. Katsumi, A.W. Orr, E. Tzima, M.A. Schwartz, Integrins in mechanotransduction, The Journal of biological chemistry, 279 (2004) 12001-12004.

[65] S.J. Shattil, C. Kim, M.H. Ginsberg, The final steps of integrin activation: the end game, Nature reviews. Molecular cell biology, 11 (2010) 288-300.

[66] D. Bouvard, J. Pouwels, N. De Franceschi, J. Ivaska, Integrin inactivators: balancing cellular functions in vitro and in vivo, Nature reviews. Molecular cell biology, 14 (2013) 430-442.

[67] R. Zaidel-Bar, S. Itzkovitz, A. Ma'ayan, R. Iyengar, B. Geiger, Functional atlas of the integrin adhesome, Nature cell biology, 9 (2007) 858-867.

[68] P. Kanchanawong, G. Shtengel, A.M. Pasapera, E.B. Ramko, M.W. Davidson, H.F. Hess, C.M. Waterman, Nanoscale architecture of integrin-based cell adhesions, Nature, 468 (2010) 580-584.

[69] L.B. Case, M.A. Baird, G. Shtengel, S.L. Campbell, H.F. Hess, M.W. Davidson, C.M. Waterman, Molecular mechanism of vinculin activation and nanoscale spatial organization in focal adhesions, Nature cell biology, 17 (2015) 880-892.

[70] E. Zamir, B. Geiger, Z. Kam, Quantitative multicolor compositional imaging resolves molecular domains in cell-matrix adhesions, PloS one, 3 (2008) e1901.

[71] J.D. Humphries, A. Byron, M.D. Bass, S.E. Craig, J.W. Pinney, D. Knight, M.J. Humphries, Proteomic analysis of integrin-associated complexes identifies RCC2 as a dual regulator of Rac1 and Arf6, Science signaling, 2 (2009) ra51.

[72] J.C. Kuo, X. Han, C.T. Hsiao, J.R. Yates, 3rd, C.M. Waterman, Analysis of the myosin-II-responsive focal adhesion proteome reveals a role for beta-Pix in negative regulation of focal adhesion maturation, Nature cell biology, 13 (2011) 383-393.

[73] H.B. Schiller, C.C. Friedel, C. Boulegue, R. Fassler, Quantitative proteomics of the integrin adhesome show a myosin II-dependent recruitment of LIM domain proteins, EMBO reports, 12 (2011) 259-266.

[74] H.B. Schiller, M.R. Hermann, J. Polleux, T. Vignaud, S. Zanivan, C.C. Friedel, Z. Sun, A. Raducanu, K.E. Gottschalk, M. Thery, M. Mann, R. Fassler, beta1- and alphav-class integrins cooperate to regulate myosin II during rigidity sensing of fibronectin-based microenvironments, Nature cell biology, 15 (2013) 625-636.

[75] E.R. Horton, A. Byron, J.A. Askari, D.H. Ng, A. Millon-Fremillon, J. Robertson, E.J. Koper, N.R. Paul, S. Warwood, D. Knight, J.D. Humphries, M.J. Humphries, Definition of a consensus integrin adhesome and its dynamics during adhesion complex assembly and disassembly, Nature cell biology, 17 (2015) 1577-1587.

[76] C.M. Franz, D.J. Muller, Analyzing focal adhesion structure by atomic force microscopy, Journal of cell science, 118 (2005) 5315-5323.

[77] I. Patla, T. Volberg, N. Elad, V. Hirschfeld-Warneken, C. Grashoff, R. Fassler, J.P. Spatz, B. Geiger, O. Medalia, Dissecting the molecular architecture of integrin adhesion sites by cryo-electron tomography, Nature cell biology, 12 (2010) 909-915.

[78] G. Shtengel, J.A. Galbraith, C.G. Galbraith, J. Lippincott-Schwartz, J.M. Gillette, S. Manley, R. Sougrat, C.M. Waterman, P. Kanchanawong, M.W. Davidson, R.D.

Fetter, H.F. Hess, Interferometric fluorescent super-resolution microscopy resolves 3D cellular ultrastructure, Proceedings of the National Academy of Sciences of the United States of America, 106 (2009) 3125-3130.

[79] U.S. Schwarz, M.L. Gardel, United we stand - integrating the actin cytoskeleton and cell-matrix adhesions in cellular mechanotransduction, Journal of cell science, 125 (2012) 3051-3060.

[80] A.J. Ridley, Rho family proteins: coordinating cell responses, Trends in cell biology, 11 (2001) 471-477.

[81] C.D. Nobes, A. Hall, Rho, rac, and cdc42 GTPases regulate the assembly of multimolecular focal complexes associated with actin stress fibers, lamellipodia, and filopodia, Cell, 81 (1995) 53-62.

[82] K. Burridge, K. Wennerberg, Rho and Rac take center stage, Cell, 116 (2004) 167-179.

[83] C.D. Lawson, K. Burridge, The on-off relationship of Rho and Rac during integrin-mediated adhesion and cell migration, Small GTPases, 5 (2014) e27958.

[84] S. Huveneers, E.H. Danen, Adhesion signaling–crosstalk between integrins, Src and Rho, Journal of cell science, 122 (2009) 1059-1069.

[85] M. Sabouri-Ghomi, Y. Wu, K. Hahn, G. Danuser, Visualizing and quantifying adhesive signals, Current opinion in cell biology, 20 (2008) 541-550.

[86] K. Kemp-O'Brien, M. Parsons, Using FRET to analyse signals controlling cell adhesion and migration, Journal of microscopy, 251 (2013) 270-278.

[87] R.E. Itoh, K. Kurokawa, Y. Ohba, H. Yoshizaki, N. Mochizuki, M. Matsuda, Activation of rac and cdc42 video imaged by fluorescent resonance energy transfer-based single-molecule probes in the membrane of living cells, Mol Cell Biol, 22 (2002) 6582-6591.

[88] P. Nalbant, L. Hodgson, V. Kraynov, A. Toutchkine, K.M. Hahn, Activation of endogenous Cdc42 visualized in living cells, Science, 305 (2004) 1615-1619.

[89] M. Machacek, L. Hodgson, C. Welch, H. Elliott, O. Pertz, P. Nalbant, A. Abell, G.L. Johnson, K.M. Hahn, G. Danuser, Coordination of Rho GTPase activities during cell protrusion, Nature, 461 (2009) 99-103.

[90] O. Pertz, L. Hodgson, R.L. Klemke, K.M. Hahn, Spatiotemporal dynamics of RhoA activity in migrating cells, Nature, 440 (2006) 1069-1072.

[91] H. Yoshizaki, Y. Ohba, K. Kurokawa, R.E. Itoh, T. Nakamura, N. Mochizuki, K. Nagashima, M. Matsuda, Activity of Rho-family GTPases during cell division as visualized with FRET-based probes, The Journal of cell biology, 162 (2003) 223-232.

[92] K. Burridge, C. Guilluy, Focal adhesions, stress fibers and mechanical tension, Experimental cell research, 343 (2016) 14-20.

[93] A.J. Ridley, A. Hall, The small GTP-binding protein rho regulates the assembly of focal adhesions and actin stress fibers in response to growth factors, Cell, 70 (1992) 389-399.

[94] A.J. Ridley, H.F. Paterson, C.L. Johnston, D. Diekmann, A. Hall, The small GTP-binding protein rac regulates growth factor-induced membrane ruffling, Cell, 70 (1992) 401-410.

[95] E.C. Lessey, C. Guilluy, K. Burridge, From mechanical force to RhoA activation, Biochemistry, 51 (2012) 7420-7432.

[96] W.B. Kiosses, S.J. Shattil, N. Pampori, M.A. Schwartz, Rac recruits high-affinity integrin alphavbeta3 to lamellipodia in endothelial cell migration, Nature cell biology, 3 (2001) 316-320.

[97] C.K. Choi, M. Vicente-Manzanares, J. Zareno, L.A. Whitmore, A. Mogilner, A.R. Horwitz, Actin and alpha-actinin orchestrate the assembly and maturation of nascent adhesions in a myosin II motor-independent manner, Nature cell biology, 10 (2008) 1039-1050.

[98] J. Stricker, Y. Beckham, M.W. Davidson, M.L. Gardel, Myosin II-mediated focal adhesion maturation is tension insensitive, PloS one, 8 (2013) e70652.

[99] I. Thievessen, P.M. Thompson, S. Berlemont, K.M. Plevock, S.V. Plotnikov, A. Zemljic-Harpf, R.S. Ross, M.W. Davidson, G. Danuser, S.L. Campbell, C.M. Waterman, Vinculin-actin interaction couples actin retrograde flow to focal adhesions, but is dispensable for focal adhesion growth, The Journal of cell biology, 202 (2013) 163-177.

[100] I. Kaverina, O. Krylyshkina, J.V. Small, Regulation of substrate adhesion dynamics during cell motility, Int J Biochem Cell Biol, 34 (2002) 746-761.

[101] S.V. Plotnikov, A.M. Pasapera, B. Sabass, C.M. Waterman, Force fluctuations within focal adhesions mediate ECM-rigidity sensing to guide directed cell migration, Cell, 151 (2012) 1513-1527.

[102] G. Giannone, M.P. Sheetz, Substrate rigidity and force define form through tyrosine phosphatase and kinase pathways, Trends in cell biology, 16 (2006) 213-223.

[103] B. Yang, Z.Z. Lieu, H. Wolfenson, F.M. Hameed, A.D. Bershadsky, M.P. Sheetz, Mechanosensing Controlled Directly by Tyrosine Kinases, Nano Lett, (2016).

[104] I. Lavelin, H. Wolfenson, I. Patla, Y.I. Henis, O. Medalia, T. Volberg, A. Livne, Z. Kam, B. Geiger, Differential effect of actomyosin relaxation on the dynamic properties of focal adhesion proteins, PloS one, 8 (2013) e73549.

[105] D.J. Webb, K. Donais, L.A. Whitmore, S.M. Thomas, C.E. Turner, J.T. Parsons, A.F. Horwitz, FAK-Src signalling through paxillin, ERK and MLCK regulates adhesion disassembly, Nature cell biology, 6 (2004) 154-161.

[106] S. Huang, D.E. Ingber, The structural and mechanical complexity of cell-growth control, Nature cell biology, 1 (1999) E131-138.

[107] D. Pan, The hippo signaling pathway in development and cancer, Developmental cell, 19 (2010) 491-505.

[108] T. Panciera, L. Azzolin, M. Cordenonsi, S. Piccolo, Mechanobiology of YAP and TAZ in physiology and disease, Nature reviews. Molecular cell biology, (2017).

[109] K.C. Wang, Y.T. Yeh, P. Nguyen, E. Limqueco, J. Lopez, S. Thorossian, K.L. Guan, Y.J. Li, S. Chien, Flow-dependent YAP/TAZ activities regulate endothelial phenotypes and atherosclerosis, Proceedings of the National Academy of Sciences of the United States of America, (2016).

[110] L. Wang, J.Y. Luo, B. Li, X.Y. Tian, L.J. Chen, Y. Huang, J. Liu, D. Deng, C.W. Lau, S. Wan, D. Ai, K.K. Mak, K.K. Tong, K.M. Kwan, N. Wang, J.J. Chiu, Y. Zhu, Y. Huang, Integrin-YAP/TAZ-JNK cascade mediates atheroprotective effect of unidirectional shear flow, Nature, (2016).

[111] A. Elosegui-Artola, I. Andreu, A.E.M. Beedle, A. Lezamiz, M. Uroz, A.J. Kosmalska, R. Oria, J.Z. Kechagia, P. Rico-Lastres, A.L. Le Roux, C.M. Shanahan, X. Trepat, D. Navajas, S. Garcia-Manyes, P. Roca-Cusachs, Force Triggers YAP Nuclear Entry by Regulating Transport across Nuclear Pores, Cell, (2017).

[112] J.T. Connelly, J.E. Gautrot, B. Trappmann, D.W. Tan, G. Donati, W.T. Huck, F.M. Watt, Actin and serum response factor transduce physical cues from the microenvironment to regulate epidermal stem cell fate decisions, Nature cell biology, 12 (2010) 711-718.

[113] M.A. Wozniak, C.Q. Cheng, C.J. Shen, L. Gao, A.O. Olarerin-George, K.J. Won, J.B. Hogenesch, C.S. Chen, Adhesion regulates MAP kinase/ternary complex factor exchange to control a proliferative transcriptional switch, Current biology : CB, 22 (2012) 2017-2026.

[114] M. Dembo, Y.L. Wang, Stresses at the Cell-to-Substrate Interface during Locomotion of Fibroblasts, Biophysical journal, 76 (1999) 2307-2316.

[115] A.K. Harris, P. Wild, D. Stopak, Silicone Rubber Substrata: A New Wrinkle in the Study of Cell Locomotion, Science, 208 (1980) 177-179.

[116] J.L. Martiel, A. Leal, L. Kurzawa, M. Balland, I. Wang, T. Vignaud, Q. Tseng, M. Thery, Measurement of cell traction forces with ImageJ, Methods in cell biology, 125 (2015) 269-287.

[117] N.Q. Balaban, U.S. Schwarz, D. Riveline, P. Goichberg, G. Tzur, I. Sabanay, D. Mahalu, S. Safran, A. Bershadsky, L. Addadi, B. Geiger, Force and focal adhesion assembly: a close relationship studied using elastic micropatterned substrates, Nature cell biology, 3 (2001) 466-472.

[118] J.L. Tan, J. Tien, D.M. Pirone, D.S. Gray, K. Bhadriraju, C.S. Chen, Cells lying on a bed of microneedles: an approach to isolate mechanical force, Proceedings of the National Academy of Sciences of the United States of America, 100 (2003) 1484-1489.

[119] L. Trichet, J. Le Digabel, R.J. Hawkins, S.R. Vedula, M. Gupta, C. Ribrault, P. Hersen, R. Voituriez, B. Ladoux, Evidence of a large-scale mechanosensing mechanism for cellular adaptation to substrate stiffness, Proceedings of the National Academy of Sciences of the United States of America, 109 (2012) 6933-6938.

[120] M. Gupta, L. Kocgozlu, B.R. Sarangi, F. Margadant, M. Ashraf, B. Ladoux, Micropillar substrates: a tool for studying cell mechanobiology, Methods in cell biology, 125 (2015) 289-308.

[121] M. Ghibaudo, A. Saez, L. Trichet, A. Xayaphoummine, J. Browaeys, P. Silberzan, A. Buguin, B. Ladoux, Traction forces and rigidity sensing regulate cell function, Soft Matter, 4 (2008) 1836–1843.

[122] S. Ghassemi, G. Meacci, S. Liu, A.A. Gondarenko, A. Mathur, P. Roca-Cusachs, M.P. Sheetz, J. Hone, Cells test substrate rigidity by local contractions on submicrometer pillars, Proceedings of the National Academy of Sciences of the United States of America, 109 (2012) 5328-5333.

[123] A.K. Yip, K. Iwasaki, C. Ursekar, H. Machiyama, M. Saxena, H. Chen, I. Harada, K.H. Chiam, Y. Sawada, Cellular response to substrate rigidity is governed by either stress or strain, Biophysical journal, 104 (2013) 19-29.

[124] J. Fu, Y.K. Wang, M.T. Yang, R.A. Desai, X. Yu, Z. Liu, C.S. Chen, Mechanical regulation of cell function with geometrically modulated elastomeric substrates, Nature methods, 7 (2010) 733-736.

[125] C.A. Lemmon, C.S. Chen, L.H. Romer, Cell traction forces direct fibronectin matrix assembly, Biophysical journal, 96 (2009) 729-738.

[126] W.R. Legant, C.K. Choi, J.S. Miller, L. Shao, L. Gao, E. Betzig, C.S. Chen, Multidimensional traction force microscopy reveals out-of-plane rotational

moments about focal adhesions, Proceedings of the National Academy of Sciences of the United States of America, 110 (2013) 881-886.

[127] S.A. Maskarinec, C. Franck, D.A. Tirrell, G. Ravichandran, Quantifying cellular traction forces in three dimensions, Proceedings of the National Academy of Sciences of the United States of America, 106 (2009) 22108-22113.

[128] X. Serra-Picamal, V. Conte, R. Sunyer, J.J. Munoz, X. Trepat, Mapping forces and kinematics during collective cell migration, Methods in cell biology, 125 (2015) 309-330.

[129] M. Reffay, M.C. Parrini, O. Cochet-Escartin, B. Ladoux, A. Buguin, S. Coscoy, F. Amblard, J. Camonis, P. Silberzan, Interplay of RhoA and mechanical forces in collective cell migration driven by leader cells, Nature cell biology, 16 (2014) 217-223.

[130] F. Meng, T.M. Suchyna, F. Sachs, A fluorescence energy transfer-based mechanical stress sensor for specific proteins in situ, FEBS J, 275 (2008) 3072-3087.

[131] C. Grashoff, B.D. Hoffman, M.D. Brenner, R. Zhou, M. Parsons, M.T. Yang, M.A. McLean, S.G. Sligar, C.S. Chen, T. Ha, M.A. Schwartz, Measuring mechanical tension across vinculin reveals regulation of focal adhesion dynamics, Nature, 466 (2010) 263-266.

[132] J.R. Lakowicz, Principles of Fluorescence Spectroscopy, 3rd ed ed., Springer, New York, 2006.

[133] A.S. LaCroix, K.E. Rothenberg, M.E. Berginski, A.N. Urs, B.D. Hoffman, Construction, imaging, and analysis of FRET-based tension sensors in living cells, Methods in cell biology, 125 (2015) 161-186.

[134] A. Freikamp, A.L. Cost, C. Grashoff, The Piconewton Force Awakens: Quantifying Mechanics in Cells, Trends in cell biology, (2016).

[135] B.D. Hoffman, The detection and role of molecular tension in focal adhesion dynamics, Prog Mol Biol Transl Sci, 126 (2014) 3-24.

[136] M.L. Smith, D. Gourdon, W.C. Little, K.E. Kubow, R.A. Eguiluz, S. Luna-Morris, V. Vogel, Force-induced unfolding of fibronectin in the extracellular matrix of living cells, PLoS Biol, 5 (2007) e268.

[137] E. Klotzsch, M.L. Smith, K.E. Kubow, S. Muntwyler, W.C. Little, F. Beyeler, D. Gourdon, B.J. Nelson, V. Vogel, Fibronectin forms the most extensible biological fibers displaying switchable force-exposed cryptic binding sites, Proceedings of the National Academy of Sciences of the United States of America, 106 (2009) 18267-18272.

[138] F. Nakamura, M. Song, J.H. Hartwig, T.P. Stossel, Documentation and localization of force-mediated filamin A domain perturbations in moving cells, Nat Commun, 5 (2014) 4656.

[139] K. Austen, P. Ringer, A. Mehlich, A. Chrostek-Grashoff, C. Kluger, C. Klingner, B. Sabass, R. Zent, M. Rief, C. Grashoff, Extracellular rigidity sensing by talin isoform-specific mechanical linkages, Nature cell biology, 17 (2015) 1597-1606.

[140] A. Kumar, M. Ouyang, K. Van den Dries, E.J. McGhee, K. Tanaka, M.D. Anderson, A. Groisman, B.T. Goult, K.I. Anderson, M.A. Schwartz, Talin tension sensor reveals novel features of focal adhesion force transmission and mechanosensitivity, The Journal of cell biology, 213 (2016) 371-383.

[141] L. Przybyla, J.M. Muncie, V.M. Weaver, Mechanical Control of Epithelial-to-Mesenchymal Transitions in Development and Cancer, Annual review of cell and developmental biology, (2016).

[142] X. Lin, Y. Shi, Y. Cao, W. Liu, Recent progress in stem cell differentiation directed by material and mechanical cues, Biomed Mater, 11 (2016) 014109.

[143] N.D. Gallant, K.E. Michael, A.J. Garcia, Cell adhesion strengthening: contributions of adhesive area, integrin binding, and focal adhesion assembly, Molecular biology of the cell, 16 (2005) 4329-4340.

[144] K.A. Beningo, M. Dembo, I. Kaverina, J.V. Small, Y.L. Wang, Nascent focal adhesions are responsible for the generation of strong propulsive forces in migrating fibroblasts, The Journal of cell biology, 153 (2001) 881-888.

[145] J.M. Goffin, P. Pittet, G. Csucs, J.W. Lussi, J.J. Meister, B. Hinz, Focal adhesion size controls tension-dependent recruitment of alpha-smooth muscle actin to stress fibers, The Journal of cell biology, 172 (2006) 259-268.

[146] M.L. Gardel, B. Sabass, L. Ji, G. Danuser, U.S. Schwarz, C.M. Waterman, Traction stress in focal adhesions correlates biphasically with actin retrograde flow speed, The Journal of cell biology, 183 (2008) 999-1005.

[147] J. Stricker, Y. Aratyn-Schaus, P.W. Oakes, M.L. Gardel, Spatiotemporal constraints on the force-dependent growth of focal adhesions, Biophysical journal, 100 (2011) 2883-2893.

[148] M.L. Gardel, I.C. Schneider, Y. Aratyn-Schaus, C.M. Waterman, Mechanical integration of actin and adhesion dynamics in cell migration, Annual review of cell and developmental biology, 26 (2010) 315-333.

[149] S.L. Gupton, C.M. Waterman-Storer, Spatiotemporal feedback between actomyosin and focal-adhesion systems optimizes rapid cell migration, Cell, 125 (2006) 1361-1374.

[150] S.J. Franco, M.A. Rodgers, B.J. Perrin, J. Han, D.A. Bennin, D.R. Critchley, A. Huttenlocher, Calpain-mediated proteolysis of talin regulates adhesion dynamics, Nature cell biology, 6 (2004) 977-983.

[151] P.A. Janmey, J.P. Winer, M.E. Murray, Q. Wen, The hard life of soft cells, Cell motility and the cytoskeleton, 66 (2009) 597-605.

[152] D.E. Discher, P. Janmey, Y.L. Wang, Tissue cells feel and respond to the stiffness of their substrate, Science, 310 (2005) 1139-1143.

[153] T. Luo, K. Mohan, P.A. Iglesias, D.N. Robinson, Molecular mechanisms of cellular mechanosensing, Nature materials, 12 (2013) 1064-1071.

[154] A. Saez, A. Buguin, P. Silberzan, B. Ladoux, Is the mechanical activity of epithelial cells controlled by deformations or forces?, Biophysical journal, 89 (2005) L52-54.

[155] C. Jurchenko, K.S. Salaita, Lighting Up the Force: Investigating Mechanisms of Mechanotransduction Using Fluorescent Tension Probes, Mol Cell Biol, 35 (2015) 2570-2582.

[156] C. Bakolitsa, D.M. Cohen, L.A. Bankston, A.A. Bobkov, G.W. Cadwell, L. Jennings, D.R. Critchley, S.W. Craig, R.C. Liddington, Structural basis for vinculin activation at sites of cell adhesion, Nature, 430 (2004) 583-586.

[157] R.P. Johnson, S.W. Craig, An intramolecular association between the head and tail domains of vinculin modulates talin binding, The Journal of biological chemistry, 269 (1994) 12611-12619.

[158] K.R. Legate, S. Takahashi, N. Bonakdar, B. Fabry, D. Boettiger, R. Zent, R. Fassler, Integrin adhesion and force coupling are independently regulated by localized PtdIns(4,5)2 synthesis, The EMBO journal, 30 (2011) 4539-4553.

[159] A.M. Pasapera, I.C. Schneider, E. Rericha, D.D. Schlaepfer, C.M. Waterman, Myosin II activity regulates vinculin recruitment to focal adhesions through FAK-mediated paxillin phosphorylation, The Journal of cell biology, 188 (2010) 877-890.

[160] K. Burridge, P. Mangeat, An interaction between vinculin and talin, Nature, 308 (1984) 744-746.

[161] D.H. Wachsstock, J.A. Wilkins, S. Lin, Specific interaction of vinculin with alpha-actinin, Biochem Biophys Res Commun, 146 (1987) 554-560.

[162] C.E. Turner, J.R. Glenney, Jr., K. Burridge, Paxillin: a new vinculin-binding protein present in focal adhesions, The Journal of cell biology, 111 (1990) 1059-1068.

[163] C.E. Turner, J.T. Miller, Primary sequence of paxillin contains putative SH2 and SH3 domain binding motifs and multiple LIM domains: identification of a

vinculin and pp125Fak-binding region, Journal of cell science, 107 (Pt 6) (1994) 1583-1591.

[164] C.K. Wood, C.E. Turner, P. Jackson, D.R. Critchley, Characterisation of the paxillin-binding site and the C-terminal focal adhesion targeting sequence in vinculin, Journal of cell science, 107 (Pt 2) (1994) 709-717.

[165] S.M. Thomas, M. Hagel, C.E. Turner, Characterization of a focal adhesion protein, Hic-5, that shares extensive homology with paxillin, Journal of cell science, 112 (Pt 2) (1999) 181-190.

[166] N.P. Brindle, M.R. Holt, J.E. Davies, C.J. Price, D.R. Critchley, The focal-adhesion vasodilator-stimulated phosphoprotein (VASP) binds to the proline-rich domain in vinculin, Biochem J, 318 (Pt 3) (1996) 753-757.

[167] K. Mandai, H. Nakanishi, A. Satoh, K. Takahashi, K. Satoh, H. Nishioka, A. Mizoguchi, Y. Takai, Ponsin/SH3P12: an l-afadin- and vinculin-binding protein localized at cell-cell and cell-matrix adherens junctions, The Journal of cell biology, 144 (1999) 1001-1017.

[168] N. Kioka, S. Sakata, T. Kawauchi, T. Amachi, S.K. Akiyama, K. Okazaki, C. Yaen, K.M. Yamada, S. Aota, Vinexin: a novel vinculin-binding protein with multiple SH3 domains enhances actin cytoskeletal organization, The Journal of cell biology, 144 (1999) 59-69.

[169] K.A. DeMali, C.A. Barlow, K. Burridge, Recruitment of the Arp2/3 complex to vinculin: coupling membrane protrusion to matrix adhesion, The Journal of cell biology, 159 (2002) 881-891.

[170] R.P. Johnson, S.W. Craig, F-actin binding site masked by the intramolecular association of vinculin head and tail domains, Nature, 373 (1995) 261-264.

[171] P.R. Bois, B.P. O'Hara, D. Nietlispach, J. Kirkpatrick, T. Izard, The vinculin binding sites of talin and alpha-actinin are sufficient to activate vinculin, The Journal of biological chemistry, 281 (2006) 7228-7236.

[172] H. Chen, D.M. Choudhury, S.W. Craig, Coincidence of actin filaments and talin is required to activate vinculin, The Journal of biological chemistry, 281 (2006) 40389-40398.

[173] C.T. Mierke, P. Kollmannsberger, D.P. Zitterbart, J. Smith, B. Fabry, W.H. Goldmann, Mechano-coupling and regulation of contractility by the vinculin tail domain, Biophysical journal, 94 (2008) 661-670.

[174] K. Kupper, N. Lang, C. Mohl, N. Kirchgessner, S. Born, W.H. Goldmann, R. Merkel, B. Hoffmann, Tyrosine phosphorylation of vinculin at position 1065

modifies focal adhesion dynamics and cell tractions, Biochem Biophys Res Commun, 399 (2010) 560-564.

[175] G. Diez, V. Auernheimer, B. Fabry, W.H. Goldmann, Head/tail interaction of vinculin influences cell mechanical behavior, Biochem Biophys Res Commun, 406 (2011) 85-88.

[176] K.M. Jannie, S.M. Ellerbroek, D.W. Zhou, S. Chen, D.J. Crompton, A.J. Garcia, K.A. DeMali, Vinculin-dependent actin bundling regulates cell migration and traction forces, Biochem J, 465 (2015) 383-393.

[177] D.W. Dumbauld, T.T. Lee, A. Singh, J. Scrimgeour, C.A. Gersbach, E.A. Zamir, J. Fu, C.S. Chen, J.E. Curtis, S.W. Craig, A.J. Garcia, How vinculin regulates force transmission, Proceedings of the National Academy of Sciences of the United States of America, 110 (2013) 9788-9793.

[178] D.L. Huang, N.A. Bax, C.D. Buckley, W.I. Weis, A.R. Dunn, Vinculin forms a directionally asymmetric catch bond with F-actin, Science, 357 (2017) 703-706.

[179] P. Hernandez-Varas, U. Berge, J.G. Lock, S. Stromblad, A plastic relationship between vinculin-mediated tension and adhesion complex area defines adhesion size and lifetime, Nat Commun, 6 (2015) 7524.

[180] W. Xu, H. Baribault, E.D. Adamson, Vinculin knockout results in heart and brain defects during embryonic development, Development, 125 (1998) 327-337.

[181] K. Garakani, H. Shams, M.R.K. Mofrad, Mechanosensitive Conformation of Vinculin Regulates Its Binding to MAPK1, Biophysical journal, 112 (2017) 1885-1893.

[182] A. Carisey, R. Tsang, A.M. Greiner, N. Nijenhuis, N. Heath, A. Nazgiewicz, R. Kemkemer, B. Derby, J. Spatz, C. Ballestrem, Vinculin regulates the recruitment and release of core focal adhesion proteins in a force-dependent manner, Current biology : CB, 23 (2013) 271-281.

[183] C.T. Mierke, P. Kollmannsberger, D.P. Zitterbart, G. Diez, T.M. Koch, S. Marg, W.H. Ziegler, W.H. Goldmann, B. Fabry, Vinculin facilitates cell invasion into three-dimensional collagen matrices, The Journal of biological chemistry, 285 (2010) 13121-13130.

[184] I. Thievessen, N. Fakhri, J. Steinwachs, V. Kraus, R.S. McIsaac, L. Gao, B.C. Chen, M.A. Baird, M.W. Davidson, E. Betzig, R. Oldenbourg, C.M. Waterman, B. Fabry, Vinculin is required for cell polarization, migration, and extracellular matrix remodeling in 3D collagen, FASEB journal : official publication of the Federation of American Societies for Experimental Biology, 29 (2015) 4555-4567.

[185] M.G. Rubashkin, L. Cassereau, R. Bainer, C.C. DuFort, Y. Yui, G. Ou, M.J. Paszek, M.W. Davidson, Y.Y. Chen, V.M. Weaver, Force Engages Vinculin and Promotes Tumor Progression by Enhancing PI3K Activation of Phosphatidylinositol (3,4,5)-Triphosphate, Cancer research, 74 (2014) 4597-4611.

[186] A.D. Doyle, F.W. Wang, K. Matsumoto, K.M. Yamada, One-dimensional topography underlies three-dimensional fibrillar cell migration, The Journal of cell biology, 184 (2009) 481-490.

[187] P.P. Provenzano, P.J. Keely, Mechanical signaling through the cytoskeleton regulates cell proliferation by coordinated focal adhesion and Rho GTPase signaling, Journal of cell science, 124 (2011) 1195-1205.

[188] S.J. Heo, T.P. Driscoll, S.D. Thorpe, N.L. Nerurkar, B.M. Baker, M.T. Yang, C.S. Chen, D.A. Lee, R.L. Mauck, Differentiation alters stem cell nuclear architecture, mechanics, and mechano-sensitivity, eLife, 5 (2016).

[189] C.P. Heisenberg, Y. Bellaiche, Forces in tissue morphogenesis and patterning, Cell, 153 (2013) 948-962.

[190] A.L. Cost, P. Ringer, A. Chrostek-Grashoff, C. Grashoff, How to Measure Molecular Forces: A Guide to Evaluating Genetically-Encoded FRET-Based Tension Sensors, Cell Mol Bioeng, (2015).

[191] L. Ju, Y. Chen, L. Xue, X. Du, C. Zhu, Cooperative unfolding of distinctive mechanoreceptor domains transduces force into signals, eLife, 5 (2016).

[192] K. Austen, C. Kluger, A. Freikamp, A. Chrostek-Grashoff, C. Grashoff, Generation and analysis of biosensors to measure mechanical forces within cells, Methods Mol Biol, 1066 (2013) 169-184.

[193] A. Freikamp, A. Mehlich, C. Klingner, C. Grashoff, Investigating piconewton forces in cells by FRET-based molecular force microscopy, J Struct Biol, (2016).

[194] M.D. Brenner, R. Zhou, D.E. Conway, L. Lanzano, E. Gratton, M.A. Schwartz, T. Ha, Spider silk peptide is a compact, linear nano-spring ideal for intracellular tension sensing, Nano Lett, (2016).

[195] P. Ringer, A. Weissl, A.L. Cost, A. Freikamp, B. Sabass, A. Mehlich, M. Tramier, M. Rief, C. Grashoff, Multiplexing molecular tension sensors reveals piconewton force gradient across talin-1, Nature methods, (2017).

[196] N.B. Becker, A. Rosa, R. Everaers, The radial distribution function of worm-like chains, Eur Phys J E Soft Matter, 32 (2010) 53-69.

[197] H.W. Ai, J.N. Henderson, S.J. Remington, R.E. Campbell, Directed evolution of a monomeric, bright and photostable version of Clavularia cyan fluorescent

protein: structural characterization and applications in fluorescence imaging, Biochem J, 400 (2006) 531-540.

[198] T. Nagai, K. Ibata, E.S. Park, M. Kubota, K. Mikoshiba, A. Miyawaki, A variant of yellow fluorescent protein with fast and efficient maturation for cell-biological applications, Nat Biotechnol, 20 (2002) 87-90.

[199] A.J. Lam, F. St-Pierre, Y. Gong, J.D. Marshall, P.J. Cranfill, M.A. Baird, M.R. McKeown, J. Wiedenmann, M.W. Davidson, M.J. Schnitzer, R.Y. Tsien, M.Z. Lin, Improving FRET dynamic range with bright green and red fluorescent proteins, Nature methods, 9 (2012) 1005-1012.

[200] T.H. Evers, E.M. van Dongen, A.C. Faesen, E.W. Meijer, M. Merkx, Quantitative understanding of the energy transfer between fluorescent proteins connected via flexible peptide linkers, Biochemistry, 45 (2006) 13183-13192.

[201] H. Chen, H.L. Puhl, 3rd, S.V. Koushik, S.S. Vogel, S.R. Ikeda, Measurement of FRET efficiency and ratio of donor to acceptor concentration in living cells, Biophysical journal, 91 (2006) L39-41.

[202] K.E. Rothenberg, S.S. Neibart, A.S. LaCroix, B.D. Hoffman, Controlling Cell Geometry Affects the Spatial Distribution of Load Across Vinculin, Cell Mol Bioeng, 8 (2015) 364-382.

[203] E. Zamir, B.Z. Katz, S. Aota, K.M. Yamada, B. Geiger, Z. Kam, Molecular diversity of cell-matrix adhesions, Journal of cell science, 112 (1999) 1655-1669.

[204] H. Chen, D.M. Cohen, D.M. Choudhury, N. Kioka, S.W. Craig, Spatial distribution and functional significance of activated vinculin in living cells, The Journal of cell biology, 169 (2005) 459-470.

[205] Z.K. Majumdar, R. Hickerson, H.F. Noller, R.M. Clegg, Measurements of internal distance changes of the 30S ribosome using FRET with multiple donor-acceptor pairs: quantitative spectroscopic methods, Journal of molecular biology, 351 (2005) 1123-1145.

[206] T. Ohashi, S.D. Galiacy, G. Briscoe, H.P. Erickson, An experimental study of GFP-based FRET, with application to intrinsically unstructured proteins, Protein Sci, 16 (2007) 1429-1438.

[207] X. Li, G. Zhang, N. Ngo, X. Zhao, S.R. Kain, C.C. Huang, Deletions of the Aequorea victoria green fluorescent protein define the minimal domain required for fluorescence, The Journal of biological chemistry, 272 (1997) 28545-28549.

[208] S. Shimozono, H. Hosoi, H. Mizuno, T. Fukano, T. Tahara, A. Miyawaki, Concatenation of cyan and yellow fluorescent proteins for efficient resonance energy transfer, Biochemistry, 45 (2006) 6267-6271.

[209] M. Ouyang, J. Sun, S. Chien, Y. Wang, Determination of hierarchical relationship of Src and Rac at subcellular locations with FRET biosensors, Proceedings of the National Academy of Sciences of the United States of America, 105 (2008) 14353-14358.

[210] N. Becker, E. Oroudjev, S. Mutz, J.P. Cleveland, P.K. Hansma, C.Y. Hayashi, D.E. Makarov, H.G. Hansma, Molecular nanosprings in spider capture-silk threads, Nature materials, 2 (2003) 278-283.

[211] S.S. Vogel, B.W. van der Meer, P.S. Blank, Estimating the distance separating fluorescent protein FRET pairs, Methods, 66 (2014) 131-138.

[212] J. Marko, E.D. Siggia, Stretching DNA, Macromolecules, 28 (1995) 8759-8770.

[213] C. Bouchiat, M.D. Wang, J. Allemand, T. Strick, S.M. Block, V. Croquette, Estimating the persistence length of a worm-like chain molecule from force-extension measurements, Biophysical journal, 76 (1999) 409-413.

[214] S.S. Vogel, T.A. Nguyen, B.W. van der Meer, P.S. Blank, The impact of heterogeneity and dark acceptor states on FRET: implications for using fluorescent protein donors and acceptors, PloS one, 7 (2012) e49593.

[215] H.E. Daniels, The Statistical Theory of Stiff Chains, 63 (1952) 290-311.

[216] H. Yamakawa, W.H. Stockmayer, Statistical Mechanics of Wormlike Chains .2. Excluded Volume Effects, Journal of Chemical Physics, 57 (1972) 2843-+.

[217] J. Wilhelm, E. Frey, Radial distribution function of semiflexible polymers, Physical Review Letters, 77 (1996) 2581.

[218] J.T. Titantah, C. Pierleoni, J.P. Ryckaert, Different statistical mechanical ensembles for a stretched polymer, Phys Rev E Stat Phys Plasmas Fluids Relat Interdiscip Topics, 60 (1999) 7010-7021.

[219] M. Ormo, A.B. Cubitt, K. Kallio, L.A. Gross, R.Y. Tsien, S.J. Remington, Crystal structure of the Aequorea victoria green fluorescent protein, Science, 273 (1996) 1392-1395.

[220] A. Rekas, J.R. Alattia, T. Nagai, A. Miyawaki, M. Ikura, Crystal structure of venus, a yellow fluorescent protein with improved maturation and reduced environmental sensitivity, The Journal of biological chemistry, 277 (2002) 50573-50578.

[221] M.A. Hink, R.A. Griep, J.W. Borst, A. van Hoek, M.H. Eppink, A. Schots, A.J. Visser, Structural dynamics of green fluorescent protein alone and fused with a single chain Fv protein, The Journal of biological chemistry, 275 (2000) 17556-17560.

[222] H.S. Muddana, T.T. Morgan, J.H. Adair, P.J. Butler, Photophysics of Cy3-encapsulated calcium phosphate nanoparticles, Nano Lett, 9 (2009) 1559-1566.

[223] J. Widengren, P. Schwille, Characterization of photoinduced isomerization and back-isomerization of the cyanine dye Cy5 by fluorescence correlation spectroscopy, J Phys Chem A, 104 (2000) 6416-6428.

[224] M.E. Sanborn, B.K. Connolly, K. Gurunathan, M. Levitus, Fluorescence properties and photophysics of the sulfoindocyanine Cy3 linked covalently to DNA, J Phys Chem B, 111 (2007) 11064-11074.

[225] S. Buckhout-White, C.M. Spillmann, W.R. Algar, A. Khachatrian, J.S. Melinger, E.R. Goldman, M.G. Ancona, I.L. Medintz, Assembling programmable FRET-based photonic networks using designer DNA scaffolds, Nat Commun, 5 (2014) 5615.

[226] A. Dittmore, D.B. McIntosh, S. Halliday, O.A. Saleh, Single-molecule elasticity measurements of the onset of excluded volume in poly(ethylene glycol), Phys Rev Lett, 107 (2011) 148301.

[227] P.A. Pincus, Excluded Volume Effects and Stretched Polymer Chains, Macromolecules, 9 (1976) 386–388.

[228] B.R. Sarangi, M. Gupta, B.L. Doss, N. Tissot, F. Lam, R.M. Mege, N. Borghi, B. Ladoux, Coordination between Intra- and Extracellular Forces Regulates Focal Adhesion Dynamics, Nano Lett, 17 (2017) 399-406.

[229] B.L. Blakely, C.E. Dumelin, B. Trappmann, L.M. McGregor, C.K. Choi, P.C. Anthony, V.K. Duesterberg, B.M. Baker, S.M. Block, D.R. Liu, C.S. Chen, A DNA-based molecular probe for optically reporting cellular traction forces, Nature methods, 11 (2014) 1229-1232.

[230] M. Morimatsu, A.H. Mekhdjian, A.C. Chang, S.J. Tan, A.R. Dunn, Visualizing the interior architecture of focal adhesions with high-resolution traction maps, Nano Lett, 15 (2015) 2220-2228.

[231] A.L. Eastwood, A. Sanzeni, B.C. Petzold, S.J. Park, M. Vergassola, B.L. Pruitt, M.B. Goodman, Tissue mechanics govern the rapidly adapting and symmetrical response to touch, Proceedings of the National Academy of Sciences of the United States of America, 112 (2015) E6955-6963.

[232] Z. Sun, S.S. Guo, R. Fassler, Integrin-mediated mechanotransduction, The Journal of cell biology, 215 (2016) 445-456.

[233] X. Hu, F.M. Margadant, M. Yao, M.P. Sheetz, Molecular stretching modulates mechanosensing pathways, Protein Sci, 26 (2017) 1337-1351.

[234] S. Bell, E.M. Terentjev, Focal Adhesion Kinase: The Reversible Molecular Mechanosensor, Biophysical journal, 112 (2017) 2439-2450.

[235] X. Hu, C. Jing, X. Xu, N. Nakazawa, V.W. Cornish, F.M. Margadant, M.P. Sheetz, Cooperative Vinculin Binding to Talin Mapped by Time Resolved Super Resolution Microscopy, Nano Lett, (2016).

[236] M. Chrzanowska-Wodnicka, K. Burridge, Rho-stimulated contractility drives the formation of stress fibers and focal adhesions, The Journal of cell biology, 133 (1996) 1403-1415.

[237] P.W. Oakes, Y. Beckham, J. Stricker, M.L. Gardel, Tension is required but not sufficient for focal adhesion maturation without a stress fiber template, The Journal of cell biology, 196 (2012) 363-374.

[238] G. Totsukawa, Y. Yamakita, S. Yamashiro, D.J. Hartshorne, Y. Sasaki, F. Matsumura, Distinct roles of ROCK (Rho-kinase) and MLCK in spatial regulation of MLC phosphorylation for assembly of stress fibers and focal adhesions in 3T3 fibroblasts, The Journal of cell biology, 150 (2000) 797-806.

[239] Y. Aratyn-Schaus, P.W. Oakes, M.L. Gardel, Dynamic and structural signatures of lamellar actomyosin force generation, Molecular biology of the cell, 22 (2011) 1330-1339.

[240] Y. Cai, N. Biais, G. Giannone, M. Tanase, G. Jiang, J.M. Hofman, C.H. Wiggins, P. Silberzan, A. Buguin, B. Ladoux, M.P. Sheetz, Nonmuscle myosin IIA-dependent force inhibits cell spreading and drives F-actin flow, Biophysical journal, 91 (2006) 3907-3920.

[241] C.M. Waterman-Storer, A. Desai, J.C. Bulinski, E.D. Salmon, Fluorescent speckle microscopy, a method to visualize the dynamics of protein assemblies in living cells, Current biology : CB, 8 (1998) 1227-1230.

[242] K. Hu, L. Ji, K.T. Applegate, G. Danuser, C.M. Waterman-Storer, Differential transmission of actin motion within focal adhesions, Science, 315 (2007) 111-115.

[243] D.M. Cohen, B. Kutscher, H. Chen, D.B. Murphy, S.W. Craig, A conformational switch in vinculin drives formation and dynamics of a talin-vinculin complex at focal adhesions, The Journal of biological chemistry, 281 (2006) 16006-16015.

[244] J. Liu, Y. Wang, W.I. Goh, H. Goh, M.A. Baird, S. Ruehland, S. Teo, N. Bate, D.R. Critchley, M.W. Davidson, P. Kanchanawong, Talin determines the nanoscale architecture of focal adhesions, Proceedings of the National Academy of Sciences of the United States of America, 112 (2015) E4864-4873.

[245] P. Atherton, B. Stutchbury, D.Y. Wang, D. Jethwa, R. Tsang, E. Meiler-Rodriguez, P. Wang, N. Bate, R. Zent, I.L. Barsukov, B.T. Goult, D.R. Critchley, C. Ballestrem, Vinculin controls talin engagement with the actomyosin machinery, Nat Commun, 6 (2015) 10038.

[246] A. Bershadsky, M. Kozlov, B. Geiger, Adhesion-mediated mechanosensitivity: a time to experiment, and a time to theorize, Current opinion in cell biology, 18 (2006) 472-481.

[247] T. Shemesh, B. Geiger, A.D. Bershadsky, M.M. Kozlov, Focal adhesions as mechanosensors: a physical mechanism, Proceedings of the National Academy of Sciences of the United States of America, 102 (2005) 12383-12388.

[248] A. Nicolas, B. Geiger, S.A. Safran, Cell mechanosensitivity controls the anisotropy of focal adhesions, Proceedings of the National Academy of Sciences of the United States of America, 101 (2004) 12520-12525.

[249] A. Besser, S.A. Safran, Force-induced adsorption and anisotropic growth of focal adhesions, Biophysical journal, 90 (2006) 3469-3484.

[250] J.E. Olberding, M.D. Thouless, E.M. Arruda, K. Garikipati, The non-equilibrium thermodynamics and kinetics of focal adhesion dynamics, PloS one, 5 (2010) e12043.

[251] A. Nicolas, A. Besser, S.A. Safran, Dynamics of cellular focal adhesions on deformable substrates: Consequences for cell force microscopy, Biophysical journal, 95 (2008) 527-539.

[252] P. Roca-Cusachs, A. del Rio, E. Puklin-Faucher, N.C. Gauthier, N. Biais, M.P. Sheetz, Integrin-dependent force transmission to the extracellular matrix by alpha-actinin triggers adhesion maturation, Proceedings of the National Academy of Sciences of the United States of America, 110 (2013) E1361-1370.

[253] E.S. Welf, B.A. Ogunnaike, U.P. Naik, Quantitative statistical description of integrin clusters in adherent cells, IET Syst Biol, 3 (2009) 307-316.

[254] J.E. Hoffmann, Y. Fermin, R.L. Stricker, K. Ickstadt, E. Zamir, Symmetric exchange of multi-protein building blocks between stationary focal adhesions and the cytosol, eLife, 3 (2014) e02257.

[255] K. Burridge, C.E. Turner, L.H. Romer, Tyrosine phosphorylation of paxillin and pp125FAK accompanies cell adhesion to extracellular matrix: a role in cytoskeletal assembly, The Journal of cell biology, 119 (1992) 893-903.

[256] T.S. Panetti, Tyrosine phosphorylation of paxillin, FAK, and p130CAS: effects on cell spreading and migration, Front Biosci, 7 (2002) d143-150.

[257] Q.C. Zhang, D. Petrey, L. Deng, L. Qiang, Y. Shi, C.A. Thu, B. Bisikirska, C. Lefebvre, D. Accili, T. Hunter, T. Maniatis, A. Califano, B. Honig, Structure-based prediction of protein-protein interactions on a genome-wide scale, Nature, 490 (2012) 556-560.

[258] W.H. Goldmann, Role of vinculin in cellular mechanotransduction, Cell Biol Int, 40 (2016) 241-256.

[259] J.M. Leerberg, G.A. Gomez, S. Verma, E.J. Moussa, S.K. Wu, R. Priya, B.D. Hoffman, C. Grashoff, M.A. Schwartz, A.S. Yap, Tension-sensitive actin assembly supports contractility at the epithelial zonula adherens, Current biology : CB, 24 (2014) 1689-1699.

[260] O. Soderberg, M. Gullberg, M. Jarvius, K. Ridderstrale, K.J. Leuchowius, J. Jarvius, K. Wester, P. Hydbring, F. Bahram, L.G. Larsson, U. Landegren, Direct observation of individual endogenous protein complexes in situ by proximity ligation, Nature methods, 3 (2006) 995-1000.

[261] D. Shcherbo, C.S. Murphy, G.V. Ermakova, E.A. Solovieva, T.V. Chepurnykh, A.S. Shcheglov, V.V. Verkhusha, V.Z. Pletnev, K.L. Hazelwood, P.M. Roche, S. Lukyanov, A.G. Zaraisky, M.W. Davidson, D.M. Chudakov, Far-red fluorescent tags for protein imaging in living tissues, Biochem J, 418 (2009) 567-574.

[262] T. Ichikawa, M. Kita, T.S. Matsui, A.I. Nagasato, T. Araki, S.H. Chiang, T. Sezaki, Y. Kimura, K. Ueda, S. Deguchi, A.R. Saltiel, N. Kioka, Vinexin family (SORBS) proteins play different roles in stiffness-sensing and contractile force generation, Journal of cell science, (2017).

[263] H. Yamashita, T. Ichikawa, D. Matsuyama, Y. Kimura, K. Ueda, S.W. Craig, I. Harada, N. Kioka, The role of the interaction of the vinculin proline-rich linker region with vinexin alpha in sensing the stiffness of the extracellular matrix, Journal of cell science, 127 (2014) 1875-1886.

[264] J.S. Aaron, A.B. Taylor, T.L. Chew, Image co-localization - co-occurrence versus correlation, Journal of cell science, 131 (2018).

[265] A.K. Kenworthy, Imaging protein-protein interactions using fluorescence resonance energy transfer microscopy, Methods, 24 (2001) 289-296.

[266] B.D. Slaughter, J.W. Schwartz, R. Li, Mapping dynamic protein interactions in MAP kinase signaling using live-cell fluorescence fluctuation spectroscopy and imaging, Proceedings of the National Academy of Sciences of the United States of America, 104 (2007) 20320-20325.

[267] Y.H. Foo, N. Naredi-Rainer, D.C. Lamb, S. Ahmed, T. Wohland, Factors affecting the quantification of biomolecular interactions by fluorescence cross-correlation spectroscopy, Biophysical journal, 102 (2012) 1174-1183.

[268] K.J. Roux, D.I. Kim, M. Raida, B. Burke, A promiscuous biotin ligase fusion protein identifies proximal and interacting proteins in mammalian cells, The Journal of cell biology, 196 (2012) 801-810.

[269] D.I. Kim, S.C. Jensen, K.A. Noble, B. Kc, K.H. Roux, K. Motamedchaboki, K.J. Roux, An improved smaller biotin ligase for BioID proximity labeling, Molecular biology of the cell, 27 (2016) 1188-1196.

[270] J.L. Kadrmas, M.C. Beckerle, The LIM domain: from the cytoskeleton to the nucleus, Nature reviews. Molecular cell biology, 5 (2004) 920-931.

[271] N. Nakazawa, A.R. Sathe, G.V. Shivashankar, M.P. Sheetz, Matrix mechanics controls FHL2 movement to the nucleus to activate p21 expression, Proceedings of the National Academy of Sciences of the United States of America, (2016).

[272] B.J. Haubner, D. Moik, T. Schuetz, M.F. Reiner, J.G. Voelkl, K. Streil, K. Bader, L. Zhao, C. Scheu, J. Mair, O. Pachinger, B. Metzler, In vivo cardiac role of migfilin during experimental pressure overload, Cardiovasc Res, 106 (2015) 398-407.

[273] B. Fabry, J.J. Fredberg, Mechanotransduction, asthma, and airway smooth muscle, Drug Discov Today Dis Models, 4 (2007) 131-137.

[274] P.B. Noble, C.D. Pascoe, B. Lan, S. Ito, L.E. Kistemaker, A.L. Tatler, T. Pera, B.S. Brook, R. Gosens, A.R. West, Airway smooth muscle in asthma: linking contraction and mechanotransduction to disease pathogenesis and remodelling, Pulm Pharmacol Ther, 29 (2014) 96-107.

[275] P. Lu, V.M. Weaver, Z. Werb, The extracellular matrix: a dynamic niche in cancer progression, The Journal of cell biology, 196 (2012) 395-406.

[276] S. Kaushik, M.W. Pickup, V.M. Weaver, From transformation to metastasis: deconstructing the extracellular matrix in breast cancer, Cancer Metastasis Rev, (2016).

[277] M.A. Karsdal, T. Manon-Jensen, F. Genovese, J.H. Kristensen, M.J. Nielsen, J.M. Sand, N.U. Hansen, A.C. Bay-Jensen, C.L. Bager, A. Krag, A. Blanchard, H. Krarup, D.J. Leeming, D. Schuppan, Novel insights into the function and dynamics of extracellular matrix in liver fibrosis, Am J Physiol Gastrointest Liver Physiol, 308 (2015) G807-830.

[278] M. Walraven, B. Hinz, Therapeutic approaches to control tissue repair and fibrosis: Extracellular matrix as a game changer, Matrix Biol, (2018).

[279] N. Borghi, M. Sorokina, O.G. Shcherbakova, W.I. Weis, B.L. Pruitt, W.J. Nelson, A.R. Dunn, E-cadherin is under constitutive actomyosin-generated tension that is increased at cell-cell contacts upon externally applied stretch, Proceedings of the National Academy of Sciences of the United States of America, 109 (2012) 12568-12573.

[280] D.E. Conway, M.T. Breckenridge, E. Hinde, E. Gratton, C.S. Chen, M.A. Schwartz, Fluid shear stress on endothelial cells modulates mechanical tension across VE-cadherin and PECAM-1, Current biology : CB, 23 (2013) 1024-1030.

[281] J. Seong, A. Tajik, J. Sun, J.L. Guan, M.J. Humphries, S.E. Craig, A. Shekaran, A.J. Garcia, S. Lu, M.Z. Lin, N. Wang, Y. Wang, Distinct biophysical mechanisms of focal adhesion kinase mechanoactivation by different extracellular matrix proteins, Proceedings of the National Academy of Sciences of the United States of America, 110 (2013) 19372-19377.

[282] C.L. Gilchrist, J. Chen, W.J. Richardson, R.F. Loeser, L.A. Setton, Functional integrin subunits regulating cell-matrix interactions in the intervertebral disc, J Orthop Res, 25 (2007) 829-840.

[283] S. Jalali, M.A. del Pozo, K. Chen, H. Miao, Y. Li, M.A. Schwartz, J.Y. Shyy, S. Chien, Integrin-mediated mechanotransduction requires its dynamic interaction with specific extracellular matrix (ECM) ligands, Proceedings of the National Academy of Sciences of the United States of America, 98 (2001) 1042-1046.

[284] M.J. Paszek, C.C. DuFort, M.G. Rubashkin, M.W. Davidson, K.S. Thorn, J.T. Liphardt, V.M. Weaver, Scanning angle interference microscopy reveals cell dynamics at the nanoscale, Nature methods, 9 (2012) 825-827.

[285] D.M. Shcherbakova, V.V. Verkhusha, Near-infrared fluorescent proteins for multicolor in vivo imaging, Nature methods, 10 (2013) 751-754.

[286] C. Gayrard, N. Borghi, FRET-based Molecular Tension Microscopy, Methods, 94 (2016) 33-42.

[287] A.K. Lagendijk, G.A. Gomez, S. Baek, D. Hesselson, W.E. Hughes, S. Paterson, D.E. Conway, H.G. Belting, M. Affolter, K.A. Smith, M.A. Schwartz, A.S. Yap, B.M. Hogan, Live imaging molecular changes in junctional tension upon VE-cadherin in zebrafish, Nat Commun, 8 (2017) 1402.

[288] D. Cai, S.C. Chen, M. Prasad, L. He, X. Wang, V. Choesmel-Cadamuro, J.K. Sawyer, G. Danuser, D.J. Montell, Mechanical feedback through E-cadherin promotes direction sensing during collective cell migration, Cell, 157 (2014) 1146-1159.

[289] D. Eder, K. Basler, C.M. Aegerter, Challenging FRET-based E-Cadherin force measurements in Drosophila, Scientific reports, 7 (2017) 13692.

Biography

Andrew Scott LaCroix was born on April 18th, 1989 in St. Louis Park, Minnesota to Susanne and Michael LaCroix. He graduated from Minnetonka High School in Minnetonka, MN in 2007. Andrew attended the University of Wisconsin-Madison from 2007-2011, graduating with his B.S. in Biomedical Engineering in December 2011. He attended Duke University from 2012-2018, being awarded his PhD in Biomedical Engineering in May 2018.

PUBLICATIONS
*indicates equal contribution

LaCroix, A. S., Lynch, A. D., Berginski, M. E., & Hoffman, B. D. (2018). Tunable molecular tension sensors reveal extension-based control of vinculin loading. eLife in press.

LaCroix, A. S.*, Rothenberg, K. E.*, & Hoffman, B. D. (2015). Molecular-scale tools for studying mechanotransduction. Annual review of biomedical engineering, 17, 287-316.

LaCroix, A. S.*, Rothenberg, K. E.*, Berginski, M. E., Urs, A. N., & Hoffman, B. D. (2015). Construction, imaging, and analysis of FRET-based tension sensors in living cells. In Methods in cell biology (Vol. 125, pp. 161-186). Academic Press.

LaCroix, A. S., Duenwald-Kuehl, S. E., Lakes, R. S., & Vanderby, R. (2013). Relationship between tendon stiffness and failure: a metaanalysis. Journal of Applied Physiology, 115(1), 43-51.

LaCroix, A. S., Duenwald-Kuehl, S. E., Brickson, S., Akins, T. L., Diffee, G., Aiken, J., ... & Lakes, R. S. (2013). Effect of age and exercise on the viscoelastic properties of rat tail tendon. Annals of biomedical engineering, 41(6), 1120-1128.

Knowles, D. B., **LaCroix, A. S.**, Deines, N. F., Shkel, I., & Record, M. T. (2011). Separation of preferential interaction and excluded volume effects on DNA duplex and hairpin stability. Proceedings of the National Academy of Sciences, 108(31), 12699-12704.

FELLOWSHIPS & AWARDS
Graduate Research Fellowship Honorable Mention, National Science Foundation (2013)
James E. McElhaney Fellowship from Duke Univeristy (2013)
Speaker Travel Award from the Cell and Molecular Bioengineering SIG (2017)
Kewaunee Senior Graduate Student Poster Award from Duke CBTE (2018)